



저작자표시-변경금지 2.0 대한민국

이용자는 아래의 조건을 따르는 경우에 한하여 자유롭게

- 이 저작물을 복제, 배포, 전송, 전시, 공연 및 방송할 수 있습니다.
- 이 저작물을 영리 목적으로 이용할 수 있습니다.

다음과 같은 조건을 따라야 합니다:



저작자표시. 귀하는 원저작자를 표시하여야 합니다.



변경금지. 귀하는 이 저작물을 개작, 변형 또는 가공할 수 없습니다.

- 귀하는, 이 저작물의 재이용이나 배포의 경우, 이 저작물에 적용된 이용허락조건을 명확하게 나타내어야 합니다.
- 저작권자로부터 별도의 허가를 받으면 이러한 조건들은 적용되지 않습니다.

저작권법에 따른 이용자의 권리는 위의 내용에 의하여 영향을 받지 않습니다.

이것은 [이용허락규약\(Legal Code\)](#)을 이해하기 쉽게 요약한 것입니다.

[Disclaimer](#)

공학박사학위논문

A STUDY ON IMPROVEMENT OF
ELECTRICAL PROPERTIES OF SOLUTION-PROCESSED
TRANSPARENT CONDUCTING OXIDES AND
METAL FILMS AFTER ANNEALING

용액 공정으로 형성한
투명 전도성 산화물과 금속 박막의
열처리 공정에 따른 전기적 특성 향상 연구

2014년 8월

서울대학교 대학원

재료공학부

김 나 래

용액 공정으로 형성한
투명 전도성 산화물과 금속 박막의
열처리 공정에 따른 전기적 특성 향상 연구
A STUDY ON IMPROVEMENT OF ELECTRICAL PROPERTIES OF
SOLUTION-PROCESSED TRANSPARENT CONDUCTING
OXIDES AND METAL FILMS AFTER ANNEALING

지도교수: 주 영 창

이 논문을 공학박사 학위논문으로 제출함
2014년 8월

서울대학교 대학원
재료공학부
김 나 래

김 나 래의 박사학위 논문을 인준함
2014년 7월

위원장	남기태	(인)
부위원장	주영창	(인)
위원	장호원	(인)
위원	최광열	(인)
위원	이범주	(인)

ABSTRACT

A Study on the Improvement of the Electrical Properties of Solution-processed Transparent Conducting Oxides and Metal Films after Annealing

Na-Rae Kim

Department of Materials Science and Engineering

The Graduate School

Seoul National University

Solution processing has many advantages over vacuum-assisted deposition, such as the development of printing or coating techniques that are low cost, environmentally friendly, and capable of being performed at atmospheric pressure; however, film quality and performance must be improved. After solution processing, post-treatment processes (post-annealing) are essential to solidify the films, remove the internal defects, and control the properties. Electrical conductors were chosen for study because conducting materials are fundamental and essential materials in electronic devices. Among various potential materials, research on metals and metal oxides (Transparent conducting oxides, TCOs) was conducted in this research. The conductivity of metal nanoparticle films was improved by the elimination of organic ligands capping the nanoparticles and by the formation of a dense microstructure with few pores. This result is due to the high heating rate during annealing. In tin-doped indium oxide (ITO) nanoparticle research, the

representative material for TCOs, the optimization of oxygen partial pressure was appropriate for increasing the electron concentration by oxygen vacancy generation and organic ligand removal. ITO nanoparticle films showed improved conductivity and transmittance compared to conventional ITO nanoparticle films after annealing under optimized oxygen partial pressure. However, a high electron concentration in ITO degrades the transmittance in the NIR region. Doping with Mo instead of Sn was the solution to this problem. Spray coating using metal-organic decomposition solution also increased the conductivity and transmittance. W and Zr were used as new doping elements for In_2O_3 , and high conductivity and transmittance were obtained.

Keywords: solution processing, annealing, transparent conducting oxide, metal, oxygen partial pressure, nanoparticle

Student Number: 2011-30931

Table of Contents

Abstract.....	i
Table of contents.....	iii
List of Tables.....	viii
List of Figures.....	ix

Chapter 1. Introduction

1.1. Evolution of electronic devices	18
1.2. Solution processing	19
1.3. Solution-processed conductors	21
1.3.1. Printable conducting materials	21
1.3.2. Issues of solution-processed conductors	27
1.4. Annealing process for solution-processed conductors	28
1.5. Objective of the thesis	30
1.6. Organization of the thesis	31

Chapter 2. Theoretical Background

2.1. Electrical properties of solution-processed conductors	32
2.1.1. Metal	33

2.1.2. Metal oxide	33
2.2. Changes in solution-processed conducting films during thermal processing	34
2.2.1. Nanoparticle films	34
2.2.2.1. Microstructure evolution	35
2.2.2. Metal-organic decomposition films	38
2.3. Solution-processed transparent conducting oxide	40
2.3.1. Electrical properties of transparent conducting oxide	41
2.3.1.1. Carrier concentration	41
2.3.1.2. Mobility	42
2.3.2. Optical properties of transparent conducting oxide	43
2.4. High-mobility transparent conducting oxide	47
2.4.1. Previous research on high-mobility TCOs	47
2.4.2. Mechanisms of high mobility	48
2.4.3. High-mobility molybdenum-doped indium oxide	49
2.4.4. Various doping elements for indium oxide films	51

Chapter 3. Experiments

3.1. Materials	53
3.1.1. Metal films	53
3.1.2. Transparent conducting oxide films	54
3.1.2.1. Nanoparticle films	54
3.1.2.2. Metal-organic decomposition films	54
3.2. Solution-based deposition	55

3.2.1. Inkjet printing	55
3.2.2. Spin coating	57
3.2.3. Spray coating	57
3.3. Annealing	58
3.3.1. Furnace annealing	58
3.3.2. Moving rapid thermal annealing	59
3.4. Characterization	61
3.4.1. Electrical properties	61
3.4.2. Optical properties	62
3.4.3. Structural properties	63

Chapter 4. Highly Conductive Ag Nanoparticle Films after Moving Rapid Thermal Annealing

4.1. Introduction	64
4.2. Experimental procedures	67
4.3. Thermal characteristics of the rapid heating system	69
4.4. Electrical resistivity and microstructure of the films	71
4.5 Comparison between furnace and rapid annealing	74
4.6 Film thickness dependence	80
4.7 Summary	82

Chapter 5. Highly Conductive ITO Nanoparticle Films after Oxygen Partial Pressure-Controlled Annealing

5.1. Introduction	83
-------------------------	----

5.2. Experimental procedures	86
5.3. Electrical properties after annealing	88
5.3.1. ' N - μ ' diagram	92
5.3.2. Impurity analysis	95
5.3.3. Microstructure	99
5.4. Optical transmittance	104
5.5. Summary	108

Chapter 6. High-Mobility Spray-Coated In₂O₃-based Films

6.1. Introduction	109
6.2. Experimental procedures	112
6.3. Effect of spray coating parameters	114
6.3.1. Solvent and precursor concentration	114
6.3.2. Substrate temperature	118
6.3.3. Solution volume	123
6.4. Effect of dopant concentration and annealing atmosphere	126
6.4.1. Electrical properties	126
6.4.2. Optical properties	129
6.5. Comparison to other ITO and IMO films	131
6.5.1. Electrical properties	131
6.5.2. Optical properties	134
6.6. Electron concentration and mobility	136
6.7. Other dopants	141
6.8. Summary	149

Chapter 7. Conclusions

7.1. Conclusions	150
References	155
Abstract (In Korean)	165

LIST OF TABLES

- Table 2.1** Properties of high-mobility dopants in In_2O_3 thin films prepared by sputtering on glass substrates.
- Table 6.1** Average optical transmittance of spray-coated ITO and IMO films. (% transmittance)
- Table 6.2** Average optical transmittance of spray-coated W and Zr doped In_2O_3 films. (% transmittance)
- Table 6.3** Fraction and chemical state of W and Zr in In_2O_3 films.

LIST OF FIGURES

- Figure 1.1** Various solution processing methods.
- Figure 1.2** SEM images of solution-processed conductors.
- Figure 1.3** Schematics and morphologies of solution-processed conductor. (a) Films made from nanoparticle solution and (b) from MOD solution (spray coating).
- Figure 1.4** Free-carrier absorptance of films with different carrier concentration (a) and mobility (b).
- Figure 1.5** Flow of solution-based deposition process and the importance of the annealing process.
- Figure 2.1** Schematics of nanoparticle films during annealing.
- Figure 2.2** Effect of spherical particles on grain boundary migration.
- Figure 2.3** A schematic of aerosol transport.

- Figure 2.4** Mass fraction abundance of the elements in the Earth's crust as a function of atomic number. Common TCO cations are highlighted by colored circles and additional dopants by squares.
- Figure 2.5** Transmittance, reflection, and absorption spectra of a typical TCO.
- Figure 2.6** Typical variation in the sheet resistance and average visible transmittance for spray-pyrolyzed ITO (●), FTO (○) and IZO (△) films of various thicknesses (0.1-0.5 μm) prepared under optimized conditions.
- Figure 2.7** Effective mass (open symbol) and relaxation time (closed symbol) as a function of carrier concentration of IMO thin films with 2, 3, and 4 wt. % Mo content.
- Figure 3.1** (a) Dimatix DMP inkjet printer and (b) drop watcher view.
- Figure 3.2** A schematic of the isothermal annealing process. The annealing time is counted once the temperature reaches a set value.
- Figure 3.3** A schematic illustration of the moving rapid thermal annealing process.

- Figure 3.4** Calculating grain size by image analyzer: (a) FE-SEM image of inkjet-printed Ag film annealed at 250 °C for 60 min and (b) associated sketch of grains from FE-SEM image. The grain size was calculated from the sketch by an image analyzer.
- Figure 4.1** Temperature profiles of the samples during rapid thermal annealing.
- Figure 4.2** The resistivities, peak temperature, and the corresponding microstructures of the inkjet-printed Ag films after moving rapid thermal annealing with variation of the applied power. The moving velocity was fixed at 2 cm/min.
- Figure 4.3** Effect of heating schedule on electrical properties and microstructure of inkjet-printed Ag films.
- Figure 4.4** Effect of heating rate on removal of organic ligand and microstructure of inkjet-printed Ag films.
- Figure 4.5** Effect of heating schedule and thickness on microstructure of inkjet-printed Ag films.
- Figure 5.1** A schematic of spin-coated nanoparticle ITO films (left) and ITO nanoparticle solution (right).

- Figure 5.2** Electrical conductivity of nanoparticle ITO films after annealing with various oxygen partial pressures and temperatures.
- Figure 5.3** Electron concentration and mobility of nanoparticle ITO films after annealing with various oxygen partial pressures and temperatures.
- Figure 5.4** Sorting ITO samples in an ' N - μ ' diagram: the nanoparticle ITO films studied here and commercially available sputtered ITO films were plotted in a materials space based on electron concentration and mobility values.
- Figure 5.5** Relative mass fraction of carbon after annealing with various temperatures and oxygen partial pressures measured by SIMS analysis.
- Figure 5.6** Relative mass change of dried ITO nanoparticle powder under air and nitrogen atmospheres.
- Figure 5.7** Inverse of SIMS data (y axis is an inverse of Figure 5.5). (a), (b), and (c) are the points in Figure 5.4. For easy analysis of the effect of impurity on mobility, the inverse of SIMS data are represented.
- Figure 5.8** A TEM image of ITO nanoparticles before annealing.

Figure 5.9 Microstructural images of nanoparticulate ITO films. FE-SEM images after annealing at (a) 250 °C under HV, (b) 550 °C under HV, (c) 550 °C under LV, and (d) 950 °C under LV. (Marked (a), (b), (c), and (d) in Figure 5.5).

Figure 5.10 XRD patterns of nanoparticulate ITO films before and after annealing.

Figure 5.11 Transmittance in the visible spectrum after oxygen partial pressure-controlled annealing. The inset pictures show the optical transparency of the ITO nanoparticle electrodes under various partial pressures and temperatures. A and B mark the samples annealed under 550 °C HV and 250 °C Air, respectively. (b) Transmittance in the 300–340 nm spectral range.

Figure 5.12 Performance comparison between our ITO nanoparticle electrodes and sputtered, MOD, and nanoparticle reference electrodes.

Figure 6.1 Optical transmittance of nanoparticle ITO films. The annealing atmosphere changed the electron concentration in the samples. ITO_1 had higher electron concentration than ITO_2. High electron concentration creates a narrow transparency window.

Figure 6.2 A Schematic of the droplet-to-particle transition in the spray-coating process.

- Figure 6.3** Sheet resistance of spray-coated In_2O_3 films as a function of solvent mixture ratio and precursor concentration.
- Figure 6.4** Optical transparency of spray-coated In_2O_3 films with variation of solvent mixture ratio before and after 2×10^{-2} Torr annealing.
- Figure 6.5** Microstructure of In_2O_3 films with 20 %, 50 %, 80 %, and 90 % ethanol.
- Figure 6.6** Variation of electrical conductance (top), sheet electron concentration (middle), and mobility (down) of spray-coated 1 at. % IMO films as a function of substrate temperature and oxygen partial pressure during annealing.
- Figure 6.7** Microstructural images of 1 at. % IMO films deposited at different temperatures after different oxygen partial pressures. Annealing temperature and time were 550 °C, 1 h.
- Figure 6.8** XRD patterns of In_2O_3 films deposited at different substrate temperatures: 345 °C, 395 °C, 435 °C, and 495 °C.
- Figure 6.9** Description of the deposition processes initiated with increasing substrate temperature.

Figure 6.10 Microstructural images of 1 at. % IMO films deposited with different solution volumes and after oxygen partial pressure-controlled annealing.

(a) After 7×10^{-4} Torr: 12.5 ml (left), 15 ml (middle), 20 ml (right).

(b) After 2×10^{-2} Torr: 12.5 ml (left), 15 ml (middle), 20 ml (right).

(c) After 4×10^{-1} Torr: 12.5 ml (left), 15 ml (middle), 20 ml (right).

Figure 6.11 Optical transmittance spectra of 1 at. % IMO films after annealing. Solution deposition volumes were (a) 10 ml, (b) 12.5 ml, (c) 15 ml, and (d) 20 ml.

Figure 6.12 Variation of electrical conductivity (top), electron concentration, (middle) and mobility (bottom) of spray-coated IMO films as a function of Mo doping and oxygen partial pressure during annealing. Graphs (right) are the electrical properties of the spray-coated ITO film. The optimized Sn concentration was 2.3 at. %.

Figure 6.13 Average transmittance of spray-coated IMO films as a function of Mo concentration and oxygen partial pressure during annealing. ($\lambda = 300 - 2500$ nm).

- Figure 6.14** Sorting IMO samples in an ‘N- μ ’ diagram: the spray-coated IMO films studied here and reference ITO and IMO samples were plotted in a materials space based on electron concentration and mobility values. The half-shaded figure indicates the lowest oxygen pressure and the highest substrate temperature.
- Figure 6.15** Optical transmittance of spray-coated (a) 2.3 at. % ITO and (b) 2 at. % IMO films (concentration of starting solution) in the visible and NIR spectra after oxygen partial pressure-controlled annealing.
- Figure 6.16** Electrical concentration of IMO films; the upper dotted line is the electron concentration that corresponds to 1 e/Mo.
- Figure 6.17** Mo 3d spectra for Mo-doped In₂O₃ films before annealing (a) and after annealing under 7×10^{-4} Torr (b), 2×10^{-2} Torr (c), and 4×10^{-1} Torr (d). The Mo dopant concentration was 2.9 at. %.
- Figure 6.18** TEM images and elemental analysis of 3 at. % Mo-doped In₂O₃ films. Mo segregation was not observed.
- Figure 6.19** A TEM micrograph is displayed using EFTEM. For zones with brighter details, the grain border and grain boundaries correspond to higher W content.

- Figure 6.20** Variation of electrical conductivity, electron concentration, and mobility of spray-coated W- and Zr-doped In_2O_3 films as a function of dopant concentration and oxygen partial pressure during annealing.
- Figure 6.21** Electrical properties of impurity-doped In_2O_3 films in an 'N- μ ' diagram.
- Figure 6.22** Optimal conductivity, electron concentration, and mobility of Mo, W, and Zr-doped In_2O_3 films in an 'N- μ ' diagram.
- Figure 6.23** Transmittance of spray-coated 2.45 at. % W (left) and 2.17 at. % Zr (right)-doped In_2O_3 films in the visible and NIR spectra after oxygen partial pressure annealing.
- Figure 6.24** W 4f spectra for 2.45 at. % W-doped In_2O_3 films (left) and Zr 3d spectra for 2.17 at. % Zr-doped In_2O_3 films (right) after annealing under 2×10^{-2} Torr.

CHAPTER 1

Introduction

1.1 Evolution of electronic devices

For several decades, rapid and continuous development of electronic devices has occurred. This advance is closely related to the miniaturization of electronics, which requires high-density integrated circuits. The design of devices has become more sophisticated, and performance has improved rapidly. Three-dimensional integration and nano-scale devices were developed as cutting-edge technologies. At the same time, interest in this sizable device industry has been increasing due to cost effectiveness. These days, for high-density integration and large-area electronics, new types of electronics are required. Portable devices such as mobile phones and tablet PCs have become popular and created large global markets. Many people are also curious about wearable and attachable electronics, such as smart watches, glasses, lenses, and patches. In the near future, implantable devices may be commercialized. The quality of people's life has been enhanced by the development of these state-of-the-art technologies. For the effective fabrication and development of future electronics, thorough study of the processing and characterization of materials and devices should be supported.

1.2. Solution processing

For large-area and flexible electronics such as wearable and attachable electronics, solution processing has been considered a strong candidate. Solution processing is the fabrication of materials or films based on the chemical solution. Source materials are liquid solution. Generally, this is considered to be a new alternative fabrication method to vacuum-assisted deposition, such as sputtering, evaporation, and pulsed laser deposition. Although these vacuum-based deposition processes are common, interest in solution processes has increased significantly due to the advantages of solution processes for developing printing or coating techniques that are low cost, environmentally friendly, and capable of being performed at atmospheric pressure.¹⁻⁴ Various materials, such as metal oxides, can be obtained by chemical solution processing; thus from synthesis to deposition, a one-step process can be possible. Moreover, solution processing has wide applications in different fields because it has few limitations of film materials and substrates. Especially for flexible electronics, conventional vacuum depositions are hard to apply to a polymer substrate because plastic substrates are sensitive to chemicals and high temperature processing. In addition, vacuum depositions require expensive equipment and batch processes.

Various solution deposition methods are represented in Figure 1.1. Coating techniques can be classified into two categories: the direct growth of the material on the substrate, or liquid coating that requires additional processing to remove solvent and yield the desired phase. In addition to electrochemical and electroless chemical bath deposition, many conducting films are commonly deposited by a liquid coating method.²



Spin coating



Inkjet printing



Screen printing



Offset printing

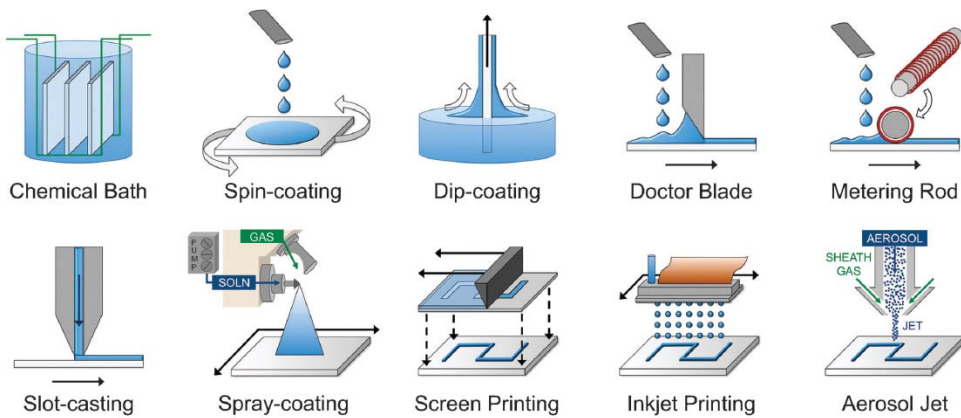


Figure 1.1 Various solution processing methods.²

1.3. Solution-processed conductors

Various materials can be fabricated by solution processing. Materials can be classified as conductors, insulators, and semiconductors according to their electrical properties. Among these, conducting materials are fundamental and essential materials used as interconnects and electrodes in many electronic devices.

1.3.1. Printable conducting materials

There are many types of solution-processable conducting materials, such as metal nanoparticle ink, transparent conducting oxide (TCO) ink, carbon-based materials such as carbon nanotubes or graphene solution, and conducting polymers. Figure 1.2 shows images of solution-processed conductors. Among these materials, metal nanoparticles and TCO ink are the most widely used in electronic devices, because metal nanoparticle ink is low cost and has low resistivity and good processing compatibility and TCO ink shows low resistivity, high transmittance and can be easily obtained by chemical solution processing.

Solution-processed conductors can be produced by metal-organic deposition (MOD) or nanoparticle-based solution methods. MOD uses metal-organic compounds or salts mixed with the desired stoichiometry and dissolved in a solvent.⁴ A nanoparticle solution contains target materials with spherical nano-sized particles suspended in a solvent. Organic ligands are used to coat nanoparticles because they help disperse the nanoparticles. Each ligand has its advantages and disadvantages.

First, nanoparticle-based films can avoid additional crystallization processes because the ITO is pre-synthesized in a particle form.^{2,3,5,6} The optimized dopant concentration

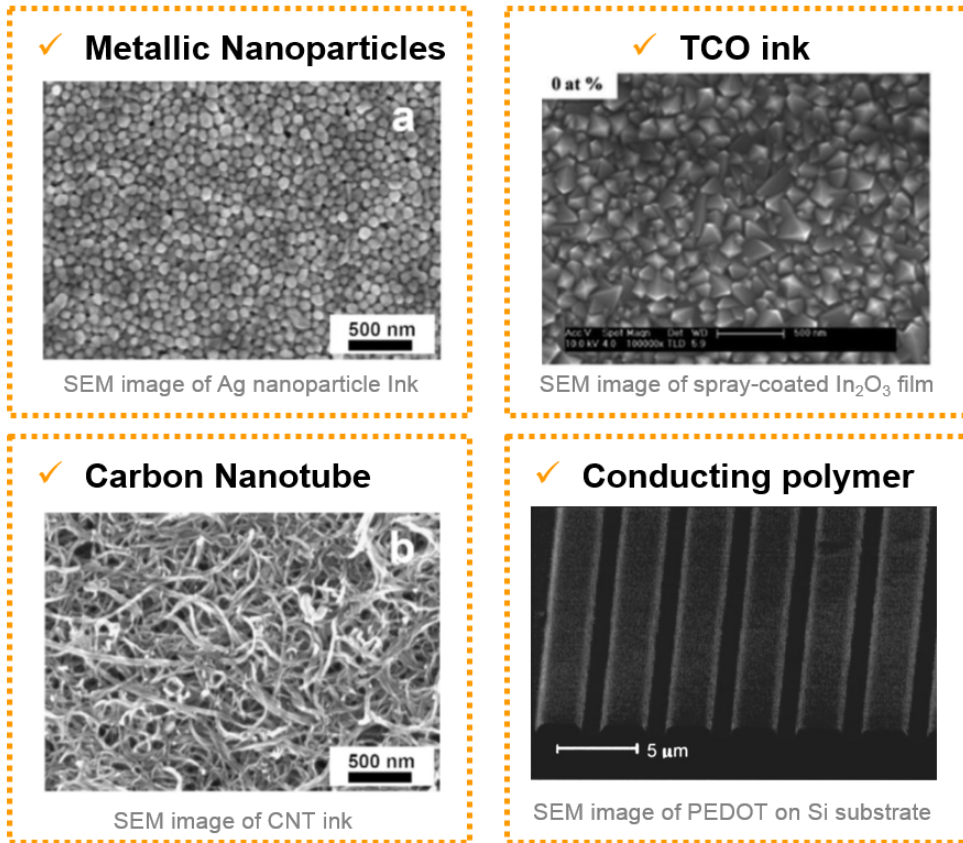


Figure 1.2 SEM images of solution-processed conductors.^{4,7}

can be easily determined, and a lower processing temperature may be possible. Furthermore, nanoparticle films are easier to fabricate as thick films compared to the MOD process.⁸ This represents an advantage over MOD films for the purpose of obtaining low resistance by the geometrical effect, $R = \rho/t$. However, films made from nanoparticle solutions have demonstrated poorer performance compared to the MOD type. This result is due to the different morphology in solution, as seen in Figure 1.3.

MOD solutions are generally the preferred route for oxide materials. In its simplest form, metal–organic compounds or salts are dissolved in a solvent and mixed at the desired stoichiometry. Additional thermal annealing processing is required to remove the organics or counter-ions and create the oxide phase. MOD routes are used for the formation of amorphous material, not just crystalline phases.

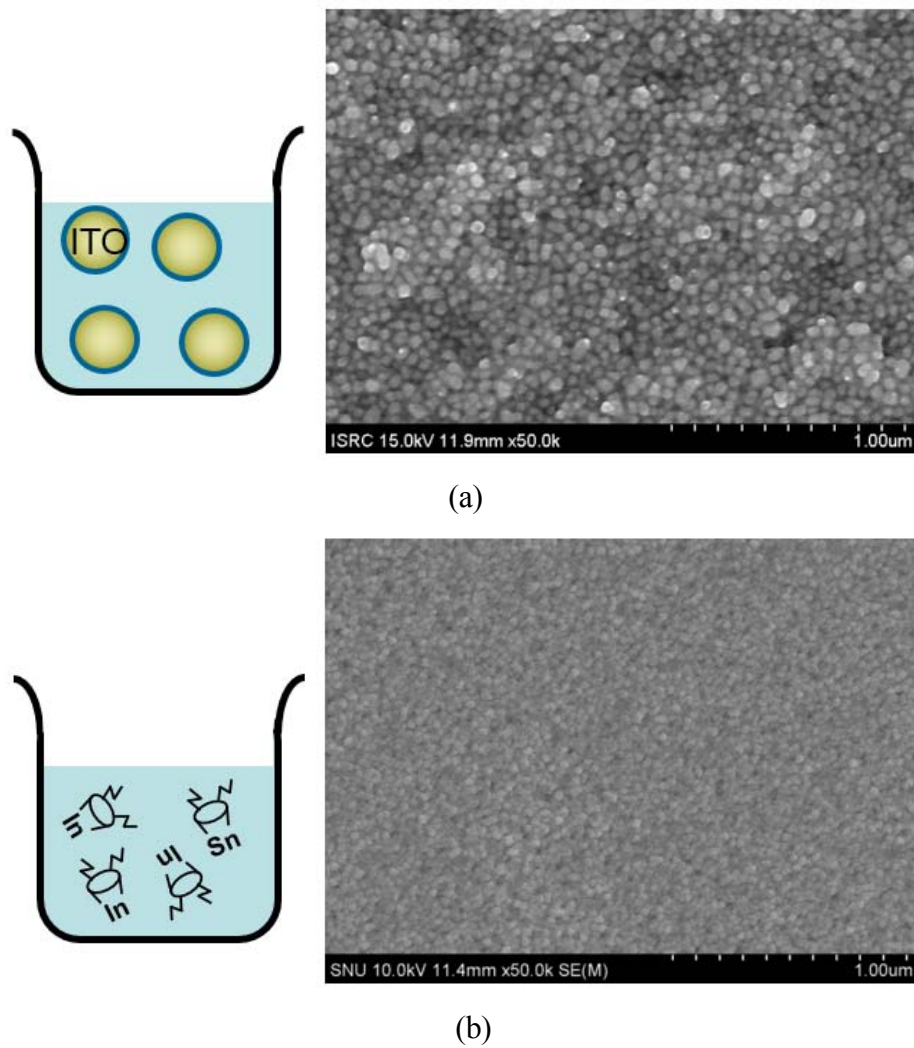
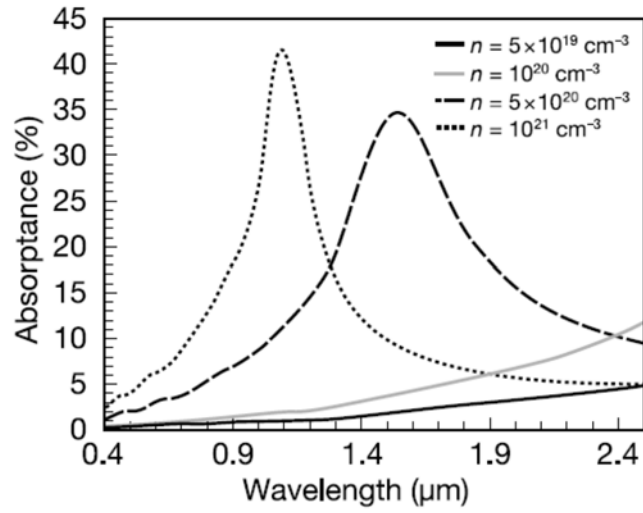


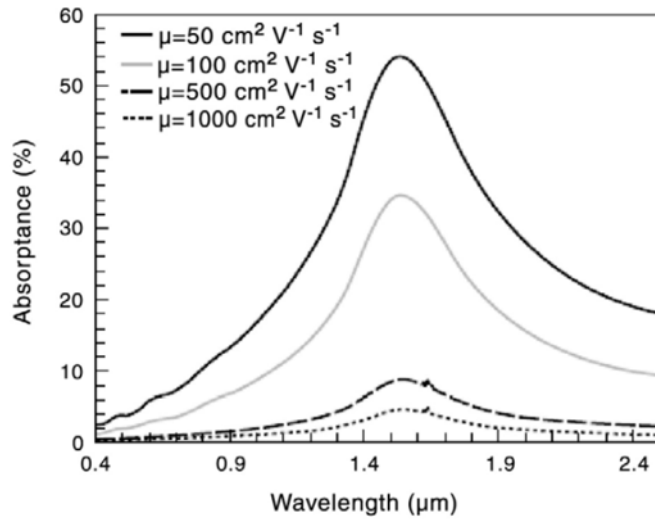
Figure 1.3 Schematics and morphologies of solution-processed conductors. (a) Films made from nanoparticle solution and (b) from MOD solution (spray coating).

Solar cells having wide-range spectral sensitivity result in optical loss in the near infrared (NIR) region due to free carrier absorption (α) in the conventional TCO electrodes, such as Sn-doped In_2O_3 (ITO), F-doped SnO_2 (FTO) and Al- or Ga-doped ZnO films. This sensitivity loss has prompted photovoltaic research on developing visible-to-NIR-transparent TCOs for use in optoelectronics devices. Furthermore, high mobility TCOs are required to derive high current and fast device operating speeds for TFT display applications. Because mobility is a measure of the efficiency of electron movement under the application of an electric field, high mobility enhances the device speed and thereby allows the films to sustain high currents. In devices, high current allows the quick charge or discharge of capacitive loads to yield high operating speeds. Basically, high μ translates into a wide range of application possibilities.⁹

If electron concentration is increased to increase conductivity, the TCO film transmission, especially in the NIR region, reduces as a result of free carrier absorption or metal-like reflection. However, the conductivity of a TCO film may be increased without reducing the NIR transmission by increasing mobility rather than electron concentration. Figure 1.4 shows the change of absorptance in a material with a fixed carrier density ($5 \times 10^{20} \text{ cm}^{-3}$) as the mobility increases.¹⁰



(a)



(b)

Figure 1.4 Free-carrier absorptance of films with different carrier concentration (a) and mobility (b).¹¹

1.3.2. Issues of solution-processed conductors

Solution-based deposition has many advantages; however, it can be a double-edged sword. One of the most representative advantages is the low cost, because the equipment and operation costs for solution-based deposition are projected to be lower than for vacuum deposition methods, whereas the costs related to chemical precursors, organic solvents, additives, and post-processing criteria might be expensive. Research and understanding into the chemistries of solution systems is crucial to overcome these potential limitations. Generally, solution-processed films show low uniformity and reproducibility. Fine line width is difficult to achieve. As a result, the conductivity and related performance are worse than for vacuum-deposited films. Many studies have focused on the improvement of the electrical, optical, and mechanical properties of solution-processed conducting films.²

1.4. Annealing process for solution-processed conductors

In solution processing, post-treatment processes (post-annealing) are essential steps. Because the starting materials are in liquid solution, films have to be solidified by an annealing process. Figure 1.5 shows the flow of the solution-based deposition process and the importance of the annealing process. Solution processing starts with solution synthesis. Solution types can be subdivided into two groups as mentioned previously. In the synthesis of the solution, dispersion, stability, matching with deposition processing, low-cost, and safety must be considered. Using starting solution, films are deposited and patterned. The achievement of fine line-width and large area processing is important. After annealing, electronic devices are fabricated. The improvement of performance comparable to the performance of sputtered devices is an important goal. The connection between printing and device performance is the annealing process. In the annealing process, the greatest change occurs in solution-processed materials, and final properties are determined. Therefore, the annealing process is a very crucial step for solution processing and must be investigated thoroughly.

The annealing process can be classified into four steps. First, liquid film is solidified by solvent evaporation. Second, organic additives are removed, and the precursor is decomposed. Third, the microstructure of the material evolves. Fourth, defects, such as oxygen vacancy, can be controlled.

There have been many attempts to introduce roll-to-roll processing, which is considered the main way to realize the mass production of flexible electronics [3], because roll-to-roll processing allows the fabrication process to be low-cost and continuous. Roll-to-roll processing can be applied to deposition as well as post-treatment processing.

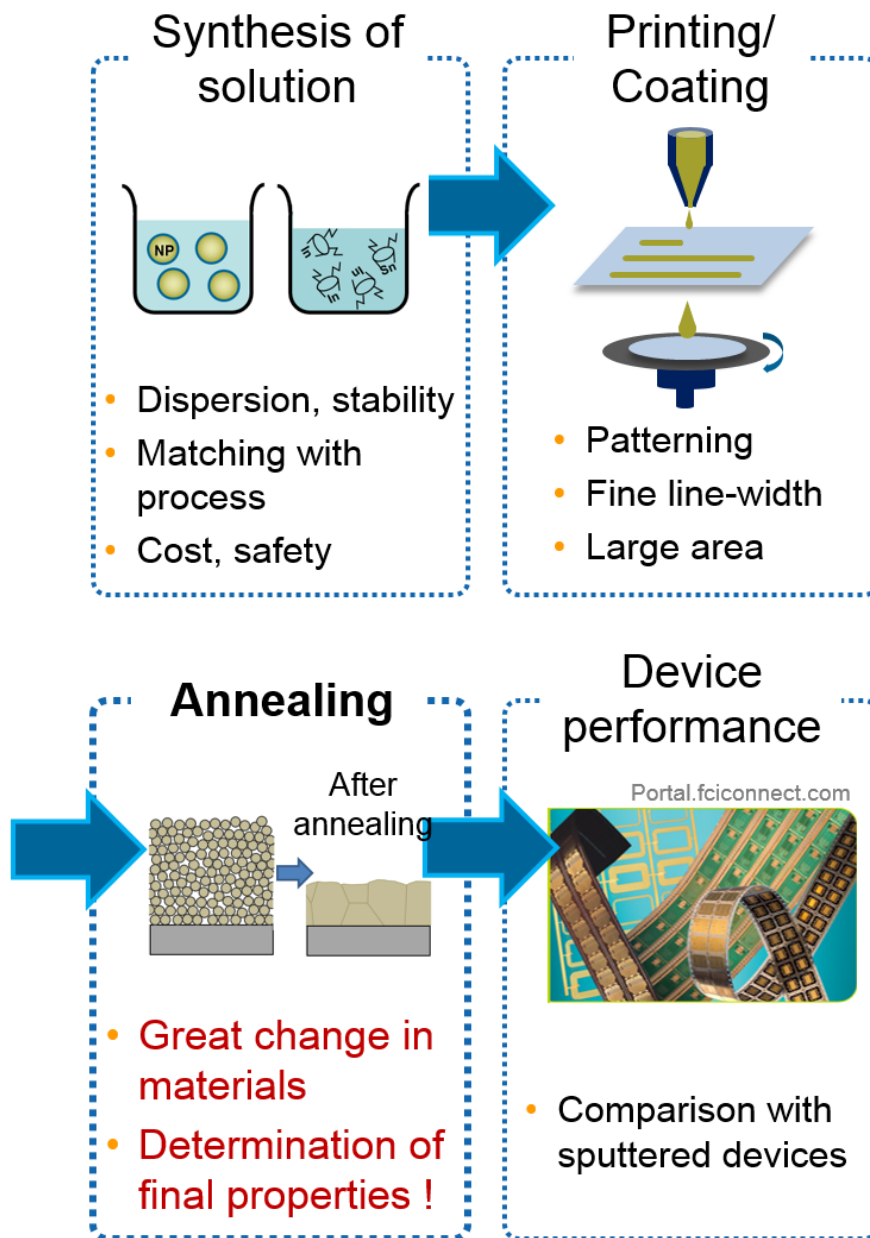


Figure 1.5 Flow of solution-based deposition process and the importance of the annealing process.

1.5. Objective of the thesis

Solution processing has several advantages over vacuum-assisted deposition; however, film quality and performance need to be improved. Among various conductors, metal and metal oxide were chosen for study here because of their practicality and low-cost. For many reasons, the annealing process is an essential step after solution-based deposition.

Interest in the application of metal and metal oxide to the printing process or device fabrication is increasing; however, these materials' properties and mechanisms have not been fully investigated. A clear explanation for the low conductivity and transmittance of metal and TCO films has not been reported; only some speculation or experiment-specific explanations have been provided.^{6,8} However, the importance of confirming the cause of low performance and improving the technology is fundamentally and industrially significant.

The objective of this thesis is to improve the performance, especially the electrical and optical properties, of solution-processed conducting films through the annealing process. Before the improvement could be made, investigation into the cause of the poor performance of solution-processed films was necessary. Based on this study, electrical and optical properties were improved, and mechanistic studies were conducted to understand the materials' characteristics, such as impurity inside the films, microstructure, vacancy, and dopant elements. This study and research system will provide guidelines for improving other solution-processed materials in addition to the conducting ones.

In detail, an annealing system that conceptually simplifies roll-to-roll processing was constructed, and the conductivity of inkjet-printed metal nanoparticle films was improved by a high heating rate annealing process.

In TCO materials, optical properties were also studied. Increased electron concentration and mobility can be achieved by controlling the annealing parameters. To improve the mobility and optical properties, new dopant materials were introduced.

1.6. Organization of the thesis

This thesis consists of seven chapters. In Chapter 2, the basic concept and changes to the physical properties during the annealing process for solution-processed metal and TCO materials are reviewed. High mobility TCO and its mechanism are also explained in Chapter 2 in detail. Chapter 3 describes the experimental procedures, including the detailed solution-based deposition and annealing processes for the samples. In Chapter 4, high heating rate annealing with a movable lamp is proposed. The microstructure and electrical conductivity of Ag nanoparticle films are improved, and the mechanism is related to the effect of the heating rate on the decomposition of organic ligand and microstructure evolution. Chapter 5 discusses the distinct effect of the oxygen partial pressure on electron concentration and mobility during annealing using Hall measurements. The electrical and optical properties of ITO nanoparticle films after annealing are compared with the sputtered films. Chapter 6 describes the achievement of high mobility and transmittance in the near-infrared (NIR) region by changing doping elements and controlling the processing parameters. Chapter 8 summarizes the results of this study.

CHAPTER 2

Theoretical background

2.1. Electrical properties of solution-processed conductors

In conducting materials, electrical conductivity is the most important characteristic, and it affects the final performance of electronic devices. Conductivity is the inverse of the resistivity, which quantifies how strongly a given material opposes the flow of electric current. A low resistivity indicates a material that readily allows the movement of electric charge. The conductivity of metal and metal oxide can be represented by the following equation:

$$\sigma = Ne\mu \quad (2.1)$$

where N is the carrier concentration, μ is the mobility, and e is the electron charge. Carrier concentration is the number of carriers in the specific volume (cm^{-3}), and mobility indicates how quickly a carrier can move through a metal or semiconductor.

2.1.1. Metal

In metals, the carriers are free electrons, and the electron concentration (N_f) is fixed. N_f is proportional to the number of metal atoms, N_a :

$$N_a = \frac{N_0 \delta}{M} \quad (2.2)$$

where N_0 is the Avogadro constant, δ is the density, and M is the atomic mass of the element. Therefore, N is fixed in the same metal, and μ determines the conductivity. Matthiessen's rule, based on experimental results, says that the resistivity arises from independent scattering processes, which are additive.¹²

$$\rho_{total} = \rho_{th} + \rho_{imp} + \rho_{def} \quad (2.3)$$

$$\rho = \frac{1}{\sigma} \quad (2.4)$$

2.1.2. Metal oxide

In metal oxide, N can be both electrons and holes. N can be changed by doping or controlling oxygen vacancy. The mobility similarly governs the resistivity according to Matthiessen's rule.

$$\frac{1}{\mu_{total}} = \frac{1}{\mu_{impurity}} + \frac{1}{\mu_{defect}} + \dots \quad (2.5)$$

Conductivity can be improved by doping, which increases N . However, dopant atoms occupy random sites in the host lattice, and the process of doping certainly impairs the mobility while increasing N . Thus, obtaining the lowest possible resistivity is a trade-off. The following relationship was deduced by Johnson and Lark-Horovitz:¹³

$$\mu = 9.816N^{-2/3} \quad (2.6)$$

This equation results in an optimum conductivity of approximately 5000 S cm^{-1} in indium-doped tin oxide (ITO).

In solution-processed films, large amounts of impurities and defects necessarily exist inside the films and are difficult to control. They degrade the mobility and conductivity.

2.2. Changes in solution-processed conducting films during thermal processing

As mentioned above, two main types of formulations are used: nanoparticle suspensions and metal–organic deposition (MOD) solutions. Changes in solution-processed conducting films depend on the solution type.

2.2.1. Nanoparticle films

For nanoparticle solutions, organic ligands, such as oleic acid¹⁴, myristic acid¹⁵, and poly(N-vinylpyrrolidone) (PVP),¹⁶ are used to coat nanoparticles, because they help them to disperse. However, these ligands act as insulators that interrupt electron transfer

and reduce conductivity when they remain in films after processing.¹⁷⁻²⁰ Thus, these organic ligands must be removed to improve the conductivity of nanoparticle-based films. Ligands are usually removed as gaseous oxidation products during the post-annealing processing. After removing ligands, the microstructure of films can change and affect the final film properties. Changes to nanoparticle films during annealing are shown in Figure 2.1. As temperature increases, ligands are removed, and the necking of nanoparticles is observed. After most of the ligands are removed, grain growth and pore formation occur as a function of the annealing parameters.

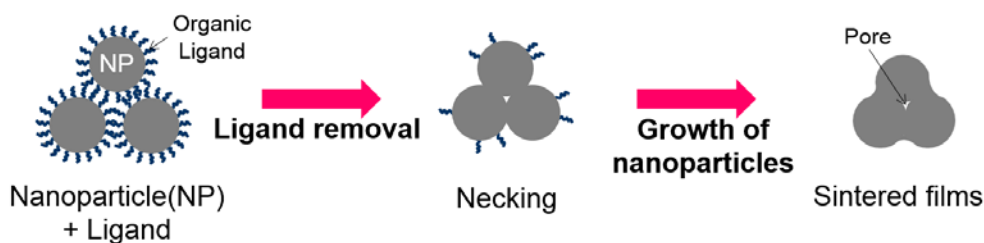


Figure 2.1. Schematics of nanoparticle films during annealing.

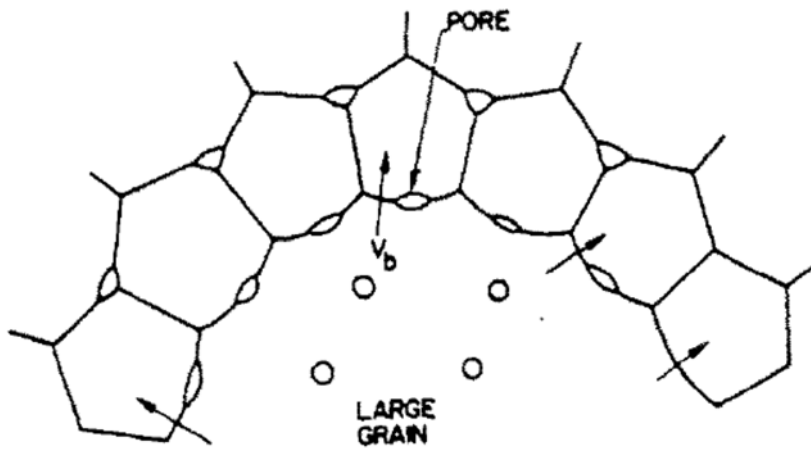
2.2.1.1. Microstructure evolution

The grain growth of nanoparticles is similar to that of polycrystalline materials from the viewpoint of the kinetics. The migration of the grain boundaries is caused by thermodynamic forces. Because the migration of the grain boundaries is considered to result from atomic displacements from one grain to another across the grain boundary, the mobility of the grain boundary usually follows the Arrhenius form. However, the

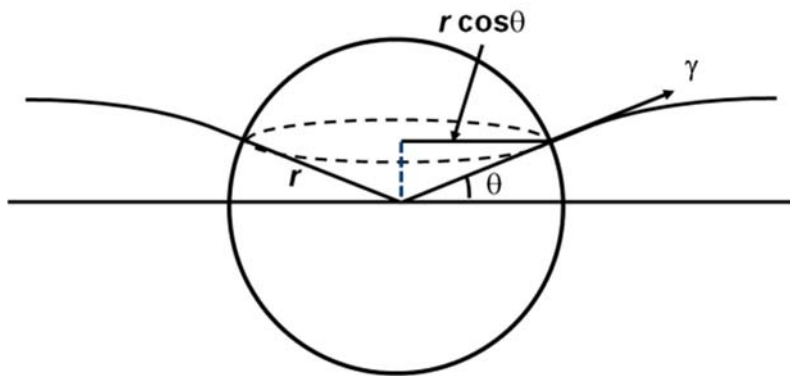
Chapter 2: Theoretical background

difference between the grain growth of nanoparticles and those of other polycrystalline materials is the drag force and its associated mechanism. The dispersion of nanoparticles creates excessive volume, and this dispersion consists of organic additives (impurities in the microstructure evolution of nanoparticles) as well as metal nanoparticles. These factors affect the drag force, which counteracts the driving force of grain growth when they are associated with the grain boundaries, to reduce the free energy.

The dominant drag forces in the grain growth of polycrystalline films are those resulting from dispersed particles, known as the Zener drag force. A single-dispersed particle of submicrometer-size can pin the grain boundaries and prevent its migration. As shown in Figure 2.2, the particles exert a pulling force on the boundary and restrict its motion.



(a)



(b)

Figure 2.2. Effect of spherical particles on grain boundary migration.²¹

2.2.2. Metal-organic decomposition films

The representative solution processing method using MOD solution is spray coating. In deposition, films are formed on the heated substrate. In this step, droplets are converted to particles. This step is crucial for the removal of solvent from the generated droplets (produced by an atomizer) and the transformation into particles. First, the droplets that are generated from the atomizer enter the droplet-to-particle conversion chamber via the flow of carrier gas. Within the aerosol droplets, solvent evaporates, and the solute condenses. This step removes solvent, while the desired components remain in the final product (dried particles or solid films).

An important factor for successful droplet-to-particle conversion using the heat treatment is the optimization of the process conditions. This optimization can be achieved by managing the geometry of the chamber, the carrier gas flow rate, the pressure, precursor concentration, and the temperature.

To achieve this key step, principles of heat and mass transport phenomena must be understood. The heating process must be controlled at a specific temperature to ensure that the solvent is removed completely from the droplet. The minimum temperature process (T_G) can be empirically approximated using a simple Antoine equation²²:

$$T_{wb} = K_1 \left(\frac{T_b}{K_2} \right)^m \log(T_G) + K_3 \quad (2.7)$$

where T_{wb} and T_b are the wet bulb and the boiling temperature, respectively. The symbols K_1 , K_2 , K_3 , and m are the Antoine constants. The characteristic temperature given above is useful for the droplet-to-particle formation step. Selection of temperature can be

Chapter 2: Theoretical background

estimated using the above equation to completely evaporate solvent. In addition, the optimization of the process depends on the residence time.

The aerosol droplets undergo solvent evaporation during the transport to the substrate. This leads to a size reduction of the droplet and to the development of a concentration gradient within the droplet. The precursor precipitates on the surface of the droplet when the surface concentration exceeds the solubility limit. Precipitation occurs due to rapid solvent evaporation and slow solute diffusion.

Many processes occur simultaneously when a droplet hits the surface of the substrate, including solvent evaporation, droplet spreading, and salt decomposition. Many models exist for the decomposition of a precursor. Most researchers suggest that only a CVD process gives high quality films by spray pyrolysis.^{23,24}

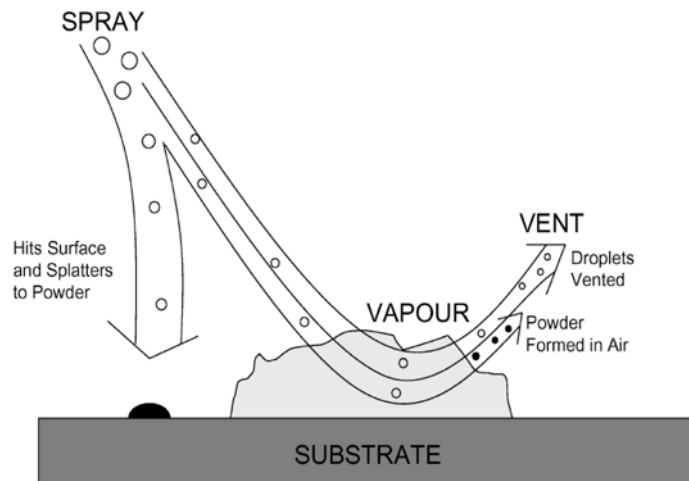


Figure 2.3 A schematic of aerosol transport.²³

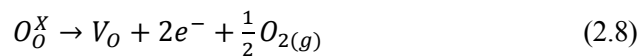
2.3.1. Electrical properties of transparent conducting oxide

As mentioned above, electrical conductivity is determined by N and μ . To obtain films with high conductivity, high carrier concentration and mobility should be simultaneously realized.

The electrical properties of the oxides depend critically upon the oxidation state of the metal component (stoichiometry) and on the characteristics and concentration of impurities incorporated into the films. Perfectly stoichiometric oxides are either insulators or ionic conductors. Ionic conductors are of little interest as transparent conductors. Effective doping can be achieved provided that the dopant is of the same size or smaller than the host ion it replaces and that no compounds form between the dopant oxide and the host oxide.²

2.3.1.1. Carrier concentration

Electronic carriers are generated both intrinsically and extrinsically. In n-type conductors, electrons are carriers. For example, electrons in ITO can be produced by external doping, substituting Sn for In. Doping is an extrinsic method for electron generation. Generally, a high valence difference can make more electrons per dopant atom. Electrons are also generated by oxygen vacancy. Oxygen vacancies generally exist in oxide materials and can be controlled intentionally. Oxygen vacancy generation can be explained by this formula written in Kröger-Vink notation:^{13,25}



The reduction of oxygen partial pressure moves the reaction forward and increases both the oxygen vacancies and the electron concentration.

2.3.1.2. Mobility

Mobility can be described as the ease with which carriers move through the material. It is defined in terms of the average scattering time (relaxation time) (τ) and the carrier effective mass (m^*) by the following equation:

$$\mu = \frac{e\tau}{m^*} \quad (2.9)$$

This equation shows that to increase the mobility, the scattering time must be increased, or the effective mass must be decreased. The latter involves new material development and the former is related to issues of film quality. In general, anything that inhibits the movement of carriers through a material (decreases τ) will decrease mobility and thus decrease conductivity.

The most important sources of scattering in transparent conducting oxide materials are ionized impurity scattering and acoustic phonon scattering (lattice scattering). Grain boundary scattering is significant when grains are small (smaller than the mean free path of the electron). Phase separation and porosity will result in further scattering. The latter is a particular concern in solution processing, because pores can form when solvent and gaseous decomposition products escape the material.²

2.3.2. Optical properties of transparent conducting oxide

The optical properties of a material are closely related to its electronic properties, as the electric field component of light can interact with the electrons of the material according to the Drude free electron model. The transmission, reflection, and absorption spectra of a typical TCO are shown in Figure. 2.5.

Transparent conducting oxides must be transparent in the visible region of the spectrum, typically defined as $\lambda = 400\text{--}750$ nm ($h\nu = 3.1\text{--}1.7$ eV). Light with energy greater than the band gap is absorbed in band transitions. This occurs as an abrupt drop in transmission and increase in absorption at shorter wavelengths (<350 nm). Typical transparent TCOs have a band gap greater than 3 eV. A second decrease in transmission and increase in reflection is observed at the other end of the spectrum at longer wavelengths (>1500 nm). This transition, corresponding to a maximum in absorption, is referred to as the plasma wavelength (λ_p), where the frequency of the light is the same as the frequency of the collective oscillation of electrons in the material. The electrons oscillating in phase with the electric field component of the light results in absorption.²

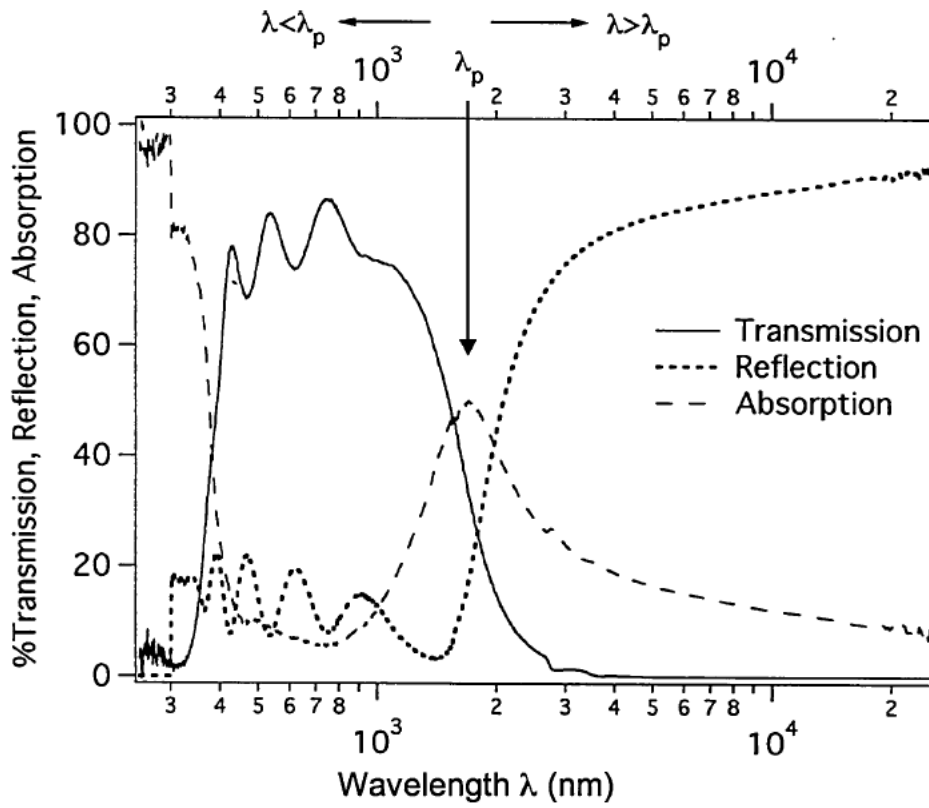


Figure 2.5 Transmittance, reflection, and absorption spectra of a typical TCO.²

Chapter 2: Theoretical background

In many conducting materials, sheet resistance and transmittance have an inverse relationship. As thickness increases, sheet resistance increases but transmittance decreases. Figure 2.6 illustrates the inherent trade-off between these two parameters for a few typical cases. However, a properly chosen combination of R_{sh} and T that takes into account this inherent trade-off can be quite useful for quick comparisons. This has led to different definitions of the figure of merit for transparent conductors. The figure of merit of transparent conductor is described by the following equation: ²⁶

$$\Phi_{TC} = \frac{T^{10}}{R_{sh}} \quad (2.10)$$

For a given material, Φ_{TC} is a function of thickness alone. A value of 10 for the index of T has been chosen to set the visible transmittance T at 90% for that thickness which yields a maximum value of Φ_{TC} . This is very practical and an important standard for the estimation of performance as a transparent electrode. ²⁷

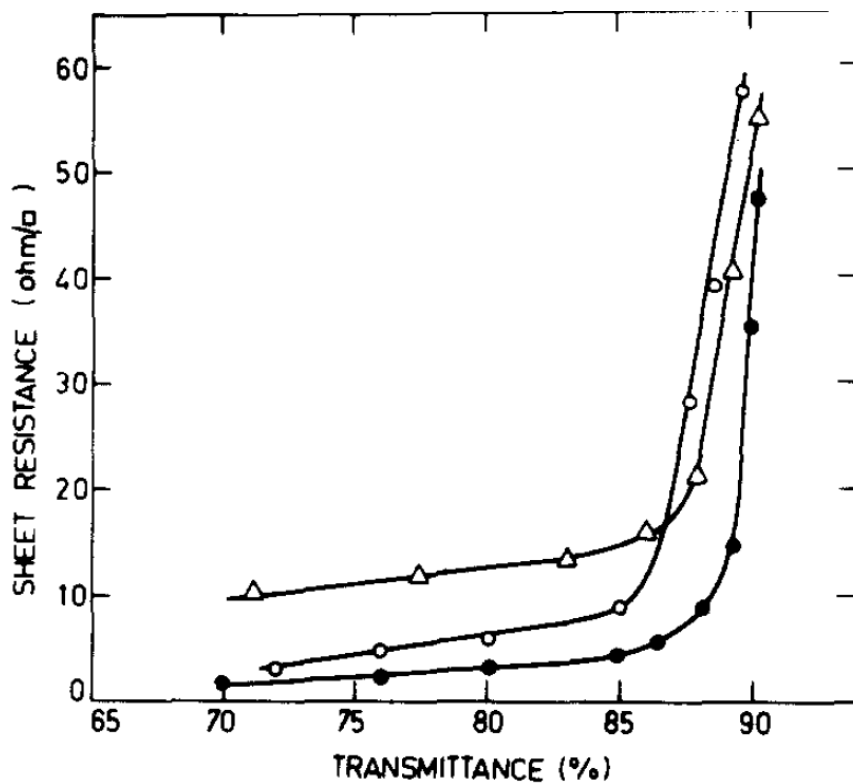


Figure 2.6 Typical variation in the sheet resistance and average visible transmittance for spray-pyrolysed ITO (●), FTO (○) and IZO (△) films of various thicknesses (0.1-0.5 μm) prepared under optimized conditions.²⁷

2.4. High mobility transparent conducting oxide

2.4.1 Previous research on high mobility TCOs

Various strategies have been employed to increase the mobility of TCO thin films while maintaining high transparency and conductivity. First, post-deposition heat treatment in different ambient conditions reduces point and/or dislocation defects in the amorphous or poorly crystallized TCO films by increasing the grain size and improving the overall crystal structure, thus enhancing the electron mobility. Second, while film growth by highly energetic particles can increase the grain size of TCO films, an excessive transfer of momentum can damage the films and reduce the mobility. Third, the control of crystal growth by using highly oriented substrates is known to enhance the mobility of TCO thin films by improving crystallinity. Fourth, Hall mobility in TCO thin films can be increased by reducing scattering caused by intrinsic crystalline defects and/or ionized impurities. Fifth, selective doping methods may increase the relaxation time in TCO materials by separating the doping and charge transport regions. Sixth, hydrogen inclusion can increase the mobility, because hydrogen is “pinned” at a fixed energy level, which introduces shallow defect states in the conduction band of oxides with a high electron affinity, thus leading to n-type doping. Seventh, specific elements have been used to prepare degenerate CdO and In₂O₃ thin films with transmission of > 80% in the visible and NIR wavelength regions by sputtering with $\mu > 62.5 \text{ cm}^2\text{V}^{-1} \text{ s}^{-1}$.

2.4.2. Mechanisms of high mobility

As mentioned above, mobility can be represented by Equation 2.9. The mobility can be increased by increasing τ or by decreasing m^* . Increasing τ requires films with fewer defects, and these can be achieved by decreasing carrier density, reducing the grain boundaries and decreasing neutral impurities. Decreasing m^* requires semiconductors with a widely dispersed conduction band.

First, crystalline quality and structure affects mobility. Poor crystalline quality may cause a reduction in the relaxation time and thus mobility as a result of increased point defects, grain boundaries and lattice distortion. If the crystal structure is disrupted by, for example, a cation vacancy, the spatial spread of the vacant s-orbital around that site is disrupted, causing the effective mass of the electron to increase and thus reducing its mobility. Therefore, shorter cation–cation bond lengths and a favorable distribution of the cations are believed to increase the mobility of the electrons in a semiconductor.

Second, it is known that electronic band structure is important for high mobility. A parabolic conduction band minimum ensures a low effective carrier mass of the electrons, which promotes high mobility. A widely dispersed conduction band minimum allows the unimpeded drift of electrons through the crystal structure and results in a higher relaxation time and thus a higher mobility.

Third, the chemical character of an element can be a factor in choosing appropriate dopants. The Lewis acid strength L can be calculated with a formula developed by Zhang as follows:

$$L = \frac{Z}{r^2} - 7.7\chi_z + 0.8 \quad (2.11)$$

where r is the ionic radius related to the electrostatic force due to the oxidation state Z of the ion, and χ_z is the electronegativity of the element in the respective oxidation state. Using this formula, the Lewis acid strengths of elements have been correlated with high mobility. However, if the Lewis acid is too strong, e.g., Ge in In_2O_3 , the dopant has a greater affinity for oxygen and may incorporate excess oxygen in the lattice, which would then limit μ due to the introduction of scattering centers.¹⁰

2.4.3. High mobility molybdenum-doped indium oxide

Mobility with more than twice the value of the commercial indium tin oxide (ITO) was observed in indium molybdenum oxide (IMO). IMO shows similar conductivity to ITO but low optical absorption and longer wavelength transparency.

Based on the above mechanism in 2.4.2, it has been reported that the electronic band structure of IMO and Lewis acid strength produce the high mobility. The effective carrier mass of IMO was determined as $0.32m_e$ and found to be independent of N , implying a parabolic conduction band minimum. A widely dispersed conduction band minimum allows the unimpeded drift of electrons through the crystal structure, which results in a higher relaxation time and thus a higher mobility. Theoretical studies also suggest that the lowest conduction band of In_2O_3 is split by Sn doping due to the strong hybridization with dopant s-type states, and this splitting contributes to both the decrease of the plasma frequency and the mobility of the carriers. In contrast, calculations of the IMO electronic band structure suggest that high mobility is attainable in degenerate $\text{In}_2\text{O}_3:\text{Mo}$ because the d-states of Mo do not hybridize with the s-states of In, resulting in m^* similar to undoped In_2O_3 .¹⁰

As shown in Figure 2.7, the effective mass of as-deposited IMO films does not vary significantly with Mo content, even though the carrier concentration varies from $\sim 4 \times 10^{19}$ to $\sim 6 \times 10^{20} \text{ cm}^{-3}$. This finding indicates that the conduction band is parabolic, at least over the range associated with the level of degeneracy probed. This degree of parabolicity of the conduction band has not been observed in any other TCO, but m^* is in good agreement with theoretical calculations for the conduction-band minimum in In_2O_3 .

For the Mo-doped indium oxide film, the valence difference of 3 between In^{3+} and Mo^{6+} is much greater than those in other TCO films, such as ZnO:Al , $\text{In}_2\text{O}_3:\text{Sn}$ (ITO), and SnO_2 . This large valence difference can produce more free electrons in the conduction band at a lower doping concentration, which can reduce the impurity scattering of the charge carriers. Additionally, the ionic radius of Mo^{6+} (62 pm) is comparable with that of In^{3+} (81 pm). This size difference will help the effective substitutional doping of Mo in the crystal lattice.²⁸

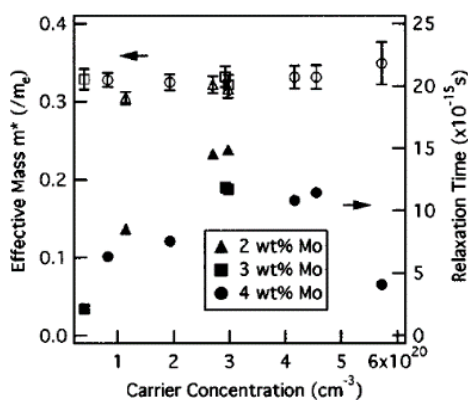


Figure 2.7 Effective mass (open symbol) and relaxation time (closed symbol) as a function of carrier concentration for IMO thin films with 2, 3, and 4 wt. % Mo content.²⁹

2.4.4. Various doping elements for indium oxide films

From the high mobility mechanism in 2.4.2, properties for high-mobility dopants are shown in Table 2.1. The most studied dopant is Mo, and dopants such as Ti, Zr, W show high mobility. A few groups have studied sputtered and spray-coated Mo and Ti-doped In₂O₃ films, but there have been few studies of W and Zr dopants. Table 2.1 shows the factors affecting the mobility and electrical performance of various dopants in In₂O₃ film prepared by sputtering. Generally, solution-processed TCOs show poorer performance and uniformity than sputtered TCOs.

Chapter 2: Theoretical background

Dopant	State	Electron configuration	Lewis acid strength	Ionic radii (pm)	N (10^{20} cm^{-3})	μ ($\text{cm}^2\text{V}^{-1}\text{s}^{-1}$)
H	+	$1s^1$	-	-	1.78	130
In	3+	$[\text{Kr}]4d^{10} 5s^2 5p^1$	1.026	94	2.5	60
Sn	4+	$[\text{Kr}]4d^{10} 5s^2 5p^2$	0.228	71	10.3	43
Zr	4+	$[\text{Kr}]4d^2 5s^2$	2.043	86	76	76
Si	4+	$[\text{Ne}]3s^2 3p^2$	8.098	40		73
W	4+, 6+	$[\text{Xe}]4f^{14} 5d^4 6s^2$	-, 0.68	66, 60	-, 2.9	66
Ge	4+	$[\text{Ar}]3d^{10} 4s^2 4p^2$	-	60	-	60
Mo	6+	$[\text{Kr}] 5s^1 4d^5$	3.667	62	2.7	99
Ti	4+	$[\text{Ar}] 3d^2 4s^2$	3.064	68	3.06	104
Gd	3+	$[\text{Xe}] 4f^7 5d^1 6s^2$	0.788	108	1.74	128
Nd	5+	$[\text{Kr}] 4d^4 5s^1$	2.581	78	10	65

Table 2.1 Properties of high-mobility dopants in In_2O_3 thin films prepared by sputtering on glass substrates.

CHAPTER 3

Experiments

3.1. Materials

3.1.1. Metal films

The synthesis of metal ink was achieved with chemical reduction and hot addition.³⁰ Metal nanoparticles were reduced from their composites at high temperature. These reduced nanoparticles were quenched at room temperature and then allowed to dry for purification. The metal ink was prepared by dispersing these pure nanoparticles in organic additives. Organic ligands coating the nanoparticles help disperse the nanoparticles. However, they act as insulators that interrupt electron transfer and degrade the properties when they remain in films.^{17-20,31}

3.1.2. Transparent conducting oxide films

3.1.2.1. Nanoparticle films

ITO nanoparticle ink can also be synthesized by a hot injection method. Solvent and organic additives affect the dispersion stability and final properties. Particle size and shape are controlled by synthesis temperature, time, concentration and the molecular weight of capping molecules (organic ligands).

3.1.2.2. Metal-organic decomposition films

A representative method for MOD film deposition is spray pyrolysis. Unlike nanoparticle solutions, the precipitation of precursors and the growth of crystals are required, which makes the starting precursor solution and coating environment very important. The starting solution consists of target material precursors, solvent, and additives for high solubility or viscosity control. The concentration of precursors can affect the solution and the film's final characteristics.

Chemical deposition routes start with a precursor, the chemical reagent that contains the cation of interest and reacts to form the desired material and phase. The selection of a precursor is dependent upon the choice of solvent, formulation, and desired processing route. Chloride salts are almost exclusively used for Sn, another common TCO cation. Solution routes to TCOs typically employ acetates, chlorides, or nitrates as precursors, because these compounds are cheap and readily available from commercial suppliers. Metal-organic compounds are another option. Their solubility in polar or non-polar solvents can be adjusted by the choice of the organic substituent.

3.2. Solution-based deposition

3.2.1. Inkjet printing

Inkjet printing is a material-conserving deposition technique used for liquid state materials. The process essentially involves the ejection of a fixed quantity of ink from a cartridge and through a nozzle in a sudden, quasi-adiabatic reduction of the chamber volume via piezoelectric action. A cartridge filled with liquid is contracted in response to the application of an external voltage. This sudden reduction initiates a shockwave in the liquid, which causes a liquid drop to discharge from the nozzle.

This process has been analyzed at some length, and the reader is referred to recent review papers. The ejected drop falls under the forces of gravity and air resistance until it impinges on the substrate, spreads under the momentum acquired in the motion, and surface tension aids flow along the surface. Recent studies show that drop spreading and the final printed shape strongly depend on the viscosity, which in turn is a function of the molar mass of the polymer. More interestingly, a printing height dependence of the final dried-drop diameter, which was a function of the polymer concentration, was also found.³¹

Figure 3.1 shows the Dimatix inkjet printer that was used for metal nanoparticle research in Chapter 4.



Figure 3.1 (a) Dimatix DMP inkjet printer and (b) drop watcher view.

3.2.2. Spin coating

Spin coating is one of the simplest deposition methods, and it is extensively used for smaller, laboratory-scale device processing due to its simplicity and high reproducibility. During the process, the substrate is placed to the spin-coater by a vacuum chuck, and an excess of solution is applied to the center of substrate surface. Then, the substrate is rapidly accelerated (typically to several thousand RPM), which drives solution flow radially outward. A uniform and thin film is left after solvent evaporation.²

3.2.3. Spray coating

Spray coating is a non-contact and large-area deposition method. It is used as either a solution coating method or for the direct growth of thin films when the substrate temperature is over the decomposition temperature of the chemical precursors. This latter method is referred to as spray pyrolysis. In general, atomized droplets are generated pneumatically or ultrasonically and then directed onto the substrate with carrier gas. Spraying generally requires low viscosity solutions.²

3.3. Annealing

3.3.1. Furnace annealing

Before furnace annealing, a drying process is required. After printing, films or patterns are still liquid, and it takes a long time for films to dry naturally. This drying depends on the physical characteristics of the solution (solvent, solid content). For film uniformity and a clear pattern shape, a drying process is necessary.

Isothermal annealing was conducted after drying. The equipment used for annealing was a tube furnace with a high vacuum pump. Control of the annealing temperature (~ 1000 °C), time, and the annealing atmosphere (vacuum, Ar/N₂ gas flowing) is possible. However, the heating rate is slow, so the annealing time can be long. Furthermore, there is a limited capacity for specimen and batch processing.³¹

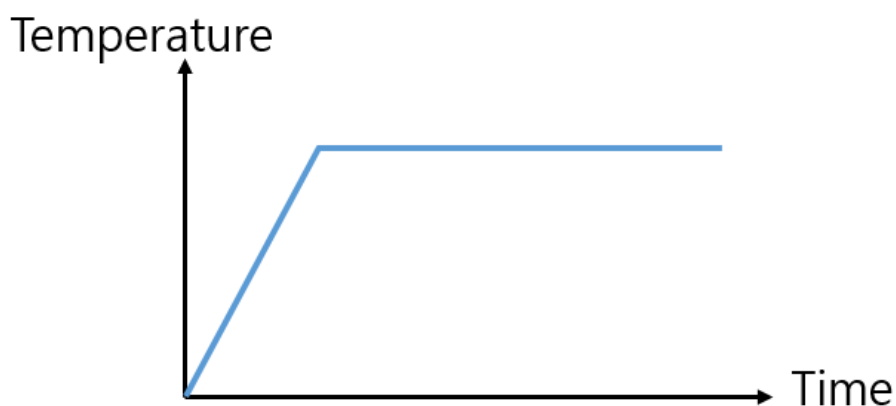


Figure 3.2 A schematic of the isothermal annealing process. The annealing time is counted after the temperature reaches a set value.

3.3.2. Moving rapid thermal annealing

In semiconductor device processing, as-deposited films (vacuum deposition) exhibited weak crystallinity and poor electrical properties. Resolving these problems requires extended post-treatment at high temperatures in a conventional tube furnace. However, such an extended high temperature annealing causes not only a change in the composition and microstructure of the deposited film but also an interaction between the film and the Si substrate. The rapid thermal annealing (RTA) method shortens the annealing time to a few minutes and reduces the interaction at the interface.³²

We have adopted this concept and used a halogen lamp as a heating source. A moving system was added to give a similar effect as a roll-to-roll system.

Figure 3.3 shows schematic illustrations of the movable rapid thermal annealing system. A tubular halogen lamp with a fixed power and velocity moved in the zone specified during annealing. When the lamp reached the specified point, it was turned off. All samples were air-cooled after annealing. The diameter and length of the lamp were 1 cm and 26 cm, respectively. The moving distance was 24.5 cm, and the distance between the sample stage and the lamp was 3.3 cm. The equipment used for the new annealing method consisted of a 33-cm quartz plate on which the printed samples were placed, a halogen lamp (2400 W), and an elliptical reflector, which focused the light on the sample. The lamp and the reflector could move with a constant velocity along the rail located on top of the equipment.³³ A roof covered the reflector and the halogen lamp to prevent heat loss from the lamp and to protect the other parts of the equipment from the heat.

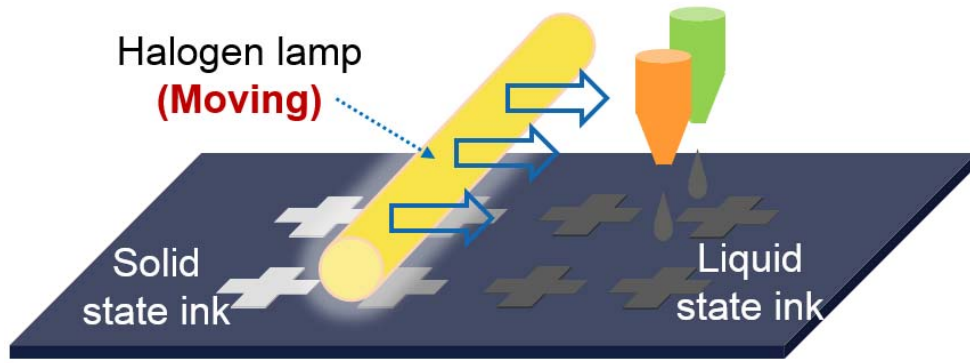


Figure 3.3 A schematic illustration of the moving rapid thermal annealing process.^{34,35}

3.3. Characterization

3.4.1. Electrical properties

Electrical properties are measured by four-point probe and Hall measurements. The four-point probe is a very versatile device used widely in physics for the investigation of electrical phenomena. The effects of contact resistance can be eliminated with the use of a four-point probe. The electrical resistivity is calculated using the sheet resistance measured by the four-point probe method multiplied by the film thickness.

Carrier type, concentration, and mobility can be obtained by the Hall measurement, which uses the Hall effect. The Hall effect is due to the nature of the current in a conductor. When a magnetic field is present that is not parallel to the direction of the motion of moving charges, these charges experience a force called the Lorentz force. When such a magnetic field is absent, the charges follow approximately straight, 'line of sight' paths between collisions with impurities, phonons, etc. However, when a magnetic field with a perpendicular component is applied, their paths between collisions are curved so that moving charges accumulate on one face of the material. This leaves equal and opposite charges exposed on the other face, where there is a scarcity of mobile charges. The result is an asymmetric distribution of charge density across the Hall element that is perpendicular to both the 'line of sight' path and the applied magnetic field.³⁶

3.4.2. Optical properties

Optical properties can be measured by UV spectroscopy. Ultraviolet-visible spectroscopy or ultraviolet-visible spectrophotometry (UV-Vis or UV/Vis) refers to absorption spectroscopy or reflectance spectroscopy in the ultraviolet-visible spectral region. Thus, it uses light in the visible and adjacent (near-UV and NIR) range. The absorption or reflectance in the visible range directly affects the perceived color of the chemicals involved. In this region of the electromagnetic spectrum, molecules undergo electronic transitions.³⁷

The instrument used in ultraviolet-visible spectroscopy is called a UV/Vis spectrophotometer. It measures the intensity of light passing through a sample (I) and compares it to the intensity of light applied to the sample (I₀). The ratio I/I₀ is called the transmittance and is usually expressed as a percentage (%T). The absorbance, A, is based on the transmittance:

$$A = -\log\left(\frac{\%T}{100}\right) \quad (3.1)$$

The UV-visible spectrophotometer can also be configured to measure reflectance. In this case, the spectrophotometer measures the intensity of light reflected from a sample (I) and compares it to the intensity of light reflected from a reference material (I₀) (such as a white tile). The ratio I/I₀ is called the reflectance and is usually expressed as a percentage (%R).

In this thesis, transmittance and absorbance are analyzed. For the investigation of the films, the effect of the substrate (glass) is eliminated.

3.4.3. Structural properties

Structural characteristics are analyzed by X-ray diffraction (XRD), scanning electron microscopy (SEM), focused ion beam (FIB), and transmission electron microscopy (TEM). SEM especially can give us quantitative values for the microstructure, such as grain size, pore size, and porosity. FIB images also show the cross-section morphology, thickness, and contact area with substrate. Higher resolution images and element analysis are possible with TEM images.

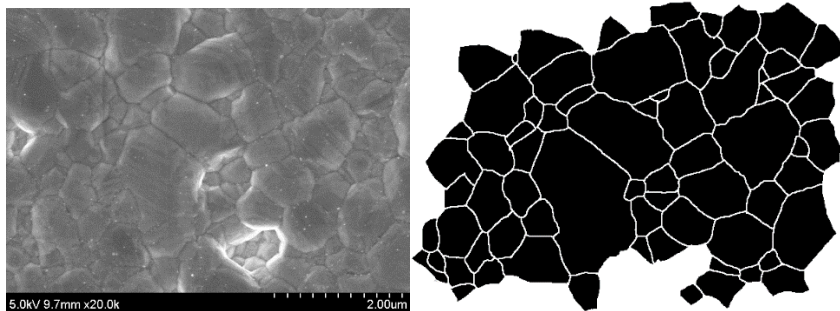


Figure 3.4 Calculating grain size by image analyzer: (a) FE-SEM image of inkjet-printed Ag film annealed at 250 °C for 60 min, and (b) associated sketch of grains from FE-SEM image. The grain size was calculated from the sketch by an image analyzer.

CHAPTER 4

Highly Conductive Ag Nanoparticle Films after Moving Rapid Thermal Annealing

4.1. Introduction

The interest in flexible electronic devices is increasing significantly due to applications such as flexible solar cells, electronic skin,³⁸ displays and radio frequency identification (RFID) tags.³⁹ There have been many attempts to introduce roll-to-roll processing, which is considered the best way to realize the mass production of flexible electronics⁴⁰ because roll-to-roll processing allows the fabrication process to be low-cost and continuous. Roll-to-roll processing should be applied to deposition as well as post-treatment processing. Printing technology, such as inkjet printing, is thought to be the best candidate for the deposition process because it is a simple, atmospheric process that imposes few limitations on the substrate type. Inkjet printing quickly forms the structures and uses less materials compared to the conventional deposition and etching processes.^{41,42}

Metallic nano-size particles have been used as conducting materials for printed electrodes and interconnects for flexible electronic devices. By dispersing the

Chapter 4: Highly conductive Ag nanoparticle films after moving rapid thermal annealing

nanoparticles in a liquid solution (nanoparticle ink), the formation of nanoparticle structures by inkjet printing becomes feasible. Nanoparticles are coated with an organic protective ligand to prevent agglomeration and for dispersion stability in liquid solvents. However, the remaining organic ligand inside the printed films obstructs the coalescence of the metal particles and degrades the electrical performance. Therefore, post-treatment processes (post-annealing) are required to remove the solvent and protective organic ligand.¹⁸ During the post-annealing process, the organic ligands decompose, and the grain growth or coalescence of the metallic nanoparticles occurs, causing the formation of compact metal films. The post-annealing process is usually conducted in a furnace or oven. Because the complete decomposition of the organic ligand and the densification of the nanoparticles are difficult to achieve during conventional annealing, typical printed metal films contain more pores and have a higher electrical resistivity than vacuum-deposited films. Additionally, conventional annealing processes are batch processes and are difficult to apply in roll-to-roll annealing.

We propose a rapid thermal annealing by moving a one-dimensional high-power heating source to produce better electrical and mechanical properties. By using a halogen lamp as the heating source, a highly dense microstructure and low resistivity were obtained in a short processing time. Conventional rapid thermal annealing is a batch process, like furnace annealing, due to the static lamps. We made the lamp move during annealing for continuous roll-to-roll processing. Direct patterning and post-annealing as a one-step process can also be performed using this moving rapid thermal annealing method. The proposed annealing method is suitable for the fabrication of large-area electronics because the specimens can be annealed uniformly by the moving lamp.

The mechanisms of the proposed annealing process, which changes the nanoparticle

Chapter 4: Highly conductive Ag nanoparticle films after moving rapid thermal annealing

films into a high-density grain structure, were studied and linked to the high heating rate and the microstructural evolution. The effect of the heating rate on the inkjet film that is composed of an organic ligand and metal nanoparticles is first reported in this paper. The differences in the microstructure and in the electrical resistivity produced by the conventional furnace annealing and the proposed annealing were analyzed. The two processes were also compared for different film thicknesses to identify the effect of the annealing method on thick metallic films, because these thick films are useful in decreasing resistance.

4.2. Experimental procedures

The Ag nanoparticle ink employed in this study (Silverjet DGP-40LT-15C, Advanced Nano Products Co. Ltd) had a solid loading of 30.4 wt% with an average particle diameter of 10 nm. The Ag nanoparticles were dispersed in triethylene glycol monoethyl ether. The Ag ink was deposited on p-type Si (100) substrates in a 6 mm × 6 mm square pad at room temperature with an inkjet printer (DMP-2831 Dimatix Materials). The film thickness was controlled by the number of overwrite-printings, and all the samples were overwrite-printed three times except in the case of the thick films (which were overwrite-printed five times).

During the moving rapid thermal annealing, the liquid-state films were solidified by heating with the movable halogen lamp, and two parameters were controlled: the applied power and the velocity of the halogen lamp. The ranges of the power and the velocity were 10 – 300 W and 0.4 - 4 cm/min, respectively. Conventional isothermal annealing was compared to this novel method. Conventional annealing was conducted at 250 °C for 60 min with a heating rate of 3 °C/min in a furnace after drying the liquid-state Ag films at 100 °C for 1 h in air in a convection oven. Both annealing processes were performed in air.

To identify the effect of the heating rate on the decomposition temperature and on the duration of the organic ligand and solvent material, thermogravimetric analysis (TGA, TA instrument) was conducted in air over a temperature range from 25 to 450 °C with heating rates of 3 °C /min and 100 °C /min.

Surface and cross-sectional images were obtained by field emission scanning electron microscopy (FE-SEM, Hitachi S-4800) and focused ion beam imaging (FIB, SII SMI-3050TB), respectively. The FIB images were observed in tilt (55°) mode. The

Chapter 4: Highly conductive Ag nanoparticle films after moving rapid thermal annealing

thicknesses of the inkjet-printed Ag films were confirmed by FIB images and measured using an image analyzer. The electrical resistivity was calculated using the sheet resistance measured by the four-point probe method multiplied by the film thickness.

4.3. Thermal characteristics of the rapid heating system

The sintering temperature and time are the most important factors for the final microstructure and resistivity of inkjet-printed films.^{43,44} The temperature during moving rapid thermal annealing was measured to identify the effects of the power and velocity on the heating profile.

Figure 4.1 shows the temperature profiles of the samples while the heating source was moved with various velocities for different powers. The temperature profile was measured using a thermocouple located in the middle of the quartz plate, in the same position as the samples. The peak temperature was reached when the halogen lamp position was just above the sample.

The heating and cooling rates of the proposed annealing are much higher than those for conventional furnace annealing. The temperature increases and then decreases after reaching the peak temperature because the distance between the halogen lamp and the sample changes as the lamp moves. This tendency is different than for conventional annealing, which generally has a heating rate of approximately 10 °C/min and an isothermal stage. The temperature increase during the heating stage consisted of two steps: slower heating, and then rapid heating. The transitions occurred at 1.7 min ($v = 4$ cm/min) and 3.2 min ($v = 2$ cm/min). The probable reason for the two-step heating process is that the heating mechanism changes as the power source approaches the samples. At first, when the halogen lamp is far away, the heat transfer is mostly due to convection. The high heating rates when the lamp is close to the sample are due to the heat absorbed by the radiation source as well as the heat conduction along the substrate.³³

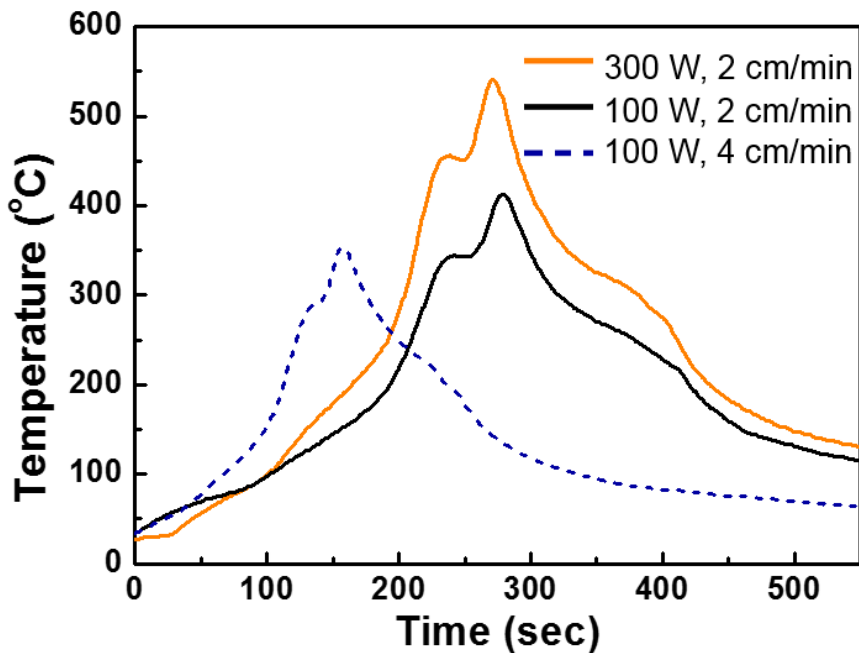


Figure 4.1 Temperature profiles of the samples during rapid thermal annealing.

34,35

The average heating rate was calculated as the difference between the peak temperature and the room temperature divided by the time required to reach the peak temperature. With powers and velocities of 100 W and 4 cm/min, 100 W and 2 cm/min, and 300 W and 2 cm/min, the peak temperatures were 354 °C, 412 °C, and 541 °C, respectively, and the heating rates were 127 °C/min, 84 °C/min and 115 °C/min, respectively. The applied power and velocity determine the peak temperature and the total heat quantity of the sample. Of these two parameters, the applied power was the dominant factor in determining the final microstructure of the inkjet-printed films. The applied power changed the peak temperature, which controlled the grain growth directly and to a greater extent than the velocity.

4.4. Electrical resistivity and microstructure of the films

The changes in the microstructure and resistivity were studied as a function of the applied power and peak temperature. Figure 4.2 shows the resistivity and peak temperature of the sample as a function of the applied power. The corresponding morphologies of the samples with applied powers of 25, 100, and 300 W are shown under the graph. The x-axis shows the applied power, and the left and right y-axes represent the log scale electrical resistivity and linear peak temperature, respectively. As the applied power of the halogen lamp increased, the peak temperature increased, and the density of films increased while the resistivity decreased.

After annealing at 25 W of power, nanometer-size particles remained. The average particle size was 60.5 nm, and the resistivity was 70.2 $\mu\Omega\text{-cm}$, which is 43 times that of bulk silver. It has been reported that the decomposition of the protective organic ligand coating of the metal nanoparticles is directly related to the reduction of the electrical resistivity of the metal nanoparticulate films.⁴⁵ Thus, at powers lower than 25 W, the temperature is not high enough to decompose the ligand. As the applied power increased, the organic ligand decomposed, and as necking formed between neighboring nanoparticles after the ligand partially decomposed, the resistivity decreased very rapidly due to the formation of electron paths among the metal particles.¹⁹

Most of the organic ligand was removed at a power greater than 100 W when the peak temperature was 402 °C, and partial coalescence between the Ag nanoparticles and the grown particles was observed. The average grain size and electrical resistivity at 100 W were 108.18 nm and 8.94 $\mu\Omega\text{-cm}$, respectively. In a power range between 50 W and 200 W, the resistivity change was relatively slow. The contribution of the reduction in

Chapter 4: Highly conductive Ag nanoparticle films after moving rapid thermal annealing

electron scattering due to grain growth and densification to the resistivity decrease was smaller than the reduction due to the ligand removal in the inkjet-printed Ag films.⁴⁶⁻⁴⁹

As the peak temperature increased over 500 °C, the resistivity was less than twice that of bulk silver. At 300 W, the final resistivity was 2.64 $\mu\Omega$ -cm, which is 1.6 times higher than the 1.62 $\mu\Omega$ -cm of bulk silver. The average grain size was 809.15 nm. In this condition, pure Ag remained after the complete removal of the organic ligand, a high-density Ag film formed, and few residual pores were found. Complete decomposition of the organic ligand is also identified in the TGA graph in Figure 4.4, which will be discussed below.

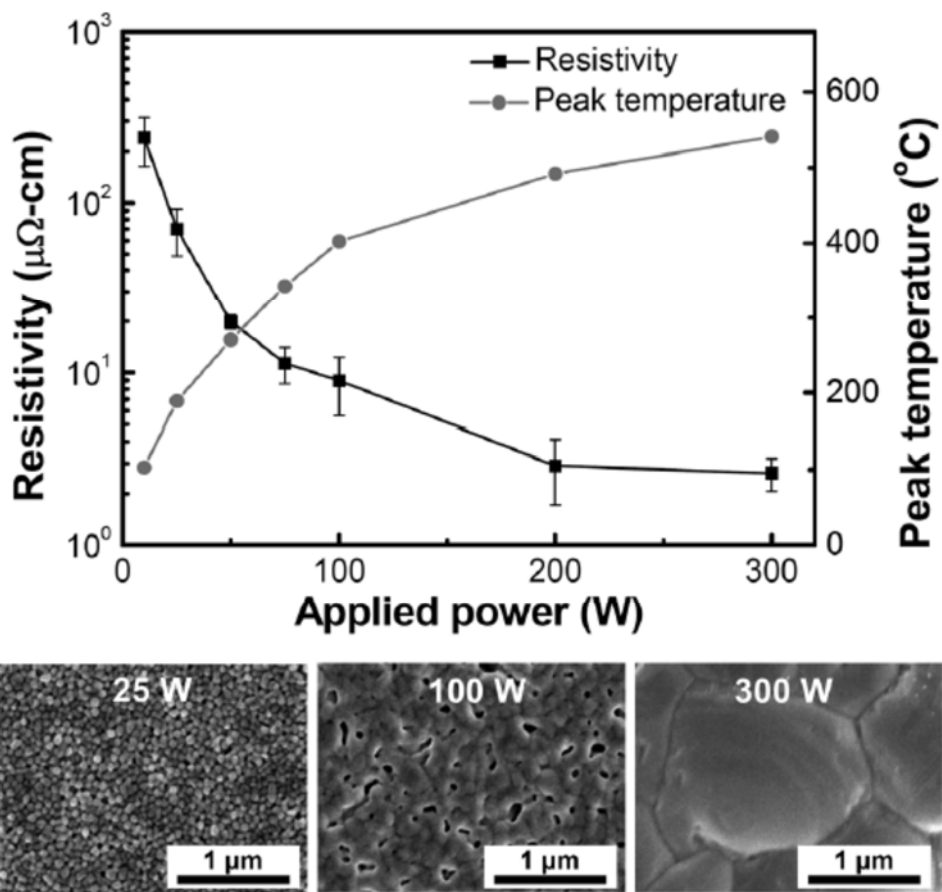


Figure 4.2 The resistivities, peak temperatures, and the corresponding microstructures of the inkjet-printed Ag films after moving rapid thermal annealing with different levels of applied power. The moving velocity was fixed at 2 cm/min.^{34,35}

4.5. Comparison between furnace and rapid annealing

The proposed rapid annealing can be applied to continuous roll-to-roll processing, and the processing time is short, unlike furnace annealing, which is a batch process that requires several hours. In addition, a drying process is not required, and a vacuum or specific gas atmosphere is not necessary for the proposed annealing.

These two annealing processes also create differences in the microstructural evolution and decomposition of the organic ligand due to different heating rates. Moving rapid thermal annealing and conventional furnace annealing were conducted to investigate the effect of the heating rate on the nanoparticle films, and the results are shown in Figure 4.3.

In Figure 4.3, microstructural images after the two annealing processes are illustrated. The thicknesses of the final films were 2.95 μm (moving rapid thermal annealing) and 4.0 μm (furnace annealing). The resistivity of the films after moving rapid thermal annealing (2.82 $\mu\Omega\text{-cm}$) was less than after furnace annealing (4.87 $\mu\Omega\text{-cm}$). The grain structure was much denser and the electrical resistivity was much lower for the films obtained by the proposed process than for films obtained by previous methods.^{44,50-52} The microstructure of the inkjet-printed Ag films that were thermally treated by moving rapid thermal annealing showed micrometer-sized columnar grains with a high density and few pores near the film surface. The difference in thickness between the two methods indicates the higher degrees of densification, which eliminated the internal pores, and grain growth, which reduced the volume fraction of the grain boundaries. In these two photographs of the final microstructure, it can be seen that the moving rapid thermal annealing induced a dense microstructure more effectively than furnace annealing. The high porosity of the microstructure after furnace annealing can lead to a

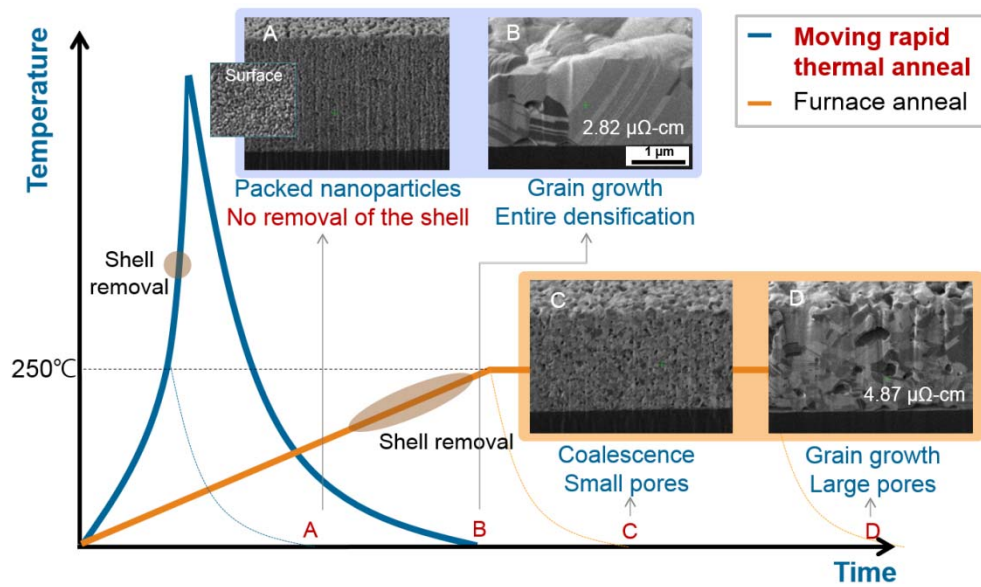


Figure 4.3 Effect of heating schedule on electrical properties and microstructure of inkjet-printed Ag films.^{34,35}

100 °C/min : moving rapid thermal annealing

3 °C/min : furnace annealing

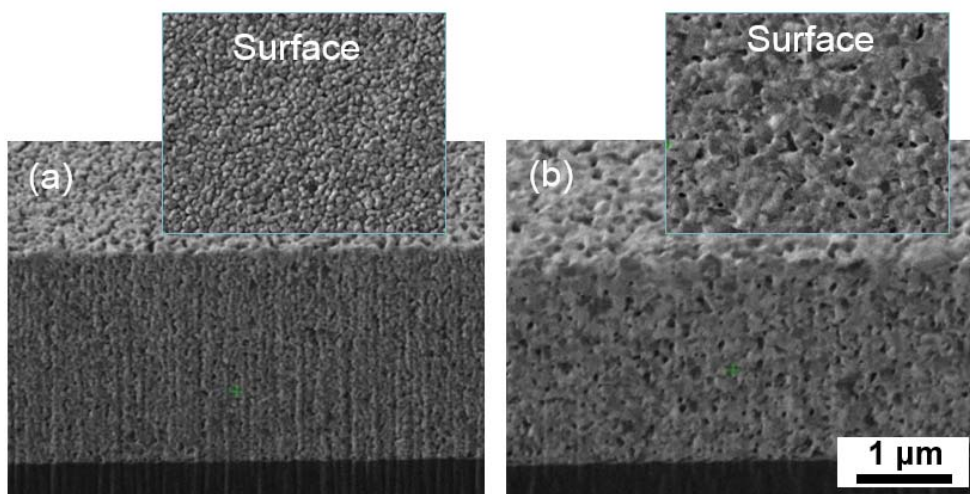
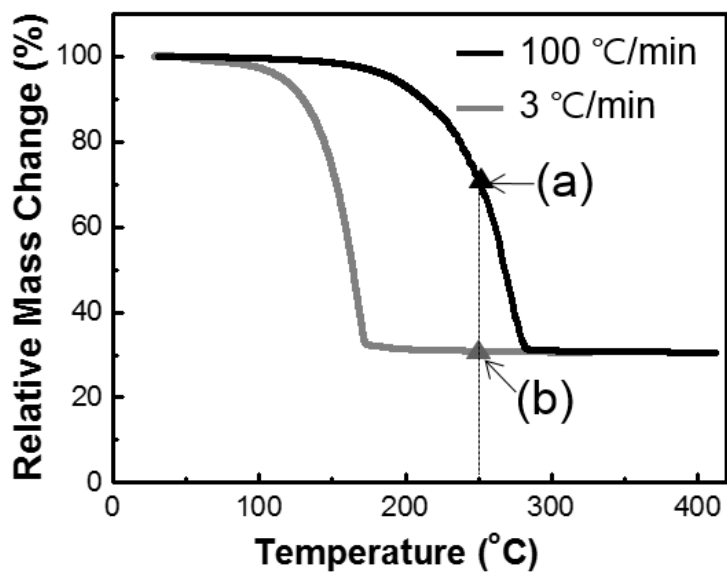


Figure 4.4 Effect of heating rate on removal of organic ligands and microstructure of inkjet-printed Ag films.^{34,35}

Chapter 4: Highly conductive Ag nanoparticle films after moving rapid thermal annealing

decrease in the electrical and mechanical performance of inkjet-printed films, which can be identified by measuring the electrical resistivity.

To identify the effect of the heating rate on the the thermal decomposition characteristics of the ink contents, the mass change was analyzed by TGA during temperature elevation with constant rates of 100 °C/min and 3 °C/min. The 100 °C/min and 3 °C/min rates were the heating rates during the moving rapid thermal annealing and furnace annealing, respectively.

The decomposition of organic additives shifted to a higher temperature during moving rapid thermal annealing compared to conventional annealing, which was confirmed by TGA. This result is in agreement with previous data.⁴⁵ The distinct changes illustrated in Figure 4.3 are the results of different heating schedules. The heating rate of the annealing affects the temperature and the time needed to decompose the organic additives, as identified by TGA.

As the heating rate increased, the thermal decomposition of the organic additives shifted to a higher temperature (an increase of approximately 110 °C). Most of the reduction in mass was due to solvent evaporation from the ink. After the solvent evaporated ($T > 173$ °C (3 °C/min); $T > 285$ °C (100 °C/min)), the mass change was less than 2 %. The protective organic ligand decomposed over a wide temperature range instead of a narrow temperature range as for solvent evaporation. Therefore, the temperature regions in which the two phenomena occurred overlapped. However, the decomposition of the organic ligand during moving rapid thermal annealing shifted to a higher temperature range than that of conventional annealing according to the overall shape of the graph. Except for the Ag contents (30.4 wt%), the solvent evaporation and the decomposition of the organic ligand were complete at 326.7 °C after 101.6 min by furnace annealing and at 412.0 °C after 4.8 min by moving rapid thermal annealing.

Chapter 4: Highly conductive Ag nanoparticle films after moving rapid thermal annealing

Therefore, decomposition time was shortened by a factor of 21, and the heating rate was 33 times greater.

The inkjet-printed Ag films were heated to 250 °C with different heating rates, i.e., moving rapid thermal annealing and furnace annealing, and then cooled to room temperature to identify the effect of the heating rate on the microstructure. The microstructural evolution during cooling was assumed to be negligible, because both samples were cooled under the same conditions.¹⁹ Inter-particle contact between nanoparticles was observed in Figure 4.3 after heating to 250 °C by moving rapid thermal annealing. In Figure 4.3, although the same temperature was reached, coarsened grains were observed after the furnace annealing. The electrical resistivities of the films were 71.6 $\mu\Omega\text{-cm}$ (left in Figure 4.4) and 6.9 $\mu\Omega\text{-cm}$ (left in Figure 4.4). Because most of the organic protective ligand remained, the Ag remained nano-sized, and the resistivity was as high as 45 times that of the bulk. This higher resistivity was caused by the remaining organic ligand in the films, which inhibited the electron transfer among the Ag particles. In furnace annealing, most of the organic ligand decomposed, and the films had a low electrical resistivity less than 5 times that of bulk Ag.

These microstructural changes can be explained by diffusion phenomena during the sintering process. Surface diffusion is the dominant transport mechanism in the low-temperature regime during sintering, and grain boundary diffusion and lattice diffusion, which induce densification, prevail in the high-temperature range.^{43,53} In furnace annealing, surface diffusion is more dominant than in moving rapid thermal annealing. However, the surface area was considerably decreased after the long annealing time of 77 minutes during furnace annealing. The evolution started at the upper part of the films.¹⁹ Therefore, pores became trapped inside the films and grew during annealing, as shown in Figures 4.3. However, in moving rapid thermal annealing, Ag existed as nano-

Chapter 4: Highly conductive Ag nanoparticle films after moving rapid thermal annealing

sized particles at temperatures over 250 °C, and the protective organic ligand decomposed more rapidly at higher temperature than in furnace annealing due to the high heating rate. The pores can escape from the inside of the film easily, and few pores were therefore observed at the surfaces and interfaces of the films. Because grain boundary and lattice diffusion are dominant in the temperature regime of moving rapid thermal annealing, and the volume fraction of the grain boundaries is large due to the nanometer size of the particles, the effect of the densification and grain growth is maximized. In conclusion, metallic films with high density and near-bulk conductivity can be achieved by rapid annealing, which causes the organic ligand to decompose at high temperature within a short time.

Although the temperature shifted to a higher region due to the high heating rate, the total time of exposure to the heat for the removal of the organic ligand was 21 times shorter than in furnace annealing. Therefore, thermal damage to the sample substrate could be decreased.

According to the literature and the results of this study, the effect of the heating rate on the inkjet-printed metal films during annealing was confirmed. Two phenomena were observed during the annealing process of the inkjet-printed metal films: the decomposition of the protective organic ligand and the microstructural evolution of the Ag film. In the first phenomenon, the high heating rate delays the removal of the organic ligand.⁴⁵ Thus, the high heating rate prevents the agglomeration of Ag nanoparticles and causes the microstructural evolution to occur at a higher temperature than in furnace annealing. After the decomposition of the organic ligand, the high heating rate induces the densification of the remaining silver nanoparticles.⁵³

4.6. Film thickness dependence

The effect of the moving rapid thermal annealing on thick inkjet-printed films was investigated by analyzing the microstructures, as shown in Figure 4.5. The films were the same thickness after printing, but the final thickness and cross-sectional and surface microstructures after the two annealing processes showed distinct differences. The final film thickness of the top image shown in Figure 4.3 was 4.5 μm , and that of the bottom one was 6.6 μm .

Nanometer-size pores were observed near the substrate in the thick films annealed with moving rapid thermal annealing; the largest thickness is shown in Figure 4.5. Because the heat transfer by radiation from the lamp was more dominant than the heat transfer by conduction along the substrate, the bottom of the microstructure was no less evolved than the top. However, from the overall pore size and porosity, a higher microstructural density and larger contact area between substrate and film were observed after moving rapid thermal annealing than after furnace annealing. In addition, the new annealing method caused the volume of the printed film to contract approximately 32% more than in the conventional method based on the changes in thickness. From the comparison of the images in Figure 4.5, moving rapid thermal annealing is more effective for obtaining stable microstructures for thick inkjet films than furnace annealing.

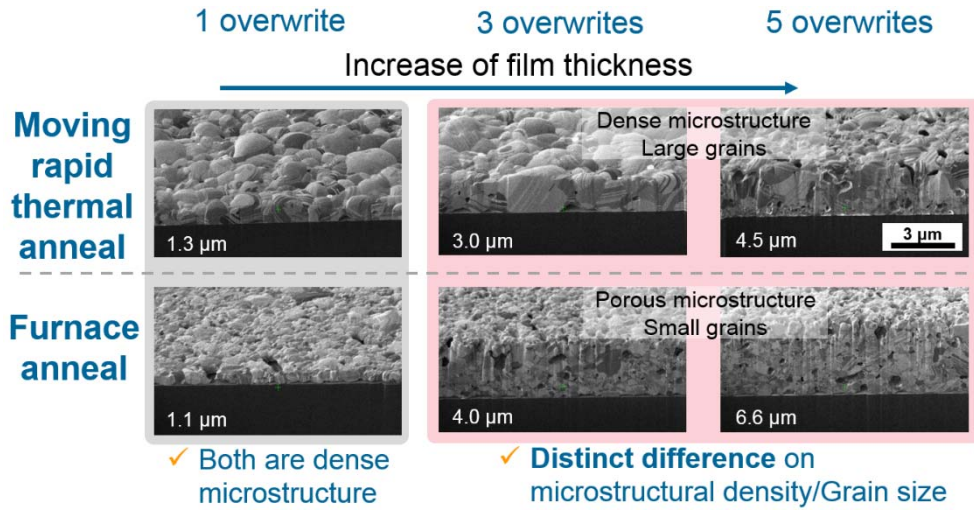


Figure 4.5 Effect of heating schedule and thickness on microstructure of inkjet-printed Ag films.^{34,35}

4.7. Summary

Moving rapid thermal annealing was proposed as a new post-annealing process for inkjet-printed Ag films. When the liquid nanoparticle ink was solidified by heating with a moving halogen lamp, a desirable microstructure and resistivity were obtained in a much simpler and faster process than conventional annealing. This method is also applicable to roll-to-roll processing and beneficial for the fabrication of large-area electronics.

The temperature during moving rapid thermal annealing showed a unique profile, and the peak temperature and the high heating rate determined the microstructure and the properties after annealing. As the power increased, the microstructure of the inkjet-printed films changed from the nanoparticle state to a micron-sized grain structure. The resistivity changes were analyzed and correlated to the decomposition of the organic ligand and microstructural evolution. A dense microstructure with micron-sized grains and the resistivity of bulk silver could be obtained by moving rapid thermal annealing but not by furnace annealing.

This effect was more apparent in thick inkjet-printed films because of the influence of the high heating rate. The high heating rate induces the decomposition of the organic ligand over a higher temperature regime for a shorter time than furnace annealing and thus leads to the densification of the whole film after the elimination of the ligand.

CHAPTER 5

Highly Conductive ITO Nanoparticle Films after Oxygen Partial Pressure-Controlled Annealing

5.1. Introduction

In transparent conducting oxides (TCO), the electron concentration can be increased by doping with other elements or by generating oxygen vacancies. A reducing environment can be beneficial for the conductivity of oxide film, because it can increase the number of oxygen vacancies. However, in solution-processed TCO nanoparticles, especially particles made of indium tin oxide (ITO), a certain amount of oxygen is essential for optimal conductivity. We investigated the distinct effect of the oxygen partial pressure on electron concentration and mobility during annealing using Hall measurements.

ITO is one of the most conductive and widely used transparent electrode materials.^{13,54} ITO films have been prepared by various methods, such as RF sputtering, pulsed laser deposition, vacuum evaporation, and chemical vapor deposition.^{2,55,56} Although these vacuum-based deposition processes are common, interest in solution processes has increased significantly due to their advantages for developing printing or coating

techniques that are low cost, environmentally friendly, and viable at atmospheric pressure.¹⁻⁴

Solution-processed ITO can be produced by metal-organic deposition (MOD) or nanoparticle-based solution methods. MOD uses metal-organic compounds or salts mixed with the desired stoichiometry and dissolved in a solvent.⁴ A nanoparticle solution contains target materials with spherical nano-sized particles suspended in a solvent. Of the two types of solution-processed ITO films, the nanoparticle-based films have many advantages in performance and fabrication processing. First, nanoparticle-based films avoid additional crystallization processes, because the ITO was pre-synthesized in a particle form.^{2,3,5,6} The optimized Sn concentration for doping can be easily achieved, and a lower processing temperature may be possible. Furthermore, nanoparticle films are easier to fabricate as thick films compared to the MOD process.⁸ This represents an advantage over MOD films for the purpose of obtaining low resistance by the geometrical effect, $R = \rho/t$. However, films made from nanoparticle solutions have demonstrated much lower electrical conductivity ($10^{-2} \sim 10^2 \Omega^{-1}\text{cm}^{-1}$) than the sputtered films ($10^4 \Omega^{-1}\text{cm}^{-1}$) or MOD films ($10^2 \sim 10^3 \Omega^{-1}\text{cm}^{-1}$).^{6,8,57,58} Therefore, to produce low-cost and high-performance transparent electrodes, the conductivity of solution-processed ITO nanoparticle films must be improved.

Organic ligands, such as oleic acid¹⁴, myristic acid¹⁵, and poly(N-vinylpyrrolidone) (PVP),¹⁶ are used to coat nanoparticles because they help disperse the nanoparticles. However, they act as insulators that interrupt electron transfer and reduce conductivity when they remain in films at the end of processing.¹⁷⁻²⁰ Thus, these organic ligands must be removed to improve the conductivity of nanoparticle-based films. Ligands are usually removed as gaseous oxidation products during the post-annealing processing; therefore, ambient oxidation is required for post-annealing.^{4,19} However, a reducing atmosphere is

Chapter 5: Highly conductive ITO nanoparticle films after oxygen partial pressure controlled annealing

essential for obtaining a high concentration of oxygen vacancies, which contribute to electron generation through oxygen vacancy formation.^{13,34,59} Therefore, to obtain high electrical conductivity, it is important to optimize the annealing environment during the post-annealing processes.

Removing organic ligands through annealing has been an important issue in metal nanoparticle studies;^{19,20,34} however, it has not been emphasized for TCO nanoparticles. Similar to sputtered ITO films, a reducing atmosphere has been simply used to generate oxygen vacancies in ITO nanoparticle studies.

However, our group first investigated the effect of oxygen partial pressure on electron concentration and mobility. We also enhanced the conductivity of ITO nanoparticle films by systematically controlling the annealing process, which was designed considering two distinct effects.

In this work, we achieved optimal electrical conductivity without losing the transparency of the solution-processed ITO nanoparticle films by controlling the annealing temperature and pressure. We studied the mechanism underlying the conductivity improvement by characterizing the electron concentration and mobility using Hall measurements. The transparency and microstructure of the samples were also analyzed.

5.2. Experimental procedures

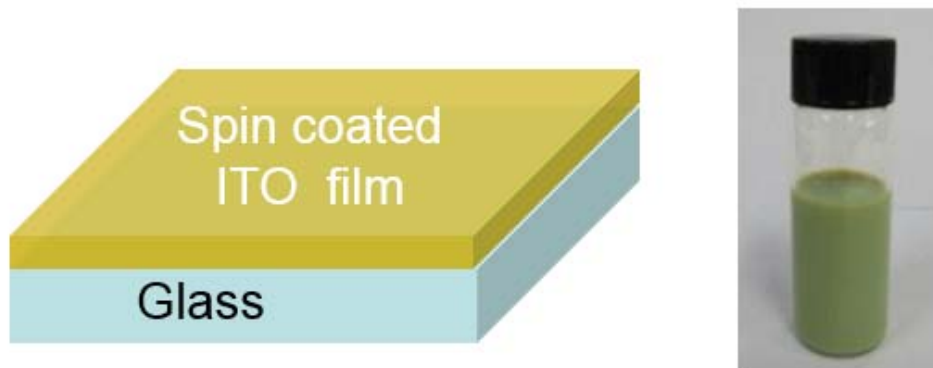


Figure 5.1 A schematic of spin-coated nanoparticle ITO films (left) and ITO nanoparticle solution (right).

The ITO (In_2O_3 : SnO_2 = 90: 10 in wt. %) nanoparticle ink (Advanced Nano Products Co. Ltd) employed in this study had a 20 wt.% solid loading with a 30 nm average particle diameter in ethanol. The ITO ink was spin-coated onto a glass substrate. Coating was performed at 1,000 rpm for 30 seconds. All samples were 300 nm thick, except for the thick films, which were 500 nm or 1 μm . The 300-nm films were achieved using a single spinning process, but the thicker films required multiple coatings to control the thickness. For the multiple coatings, the subsequent layer(s) were spun onto the previous layer(s) without drying. Ethanol was used as the ink solvent because it evaporated quickly, allowing film to solidify rapidly.

After the spin coating, the films were dried in 50 °C air for 1 h in a convection oven (Samheung Instrument). Subsequently, oxygen partial pressure-controlled annealing

Chapter 5: Highly conductive ITO nanoparticle films after oxygen partial pressure controlled annealing

was conducted using a tube furnace with a high vacuum pump. The temperature, time, and oxygen partial pressure ranges were 250 – 950 °C, 1 – 3 h, and 10^{-6} - 1.6×10^2 Torr, respectively. The heating rate was 3 °C/min. The oxygen partial pressure was controlled using the vacuum pump during annealing and was calculated from the pressure inside the furnace by multiplying by 0.21 (the fraction of oxygen in the air). Argon gas was used to control the partial pressure and determine its potential for low cost and practicality.

Electrical properties, such as sheet resistance, electron concentration, and mobility, were obtained using the four-point probe method and the Hall measurement system (BIO-RAD HL5500PC). Samples for the Hall measurements were 1 cm × 1 cm squares with Ag paste contacts at the four corners. The magnetic field was 5,000 G. Optical transmittance was measured for $\lambda = 300 - 800$ nm using UV spectroscopy (Varian Cary-5000 UV-Vis-NIR Spectrophotometer). Nanoparticle ITO films were compared to RF-sputtered films from Wooyanggms Co., Ltd. that had a sheet resistance and thickness of 20 Ω /sq and 80 nm, respectively. The film thicknesses were measured using an alpha step. The surface morphology was investigated with field emission scanning electron microscopy (FE-SEM, Hitachi SU-70). Particle size, porosity, and pore size were calculated using an image analyzer and FE-SEM images. The properties of the residual organic ligand were analyzed using secondary ion mass spectroscopy (SIMS).

5.3. Electrical properties after annealing

The ITO (In_2O_3 : SnO_2 = 90: 10 in wt. %) nanoparticle ink had an average particle diameter of 30 nm and was spin-coated on a glass substrate. Post-annealing was conducted after drying the ITO films at 250 – 550 °C in a vacuum furnace under various oxygen partial pressures that ranged ranging from 10^{-6} - 10^2 Torr; these pressures were achieved by controlling the base pressure during annealing in the vacuum furnace. Figure 5.2 shows the conductivity changes of the ITO films under various annealing conditions. The thickness of the films was 300 nm, and the annealing time was one hour. Interestingly, the conductivity changed by about two orders of magnitude due to changes in the annealing conditions. Generally, increasing the annealing temperature caused the conductivity to increase, in agreement with previous reports.⁸ When annealing at 250 °C, there was little dependence on the oxygen partial pressure. However, when annealing at 400 or 550 °C, the conductivity was maximized at 2.1×10^{-3} Torr. Therefore, the highest conductivity was obtained after annealing at 550 °C under 2.1×10^{-3} Torr. The conductivity value was greatly improved compared to the conductivities of the conventional ITO nanoparticle films.^{6,8,57,58}

As mentioned in Chapter 2, the conductivity of ITO is a product of the electron concentration and mobility. Using Hall measurements, the electron concentration and mobility were determined for each of the samples, as shown in Figure 5.3. The electron concentration of the nanoparticle ITO film increased when the oxygen partial pressure decreased. Electrons in ITO can be produced by external doping, substituting Sn for In. In our samples, we used the same ink, and the Sn concentrations should therefore be the same for all samples. Therefore, changes in the electron concentration are associated with the generation of oxygen vacancies during annealing. Oxygen vacancy generation

Chapter 5: Highly conductive ITO nanoparticle films after oxygen partial pressure controlled annealing

can be explained by the formula written in Kröger-Vink notation^{13,25} in Equation 2.8.

The reduction of oxygen partial pressure drives the reaction and increases both the oxygen vacancies and the electron concentration. As the temperature increased, a higher electron concentration was obtained because the equilibrium constant (K) increased. K is represented in the following equation:²

$$K = [V_O][e^-]^2 p_{O_2}^{-1/2} \quad (5.1)$$

The generation of oxygen vacancy is an exothermic reaction. As the annealing temperature increased, K increased and the electron concentration increased.

The bottom graph of Figure 5.3 shows the mobility changes that occurred during annealing. At higher annealing temperatures, the mobility increased. However, the mobility responded differently to the oxygen partial pressure differently than to the electron concentration. Increasing oxygen partial pressure led to greater mobility but also a lower electron concentration. It is interesting to note that the increase in mobility reaches saturation at approximately 2.1×10^{-3} Torr. Mobility is influenced by the scattering due to impurities, defects, grain boundaries, and pores.² The increased mobility in Figure 5.3 is due to the oxidation and elimination of organic ligands acting as impurities during annealing. In terms of microstructure that is closely related to grain boundaries and pores, mobility changes are explained in Figure 5.9.

Combining the two graphs in Figure 5.3 reveals that the electron concentration decreased and mobility became saturated after the oxygen partial pressure was increased; maximum conductivity could be obtained at 2.1×10^{-3} Torr. To obtain high conductivity with a nanoparticle ITO, the minimum oxygen partial pressure for ligand removal should be used.

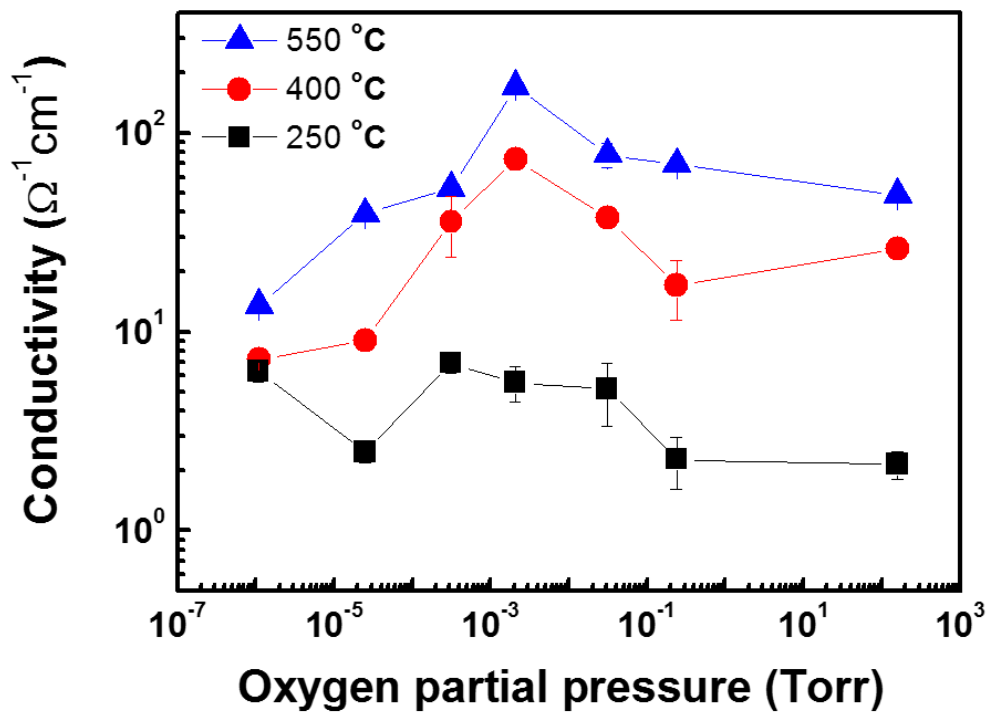


Figure 5.2 Electrical conductivity of nanoparticle ITO films after annealing with various oxygen partial pressures and temperatures.⁶⁰

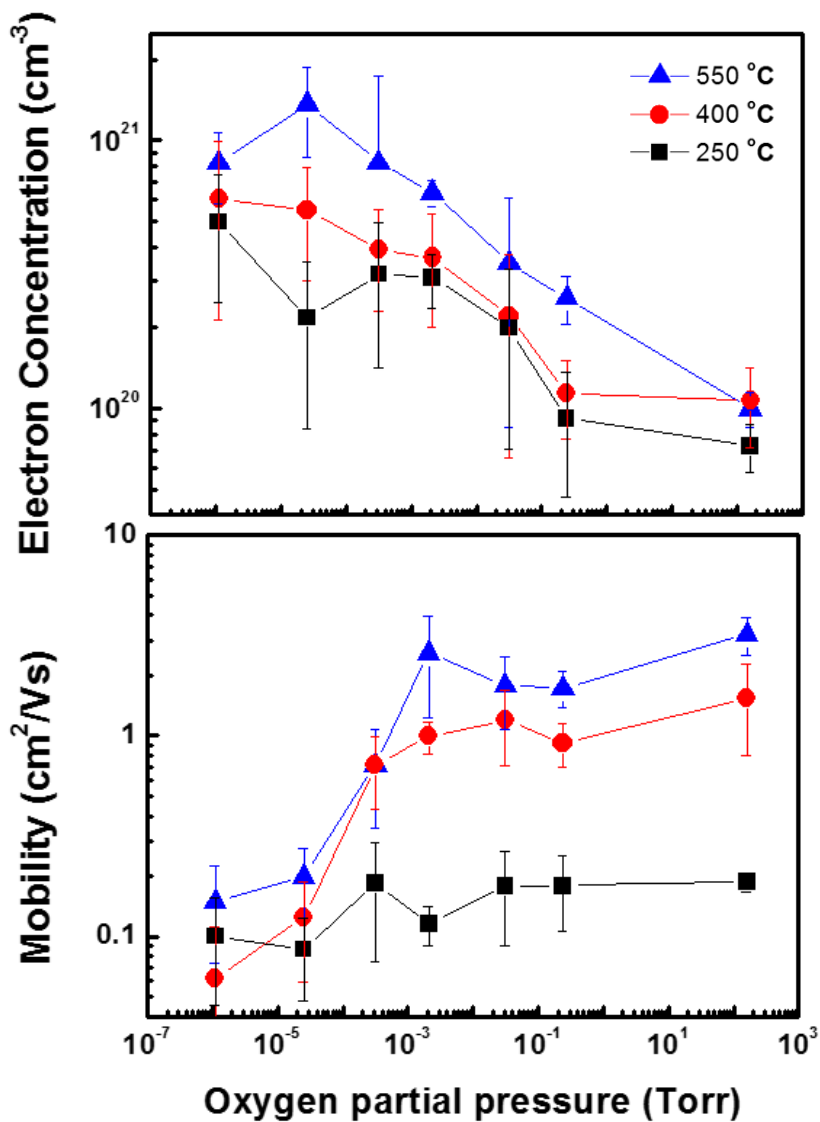


Figure 5.3 Electron concentration and mobility of nanoparticle ITO films after annealing with various oxygen partial pressures and temperatures.⁶⁰

5.3.1. 'N- μ ' diagram

The relationship between electron concentration and mobility in various materials can be easily understood with an 'N- μ ' diagram.⁶¹ Figure 5.4 is a sorting map for the ITO samples produced in this work within an 'N- μ ' diagram. We further compared the electron concentration and mobility data from Figure 5.3 with the data for sputtered ITO films. From Figure 5.4, the complex relationship between the annealing parameters and electrical properties is represented clearly. In the graphs, the oxygen partial pressure is indicated as HV (high vacuum), LV (low vacuum), and Air, corresponding to 1.1×10^{-6} Torr, 2.1×10^{-3} Torr, and 1.6×10^2 Torr, respectively. The three diagonal lines indicate constant conductivity levels ($\sigma = Ne\mu$). The results of annealing at 950 °C are presented in Figure 5.4. Although the condition was harsh, this experiment was conducted to investigate the relationship between mobility and the microstructure change.

As the vacuum increases, the electron concentration increases due to oxygen vacancy formation. Under HV conditions, the electron concentration is as high as the electron concentration of the sputtered film. The mobility varied greatly with the annealing temperature. Although we controlled the annealing conditions, the mobility was still an order of magnitude smaller than the mobility of the sputtered films. Therefore, we concluded that the main cause of the difference in conductivity between sputtered and nanoparticle ITO film was the mobility. Figure 5.4 also shows that electron concentration was primarily determined by oxygen partial pressure, whereas temperature was the dominant annealing parameter for mobility.

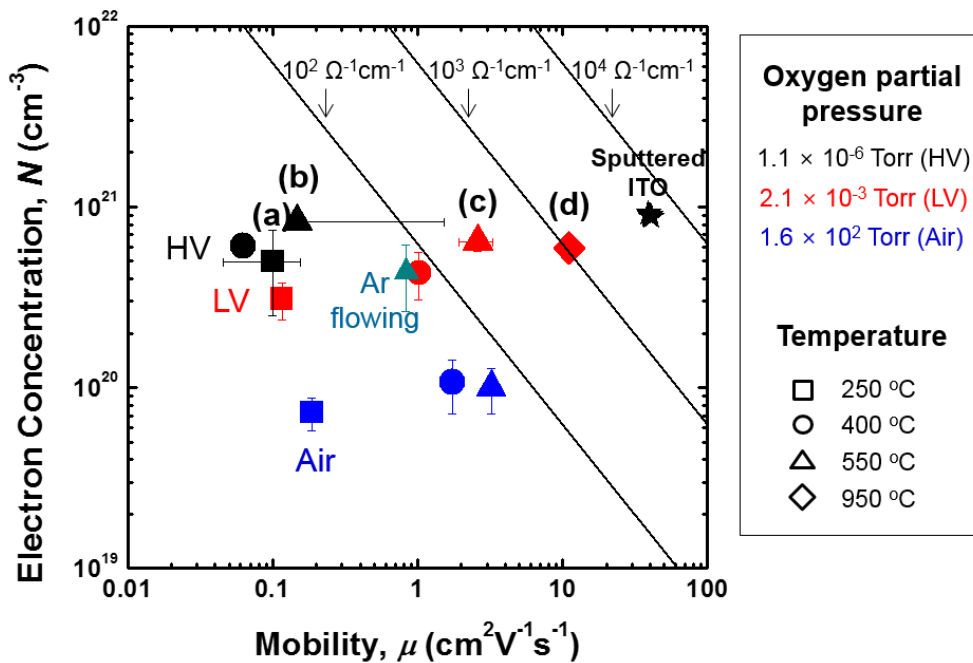


Figure 5.4 Sorting ITO samples in an ‘ N - μ ’ diagram: the nanoparticle ITO films studied in this research and commercially available sputtered ITO films were plotted in a materials space based on electron concentration and mobility values.

60

Chapter 5: Highly conductive ITO nanoparticle films after oxygen partial pressure controlled annealing

Controlling the oxygen partial pressure by modulating the vacuum strength is an appropriate technique for highly controlled experiments and mechanistic studies. However, applying a vacuum during annealing may be difficult in industrial processes.⁶² We also tested the process under an inert gas, such as nitrogen or argon. Annealing under argon was conducted instead of using a vacuum to optimize oxygen partial pressure, and the results are presented in Figure 5.4. The ITO nanoparticle samples were annealed at 550 °C under flowing argon; they exhibited an average mobility of 0.84 cm²/Vs and an average electron concentration of 4.4×10^{20} cm⁻³. These values were similar to the data obtained by annealing under 2.4×10^{-1} Torr. Therefore, the performance was expected to be enhanced when the oxygen concentration was decreased during annealing. When the annealing atmosphere was modulated, the electrical properties of the ITO nanoparticle films were improved under both inert gas and vacuum annealing.

5.3.2. Impurity analysis

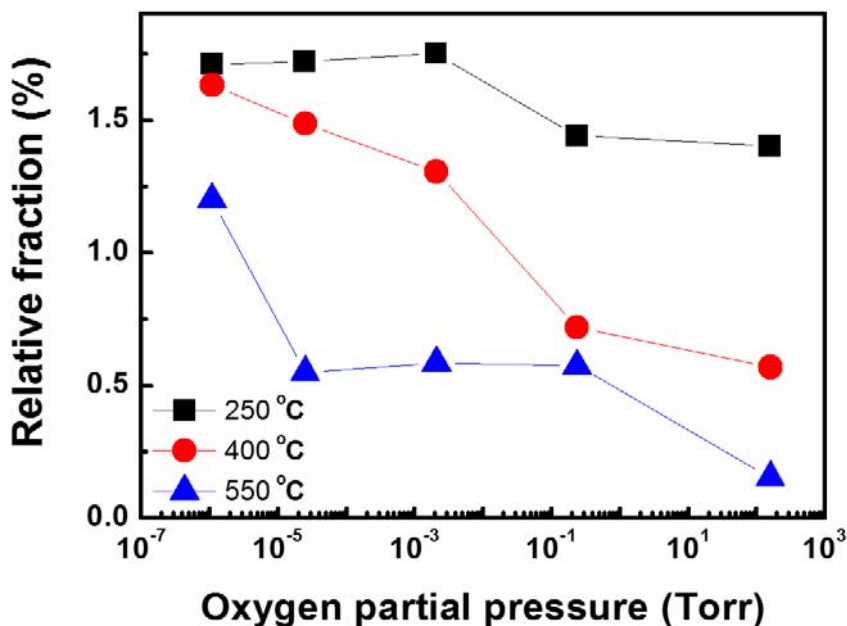


Figure 5.5 Relative mass fraction of carbon after annealing with various temperatures and oxygen partial pressures measured by SIMS analysis.⁶⁰

As discussed, the mobility is the key parameter limiting the conductivity of the nanoparticle ITO films. The main reasons for the limited mobility in nanoparticle ITO films relative to sputtered ITO films are residual organic ligands and the microstructure of the films.

In the nanoparticle films, the remaining organic ligands act as impurities and negatively affect mobility. The state of organic ligands varies with the annealing condition. To confirm that the organic ligand was removed during annealing, secondary ion mass

Chapter 5: Highly conductive ITO nanoparticle films after oxygen partial pressure controlled annealing

spectroscopy (SIMS) analysis was performed, as exhibited in Figure 5.5. The change in the intensity of the carbon atoms after the annealing process was assumed to be directly proportional to the changes in organic ligand. The intensity of the carbon was calculated by summing the intensity values of the carbon in hydrocarbons, C_xH_y . The masses of the carbon, indium, and tin were calculated by multiplying their intensities by their atomic weights. The ratios of the carbon mass to the masses of indium and tin were compared (we refer to these ratios as the 'relative mass fractions' of carbon).⁴⁶ Figure 5.5 shows the relative mass fractions of carbon plotted as a function of annealing temperature and oxygen pressure. As the temperature and oxygen partial pressure increased, the relative fraction decreased. Therefore, large amounts of organic ligand were removed. At higher temperatures, larger amounts of organic ligand were converted into byproducts. When the amount of oxygen was sufficient to react with the ligand (1.6×10^2 Torr (as in Air)), the ligand transformed into gaseous products, such as H_2O and CO_2 and was removed from ITO films.

The trend in Figure 5.5 is roughly the inverse of the trend observed for mobility in Figure 5.3, which indicates that the remaining carbon is the main source for scattering. Interestingly, in 2.1×10^{-3} Torr at 400 °C and in 2.1×10^{-3} - 2.4×10^{-1} Torr at 550 °C in Figure 5.3, the mobility was higher than what was expected from the data in Figure 5.5. The difference between the SIMS and the mobility change data might be caused by the microstructural difference, which is another important factor affecting mobility.

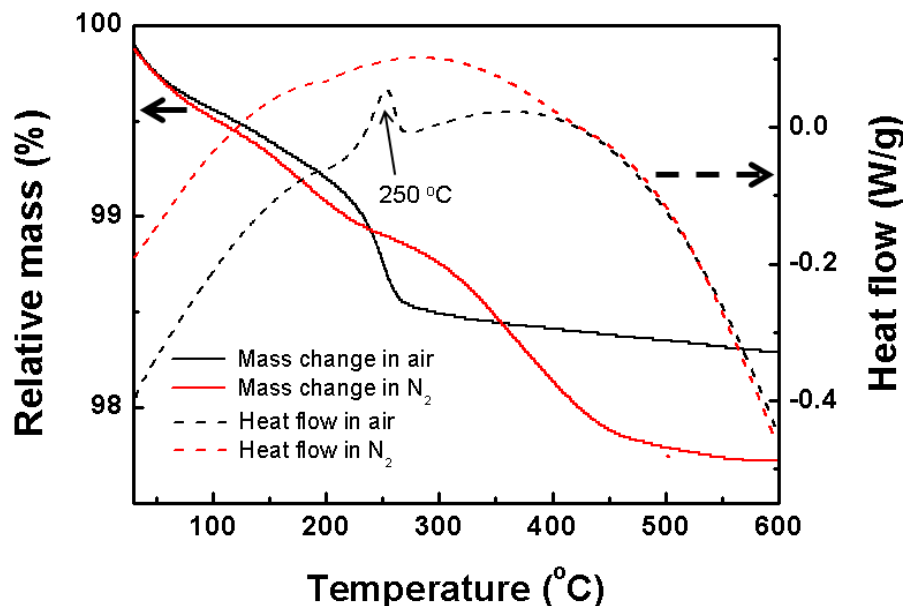


Figure 5.6 Relative mass change of dried ITO nanoparticle powder under air and nitrogen atmospheres.

To investigate the relationship between the decomposition of organic ligand and the mobility change in Figure 5.3, TGA was conducted. The thermal properties of ITO nanoparticles were analyzed by TGA under air and nitrogen ambient. To obtain accurate decomposition temperatures and quantities of organic ligand, the solvent of ITO ink, which accounted for the majority of the total mass, was evaporated before analysis.

In ambient air, 1.5 % of the mass decrease and an exothermic peak as a result of the ligand removal by oxidation were observed at 251 °C. However, the peak corresponding to ligand removal was not detected in this temperature regime under a nitrogen atmosphere lacking oxygen; the removal was shifted to higher temperature. This indicated that carbon compounds (organic ligands) reacted with oxygen in the air and

were removed at 251 °C.^{3,46} In the nitrogen atmosphere, a larger mass change was observed than in air containing oxygen, which may be due to dissociation.⁶³

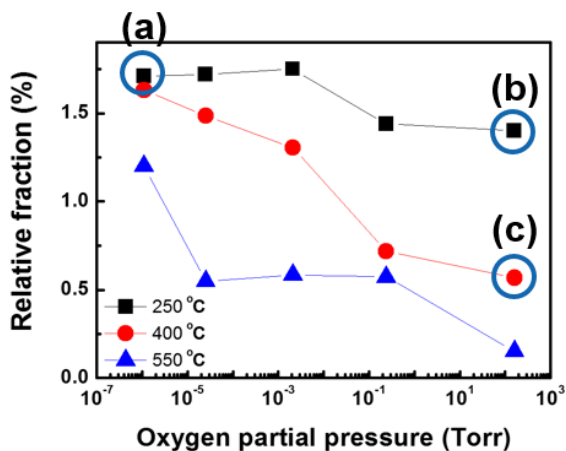


Figure 5.7 Inverse of SIMS data (y axis is an inverse of Figure 5.5). (a), (b), and (c) are the points in Figure 5.4. For easy analysis of the effect of impurities on mobility, the inverse of SIMS data are represented.⁶⁰

5.3.3. Microstructure

The microstructure of the ITO nanoparticle films was analyzed using field emission scanning electron microscopy (FE-SEM). Figure 5.9 illustrates the microstructure of the samples after annealing at (a) 250 °C under HV (1.1×10^{-6} Torr), (b) 550 °C under HV (1.1×10^{-6} Torr), (c) 550 °C under LV (2.1×10^{-3} Torr), and (d) 950 °C under LV (2.1×10^{-3} Torr). These samples are also marked (a), (b), (c), and (d) in Figure 5.4. Before annealing, ITO nanoparticles were observed by TEM, as shown in Figure 5.8. The initial particle size was approximately 30 nm.

After annealing at 250 °C and 550 °C, the morphologies were quite similar. The grain growth was negligible, and many pores were observed. Figure 5.9 (a), (b), and (c) show approximately 33.2 nm particles and approximately 6.6 % of surface porosity with 17.2 nm pores (average). Significant changes in the microstructure only occurred after annealing at high temperature (950 °C under LV), as presented in Figure 5.9 (d). The coarsened particles and some large clusters containing individually connected nanoparticles (white arrow) were observed. Under this condition, the particle size, porosity, and average pore size were 49.1 nm, 5.7 %, and 22.8 nm, respectively. As the temperature increased, the microstructure changed, including particle growth and pore elimination.¹⁹ In our nanoparticle ITO films, these observable changes occurred at higher temperature (950 °C). These changes were responsible for the increase of conductivity (mainly the mobility) of this sample. Obtaining high-density microstructures in the ITO nanoparticle films to enhance mobility is practically difficult in the low temperature region because the temperature must be above 1200 °C.⁶³

At 550 °C, little difference was observed between the images in Figure 5.9 (b) and (c), but mobility increased by more than an order of magnitude. Some of these changes can

be explained by the ligand removal. However, for the experiments at 400 °C under LV and 550 °C under HV, the SIMS relative fraction showed similar values but still demonstrated significant differences in mobility. We think this difference might be caused by the contact between the particles. During the sintering process, contact and necking occurs before coarsening.^{64,65} Necking does not influence the overall microstructural parameters, such as the particle and pore sizes, but greatly impacts the mobility, because electrons can move between these connected regions.^{19,46} Because the nanoparticles were covered with organic ligands, necking among the particles can only occur after the ligand was removed.

As for the crystal structure of the solution-processed ITO films, X-ray diffraction in Figure 5.10 showed a cubic structure for ITO. The ITO nanoparticle film was initially crystalline, and crystallinity was only slightly improved by the annealing process. Phase change was not a crucial factor in our system.

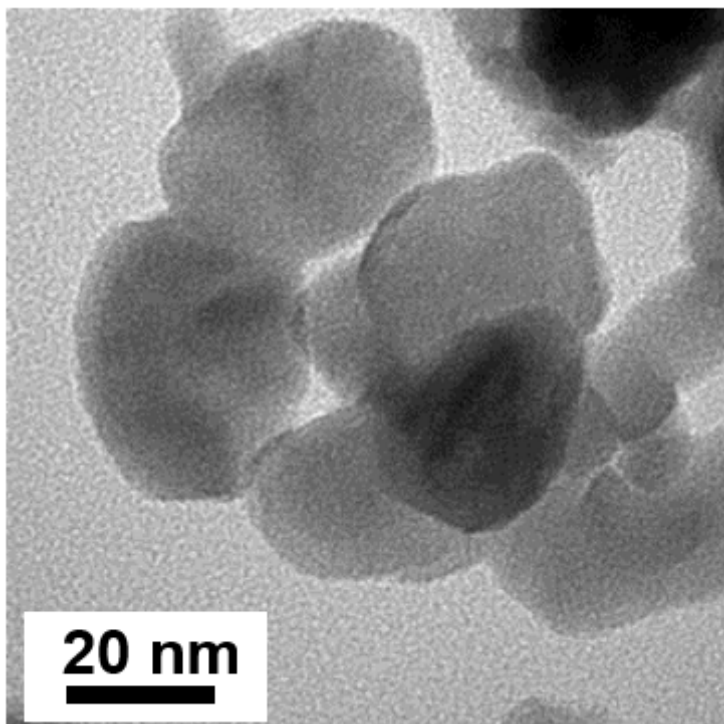


Figure 5.8 A TEM image of ITO nanoparticles before annealing.

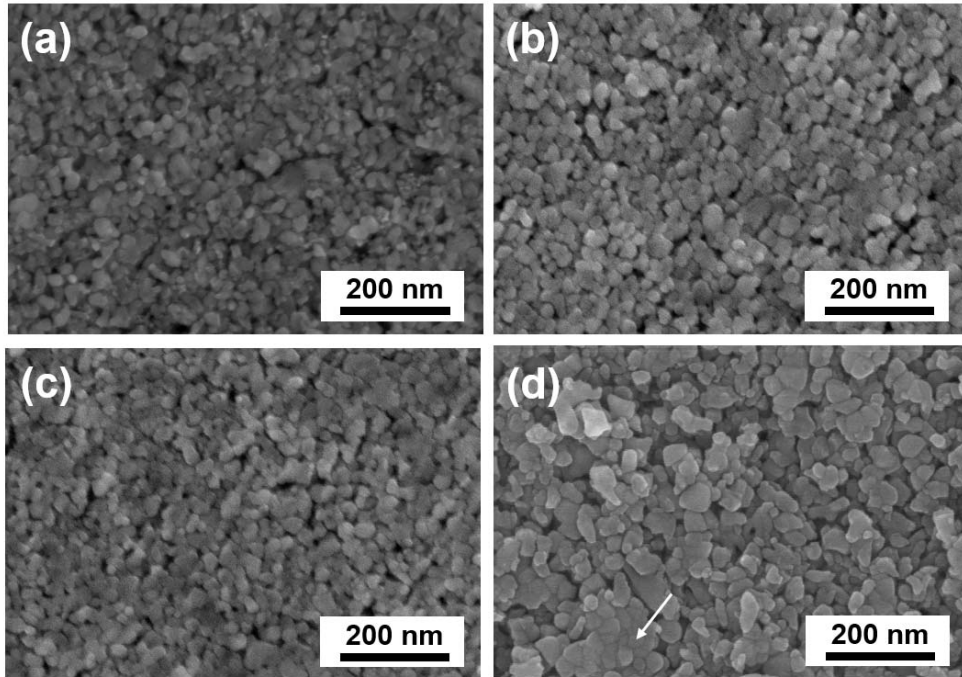


Figure 5.9 Microstructural images of nanoparticulate ITO films. FE-SEM images after annealing at (a) 250 °C under HV, (b) 550 °C under HV, (c) 550 °C under LV, and (d) 950 °C under LV. (Marked (a), (b), (c), and (d) in Figure 5.5).

60

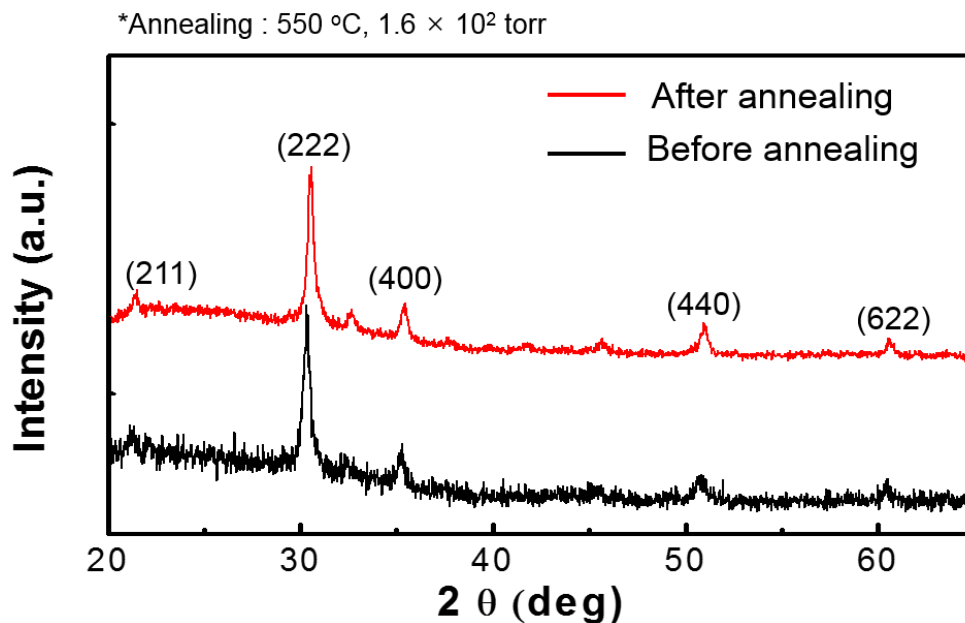


Figure 5.10 XRD patterns of nanoparticulate ITO films before and after annealing.

5.4. Optical transmittance

Optical transparency is also an important characteristic in materials used for transparent electrodes. The transmittance of the solution-processed nanoparticle ITO films in the visible spectrum is presented in Figure 5.11. Most of the films displayed excellent transparency (over 93 %); transparency was calculated by integrating the spectral transmittance over the visible wavelength range (from 380 nm to 780 nm). As indicated by the inset pictures, the nanoparticle ITO samples showed transparency comparable to bare glass after annealing under the appropriate oxygen partial pressure. However, the transparency degraded under HV at 550 °C because a carbon residue formed after the thermal pyrolysis of the organic ligand. At high temperatures, thermal pyrolysis occurs at low oxygen partial pressure. The molecular structure of the ligand was destroyed, and volatile products and solid residues were generated.^{58,66,67} The color of this sample was black. The carbon residues on ITO films were significant event when organic ligand was not thermally pyrolyzed and transmittance was not degraded, such as under 250 °C annealing. More carbon residue was generated by pyrolysis under higher temperature and lower oxygen partial pressure, causing transmittance to decrease and the samples to darken in color. The degraded transmittance was not observed under the same conditions followed by 550 °C annealing under air; the ligand was effectively eliminated by oxidation. Except for this case, the oxygen partial pressure and temperature did not strongly affect transmittance.

In Figure 5.11 (b), the transmittance of the 300 – 340 nm wavelength range is plotted to demonstrate the band gap movement as a function of annealing conditions. According to the Burstein–Moss model, the increase in the optical band gap was caused by the low energy states being filled in the conduction band by the doped electrons. This Burstein–

Moss shift (ΔE^{BM}) relates directly to the electron concentration (N).^{27,68,69} High electron concentrations resulting from low oxygen partial pressure annealing might be identified by the extent of the ultraviolet cut-off shift in the transmittance graph displayed in Figure 5.11 (b). The electron concentration data in Figure 5.3 agreed with this result

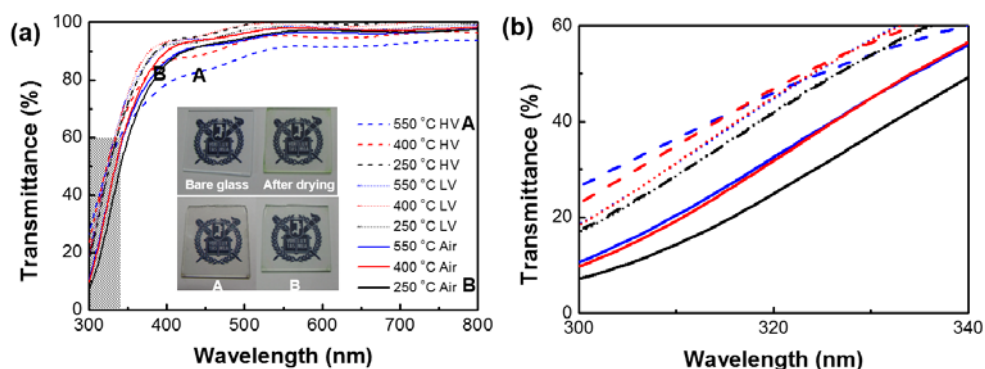


Figure 5.11 Transmittance in the visible spectrum after oxygen partial pressure-controlled annealing. The inset pictures show the optical transparency of the ITO nanoparticle electrodes under various partial pressures and temperatures. A and B mark the samples annealed under 550 °C HV and 250 °C Air, respectively. (b) Transmittance in the 300–340 nm spectral range.⁶⁰

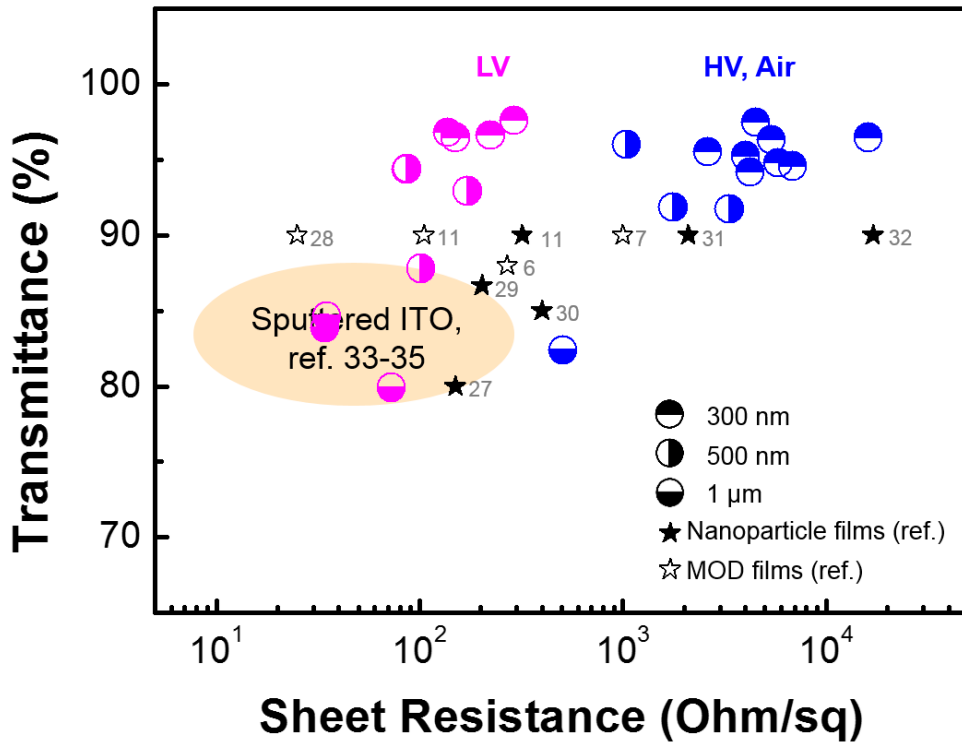


Figure 5.12 Performance comparison between our ITO nanoparticle electrodes and sputtered, MOD, and nanoparticle reference electrodes. ^{1,3,8,60,70-78}

The transmittance and sheet resistance of the nanoparticle ITO films with various thicknesses (300, 500, 1,000 nm) were measured and are presented in Figure 5.12. Various reference data, such as data from the sputtered, MOD, and nanoparticle ITO films, are also shown in Figure 5.12. The full and empty stars denote the reference data for the nanoparticle and MOD films, respectively. MOD films generally have better electrical and optical properties than nanoparticle films. Differences between the MOD and nanoparticle films were caused by their coating morphology.⁸ Circles denote our

Chapter 5: Highly conductive ITO nanoparticle films after oxygen partial pressure controlled annealing

experimental data. Samples with various thicknesses are represented by differently shaded circles. After identical annealing processes, the points for the graphed films may be different because thicker films have a lower sheet resistance and transmittance. Our samples display properties superior to the reference data for the nanoparticle films and comparable to the data for MOD films due to the modulated partial pressure during annealing. Samples annealed under LV exhibited much lower sheet resistances than samples annealed under HV and Air, but transparency is maintained because LV is the optimal oxygen partial pressure to maximize oxygen vacancy generation and sufficiently remove the organic ligands. Therefore, the electrical properties were improved two orders of magnitude while maintaining transparency by optimizing the oxygen partial pressure, as demonstrated by the data from our 300 nm thick samples in Figure 5.12.

In transparent electrodes, conductivity and transparency are both critical factors that should be considered simultaneously. By calculating the figure of merit value, the performance as a transparent electrode can be quantified.²⁶ The equation for the figure of merit of a transparent conductor is described in Chapter 2. This equation contains the effect of both electrical and optical properties. For a given material, figure of merit is only a function of thickness. Generally, the sheet resistance is used when the transmittance is 90 %.^{26,27} The figure of merit was $5 \times 10^{-3} \Omega^{-1}$ for the commercial ITO sputtered electrode. The maximum value found in this work was $5.4 \times 10^{-3} \Omega^{-1}$, which is similar to the sputtered ITO electrode and excellent compared to the other reference materials for transparent electrodes.^{76,79,80}

5.5. Summary

Highly conductive and transparent ITO nanoparticle films were developed by controlling the oxygen partial pressure during annealing. The oxygen partial pressure is an important factor affecting the electrical properties of solution-processed ITO nanoparticle films. This is because a reducing atmosphere is beneficial to increase the electron concentration, but an oxidizing atmosphere is essential for high mobility. Mobility is controlled by impurities related to the elimination of organic ligands covering nanoparticles and the microstructure evolution relevant to necking, grain growth, and densification. The maximum conductivity of ITO nanoparticle films in this work was $313 \Omega^{-1}\text{cm}^{-1}$ and the figure of merit was $5.4 \times 10^{-3} \Omega^{-1}$. The electron concentration was comparable to the data for the sputtered films, but mobility was lower than in the sputtered films. These differences originated from the nano-sized grains and numerous pores inside the films. The electron concentration was primarily affected by the oxygen partial pressure, whereas temperature was the dominant parameter for mobility. Conductivity enhancement was also achieved in an argon gas flowing environment, which was cheaper and easier to operate than a vacuum. If the conductivity of nanoparticle ITO were improved to match the conductivity of the sputtered films using this technology, then the fabrication of low-cost ITO based devices could become feasible. This method can also be applied to other solution-processed oxide nanoparticle films.

CHAPTER 6

High Mobility Spray-Coated In₂O₃-based Films

6.1. Introduction

Transparent conducting oxide is an important material in electronic devices such as flat panel displays, photovoltaic cells, organic light emitting diodes, thin film transistors, and smart windows. ITO is the most widely used TCO and shows high conductivity and transparency. However, it has a high electron concentration, N , but low mobility, which results in a narrow transparency window because of low transmittance in the near-infrared (NIR) region. In photovoltaic applications that have wide-range spectral sensitivity, there should be optical loss in the NIR region by free carrier absorption. Electronic devices commonly require high conductivity but low N , which requires mobility to increase.

Therefore, studies about increasing mobility have received increasing attention recently. Mobility is expressed in the equation: $\mu = \tau e / m^*$; to achieve high mobility, increasing τ or decreasing m^* is required. There are many studies concerning the improvement of film quality by controlling the deposition and annealing processes (τ control). It has been found that specific dopants such as Mo, Ti, W, and Zr in In₂O₃ (m^* control) can increase

mobility significantly compared to Sn.¹⁰

Among various dopants, Mo shows the best mobility increase without conductivity loss due to its electronic band structure (d-orbital hybridization), slightly smaller ionic radius than In, large valence difference, and high Lewis acid strength.

Conventional vacuum-assisted deposition has many problems, and solution processing can be a good alternative. There are two types of starting solution. Nanoparticle solution has many merits but shows low mobility. This phenomena intensifies in oxide materials that have high melting temperatures.⁶⁰ In solution processing, annealing is a necessary step after deposition. The control of oxygen partial pressure is important because characteristics of oxide materials are changed remarkably by the annealing atmosphere.

⁶⁰

In this study, Mo, W, and Zr-doped In₂O₃ films were fabricated to obtain high mobility while maintaining conductivity. Spray coating was used for the deposition of solution; this method was appropriate for obtaining high mobility and made the introduction of various dopants and concentrations straightforward.

The interesting focus of this research is the strategy for the improvement of mobility for solution-processed In₂O₃-based TCOs. Both the choice of appropriate dopant and the fabrication of high-quality film are important. Mobility can be increased by optimizing the dopant concentration and microstructure control. After oxygen partial pressure-controlled annealing, a high electron concentration was obtained by the generation of oxygen vacancy. The mechanistic study of spray-coated, high-mobility IMO films was investigated systematically. Using this concept, W and Zr were also used as dopants in In₂O₃, and high conductivity and mobility were found. By comparing other fabrication processes and dopants (ITO), guidelines for the production of low-cost, high mobility-film is suggested.

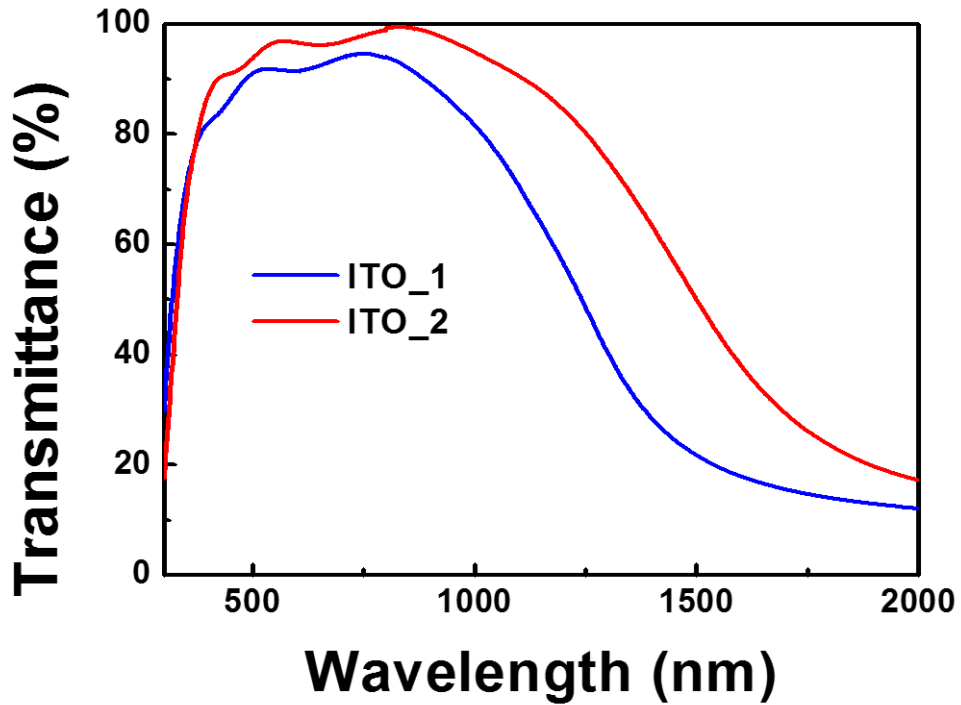


Figure 6.1 Optical transmittance of nanoparticle ITO films. Annealing atmosphere made the difference of electron concentration in the samples. ITO_1 had a higher electron concentration than ITO_2. High electron concentration creates the narrow transparency window.

6.2. Experimental procedures

Indium III chloride (InCl₃; Aldrich) was used as the source for indium, whereas molybdenum, tungsten, and zirconium doping were achieved with molybdenum V chloride, tungsten VI chloride, and zirconium IV chloride (MoCl₅, WCl₆, ZrCl₄; Aldrich), respectively. ITO film was also spray-coated using Tin(IV) chloride pentahydrate (SnCl₄·5H₂O; Aldrich) to compare with other films. The size of the glass substrate is 20×20×7 mm³. The substrate temperature was 345 - 495 °C. The precursor concentration was 0.025-0.1 M, and the solvent is mixture of distilled water (DIW) and ethanol in various ratios. WCl₆ was dissolved in NH₃OH+DIW solvent.⁸¹ For doping, MoCl₅, WCl₆, and ZrCl₄ solution were added to the InCl₃ starting solution. The amount of dopant precursor was varied to achieve different dopant/(dopant+In) atomic ratios up to 6.5 at. %. The final solution was sprayed onto preheated substrates using the spray pyrolysis experimental setup (Nano Spray Coater). The volume of spray solution was varied from 10 ml to 20 ml. Generally, 12.5 ml solution was spray-deposited in 30 minutes.

After the spray coating, the films were annealed to remove organic additives and improve the properties. Oxygen partial pressure-controlled annealing was conducted using a tube furnace with a high vacuum pump. The temperature and time were fixed at 550 °C, 1 h. Oxygen partial pressure ranged from 10⁻⁶ - 4 × 10⁻¹ Torr. The heating rate was 3 °C/min. The oxygen partial pressure was controlled using the vacuum level during annealing and was calculated from the pressure inside the furnace by multiplying by 0.21 (the fraction of oxygen in the air).

Electrical properties, such as sheet resistance, electron concentration, and mobility, were obtained using the four-point probe method and the Hall measurement system

(BIO-RAD HL5500PC, Ecopia Hall measurement system HMS-3000). Samples for the Hall measurements were 1 cm × 1 cm squares with Ag paste contacts at the four corners. The magnetic field was 5000 G. Optical transmittance was measured for $\lambda = 300 - 2500$ nm using UV spectroscopy (Varian Cary-5000 UV-Vis-NIR Spectrophotometer). Spray IMO films were compared to spray-coated ITO and RF-sputtered ITO films from Wooyangms Co., Ltd. that had a sheet resistance and thickness of 20 Ω /sq and 80 nm, respectively. The film thicknesses were measured using an alpha step. The surface and cross-sectional morphology were investigated with field emission scanning electron microscopy (FE-SEM, Hitachi SU-70) and transmission electron microscopy (TEM, Tecnai F20). X-ray diffraction (XRD) patterns were obtained using an X-ray Diffractometer (D8-Advance, BRUKER MILLER Co.). Chemical characteristics were analyzed by X-ray photoelectron spectroscopy (XPS, PHI 5000 VersaProbe, Ulvac-PHI).

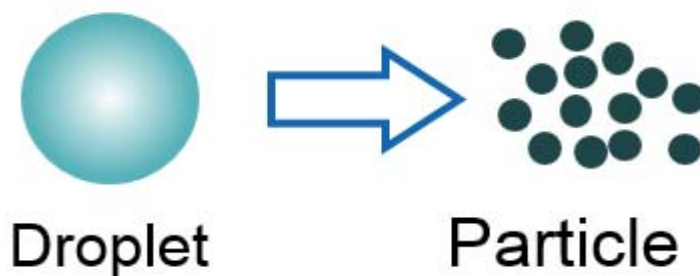


Figure 6.2 A Schematic of droplet-to-particle transition in the spray-coating process.

6.3. Effects of spray-coating parameters

6.3.1. Solvent and precursor concentration

Optical transparency improves significantly at the same substrate temperature as the ratio of ethanol, which evaporates at a lower temperature, in the solvent increases. In Figure 6.4, university insignia can be seen more clearly through higher ethanol ratio films. It was reported that transmittance was low, and films with milky white heaps were obtained.²⁴ However, high resistance ($\sim 10^6 \Omega/\text{square}$) was measured in 90 % ethanol film. To determine the reason for this high resistance, the microstructure was analyzed. In the SEM images of Figure 6.5, a more uniform but discontinuous microstructure was observed with the high ethanol ratio. Low resistance and high transparency were obtained by increasing the precursor concentration from 0.025 to 0.1 M, as seen in Figure 6.3

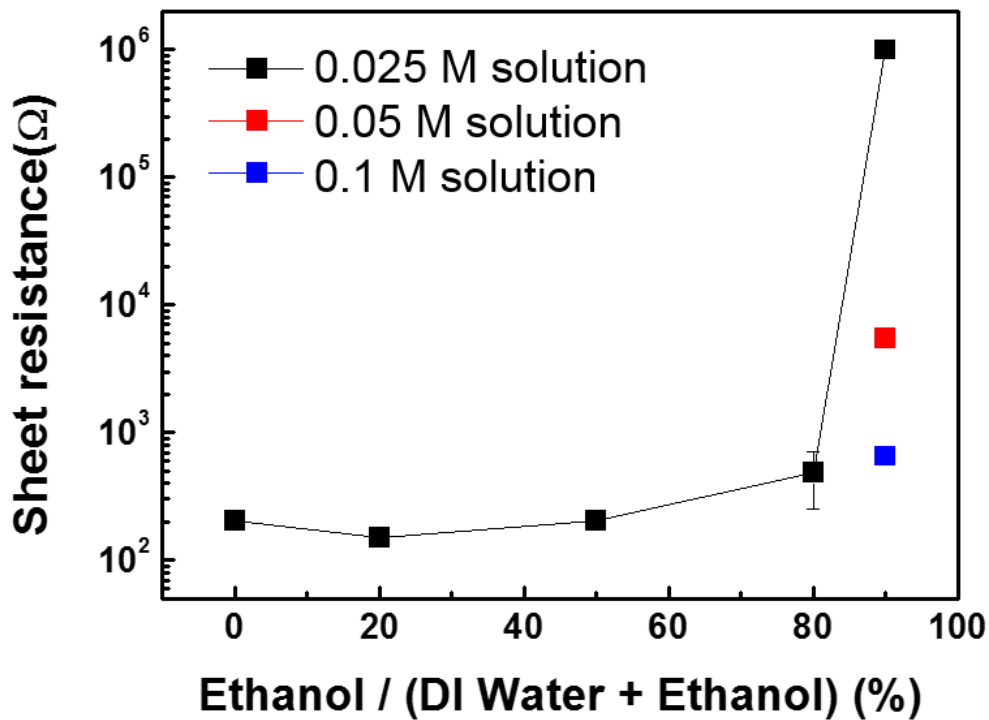
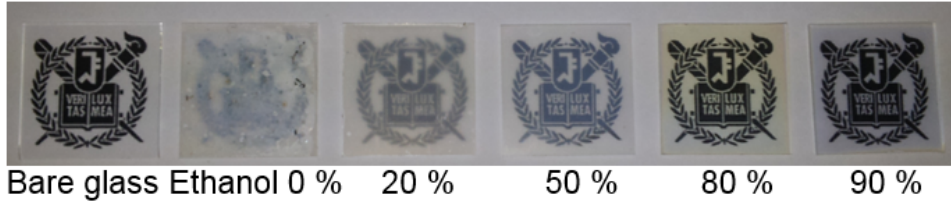


Figure 6.3 Sheet resistance of spray-coated In_2O_3 films as a function of solvent mixture ratio and precursor concentration.

✓ Before annealing



✓ After annealing $<2 \times 10^{-2}$ Torr $>$



Figure 6.4 Optical transparency of spray coated In_2O_3 films with varied solvent mixture ratios before and after 2×10^{-2} Torr annealing.

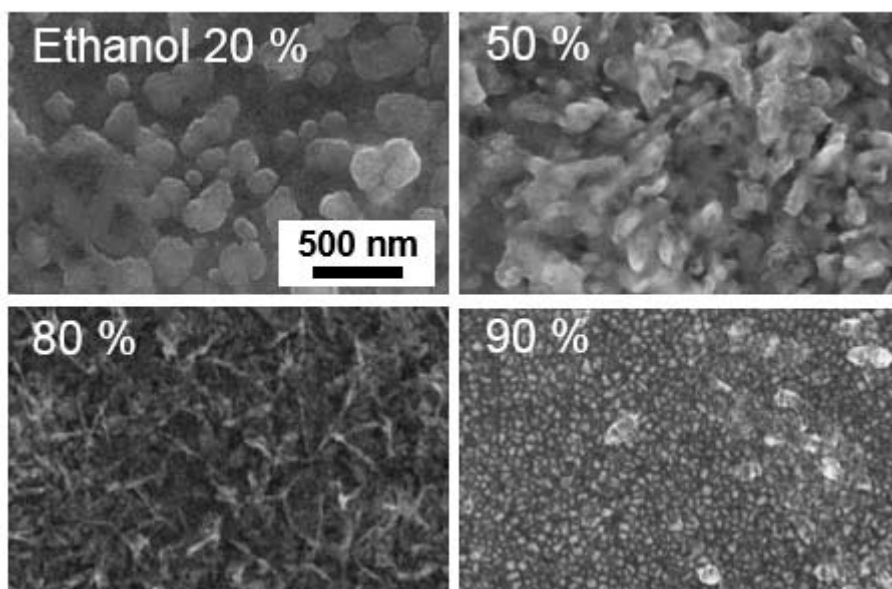


Figure 6.5 Microstructure of In_2O_3 films with 20 %, 50 %, 80 %, and 90 % ethanol.

6.3.2. Substrate temperature

As substrate temperature increased, conductance and mobility increased. The effect of temperature on electron concentration was minor, and the doping efficiency was not related to the substrate temperature in this system. Oxygen partial pressure affects the electron concentration by controlling oxygen vacancy.

According to J. Prince, atomized droplets emitted from the spray coater are vaporized on the heated substrate and converted to solid films with a similar mechanism to low temperature chemical vapor deposition (LPCVD). A 395 °C substrate temperature is not high enough for the solution to be vaporized. Above 440 °C, a highly uniform film is produced, and grain growth is observed with increasing temperature. Mobility increased with temperature, because the microstructure is evolved and defects are eliminated.

Films deposited over 345 °C are highly crystalline and not amorphous. The effect of substrate temperature on crystallinity is negligible based on Figure 6.8, the (400) peak in XRD data of films increased at 495 °C. However, there are no reports about the effect of a preferred orientation on the film properties, except the surface morphology.⁸²

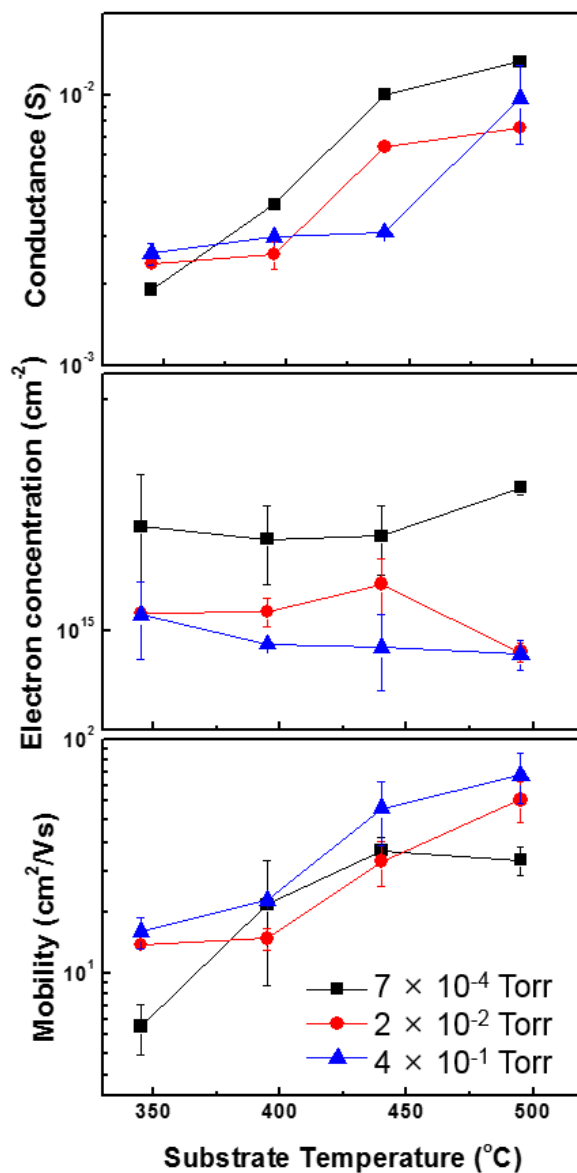


Figure 6.6 Variation of electrical conductance (top), sheet electron concentration (middle), and mobility (down) of spray-coated 1 at. % IMO films as a function of substrate temperature and oxygen partial pressure during annealing.

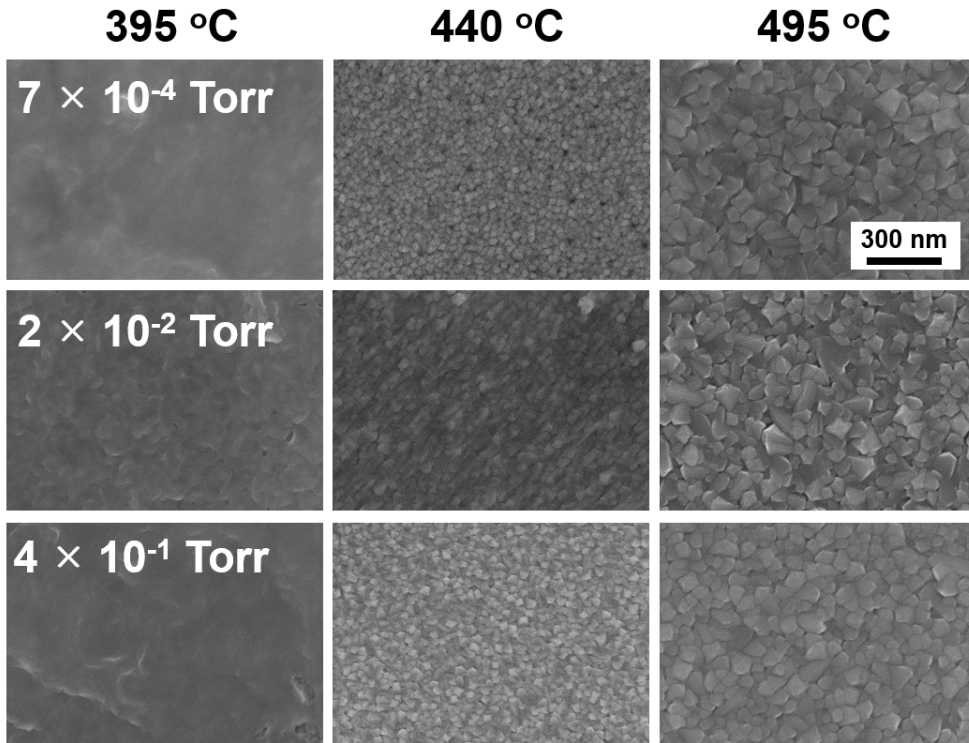


Figure 6.7 Microstructural images of 1 at. % IMO films deposited at different temperatures and different oxygen partial pressures. Annealing temperature and time were 550 °C, 1 h.

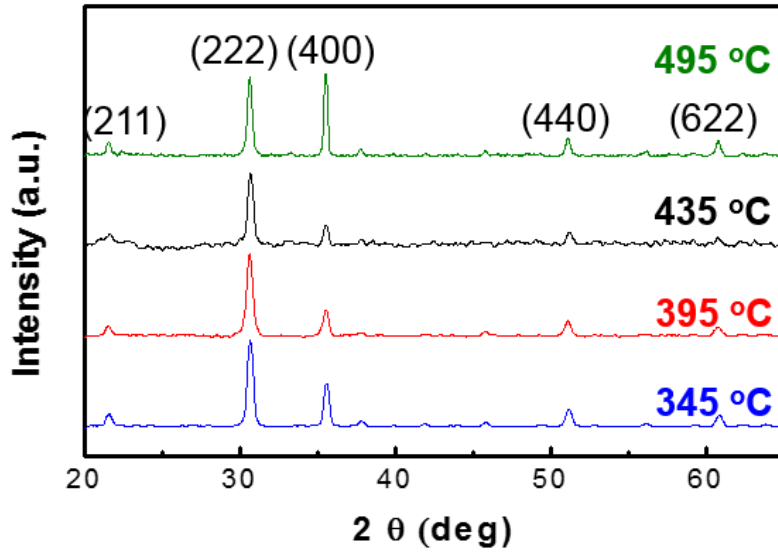


Figure 6.8 XRD patterns of In_2O_3 films deposited at different substrate temperatures: 345 °C, 395 °C, 435 °C, and 495 °C.

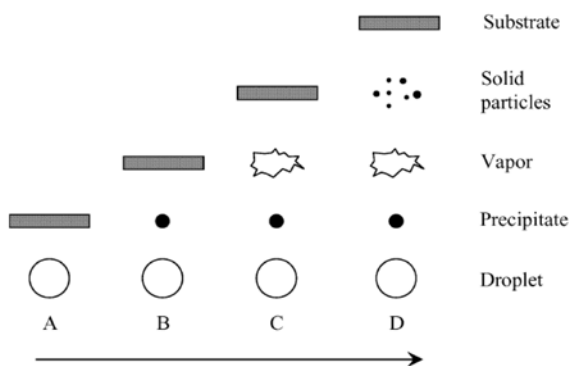


Figure 6.9 Description of the deposition processes initiated with increasing substrate temperature.²³

Viguie and Spitz suggested the above processes that occur with increasing substrate temperature. The x-axis shows the substrate temperature. In the lowest temperature range (process A), the droplet splashes onto the substrate and decomposes. At higher temperature ranges (process B), the solvent of precursor solution evaporates completely during the flight of the droplet, and precipitates hit the substrate, where decomposition occurs. At even higher substrate temperatures (process C), the solvent also evaporates before the droplets reach the substrate. Then, the solid precipitates melt and vaporize without decomposition, and the vapor diffuses onto the substrate to undergo a CVD process. At the highest temperature ranges (process D), the precursor vaporizes before it reaches the substrate, and consequently the solid particles are generated after the chemical reaction in the vapor phase. It is believed that processes A and D lead to rough or non-adherent films. Adherent films were obtained by CVD at low temperatures (process C). However, type A or B processes also allow the formation of high-quality

adherent films. Moreover, process C rarely occur in most spray pyrolysis depositions, because either the deposition temperature is too low for the vaporization of a precursor, or the precursor salt decomposes without melting and vaporization.

6.3.3. Solution volume

To study the effect of surface scattering on electrical or optical properties, thickness dependence was investigated. Thickness was controlled by the volume of solution used for deposition. In Figure 6.10, crystal size increased with the thickness, which was similar to sputtered films.⁸³ An increase of mobility was expected, and because of large grain size and the reduction of surface portion, mobility decreased. In films deposited using 20 ml, cracks were responsible for decreased mobility. However, the surface scattering effect was not observed in thickness control.

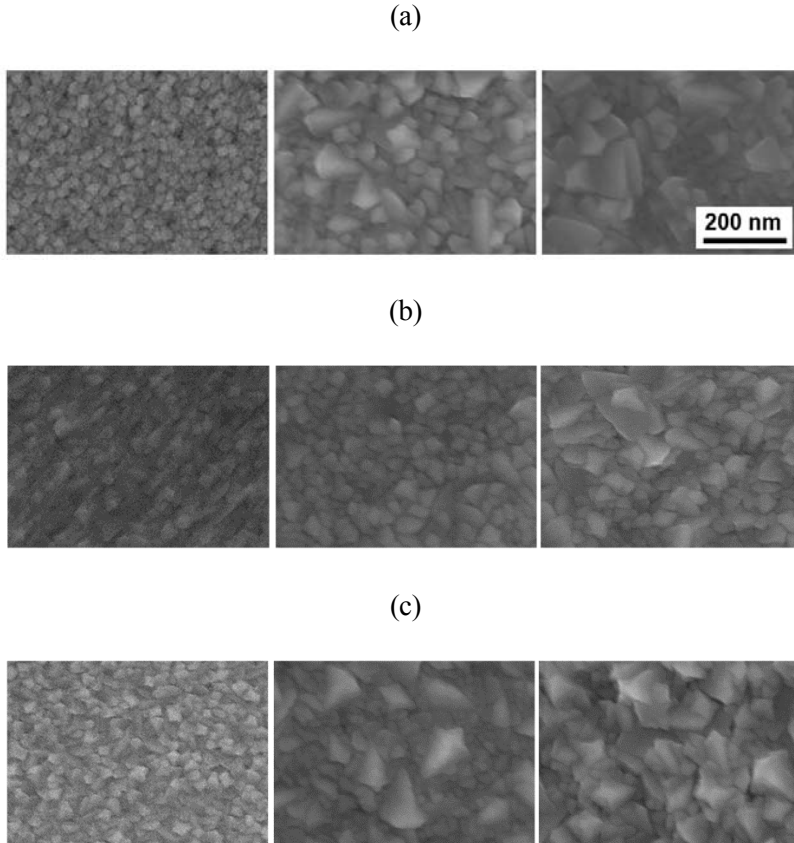


Figure 6.10 Microstructural images of 1 at. % IMO films deposited with different solution volumes and after oxygen partial pressure-controlled annealing.

(a) After 7×10^{-4} Torr: 12.5 ml (left), 15 ml (middle), 20 ml (right).

(b) After 2×10^{-2} Torr: 12.5 ml (left), 15 ml (middle), 20 ml (right).

(c) After 4×10^{-1} Torr: 12.5 ml (left), 15 ml (middle), 20 ml (right).

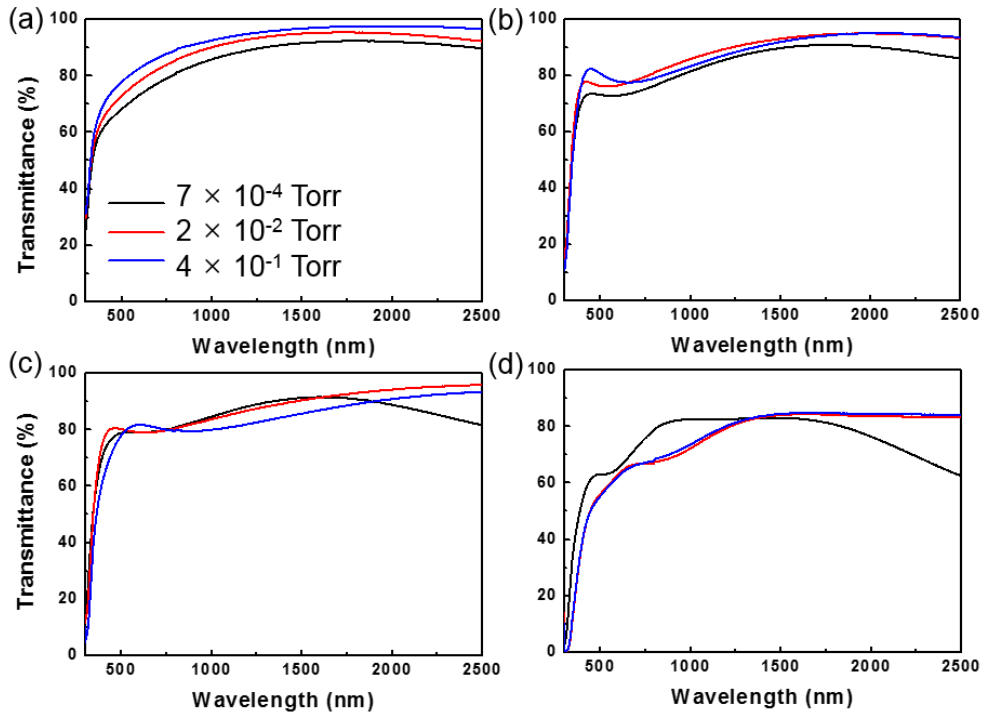


Figure 6.11 Optical transmittance spectra of 1 at. % IMO films after annealing. Solution deposition volumes were (a) 10 ml, (b) 12.5 ml, (c) 15 ml, and (d) 20 ml.

6.4. Effect of dopant concentration and annealing atmosphere

6.4.1. Electrical properties

In transparent conducting oxides (TCO), the electron concentration can be increased by doping with other elements or by generating oxygen vacancies.

To investigate the effect of the dopant concentration on the electron concentration and mobility, the Mo ratio was set to 4.5 at. %.

As the Mo proportion increased, conductivity increased. The dopant contents that showed the maximum conductivity were only slightly different (7×10^{-4} Torr, 2×10^{-2} Torr: 2.25 at. %, 7×10^{-4} Torr: 0.75 at. %), however the conductivity increased and decreased depending on the Mo content. Films annealing under low oxygen partial pressure showed higher conductivity. The highest conductivity was obtained with 2.25 at. % IMO films after annealing under 2.1×10^{-2} Torr.

In Figure 6.12, the Mo concentration affected both the electron concentration and mobility. As a dopant substituting for In, the number of electrons increased with Mo contents of 1.5-2.25 at. % and then decreased at higher levels. When the number of Mo atoms increases, they may not occupy proper lattice sites in the In₂O₃ due to their solubility limit in In₂O₃.⁸⁴ For mobility, the Mo concentration determined the optimum condition. The highest mobility was observed in 0.75 at. % regardless of the oxygen partial pressure. The highest value of mobility was $69.3 \text{ cm}^2/\text{Vs}$ with 2×10^{-2} Torr partial pressure annealing. At 0.75 at. %, mobility decreased due to an increase in the concentration of electron traps as a result of excess Mo doping. This finding is similar to Sn doping in ITO films.⁸⁵

Oxygen partial pressure during annealing affects the electron concentration

significantly because of the oxygen vacancy generation. From the Kröger-Vink notation, the reduction of oxygen partial pressure moves the reaction forward and increases both the oxygen vacancies and the electron concentration.⁶⁰ However, the dependence of partial pressure on mobility was negligible. The formation or dissociation of defects (complex) by oxygen vacancy generation may not be a crucial scattering center.¹³

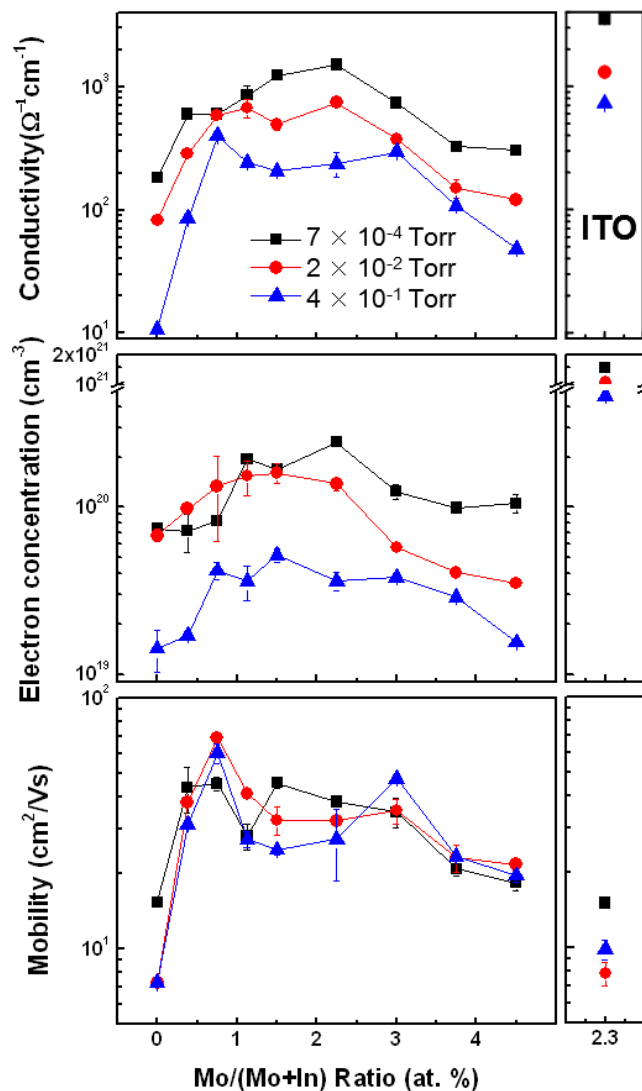


Figure 6.12 Variation of electrical conductivity (top), electron concentration (middle), and mobility (bottom) of spray-coated IMO films as a function of Mo doping and oxygen partial pressure during annealing. Graphs (right) are the electrical properties of the spray-coated ITO film. Optimized Sn concentration was 2.3 at. %.

6.4.2. Optical properties

Optical transparency is also an important characteristic in materials used for transparent electrodes. The average transmittance of the spray-coated IMO films in the visible and NIR spectrum is presented in Figure 6.13. Most of the films displayed excellent transparency (over 80 %) and even better transmittance over 90 % in the NIR region. Average was calculated by integrating the spectral transmittance over the visible and NIR wavelength range (visible: 380 – 780 nm, NIR: 780 - 2500 nm). As electron concentration increased with Mo content, however effect of electron absorption on transmittance in NIR region was not observed.

Average transmittance did not depend on the Mo doping. Transmittance in both the visible and the NIR regions was the lowest in the lowest oxygen partial pressure, which may be due to the carbon residue formed after the thermal pyrolysis of the organic solvent, ethanol.

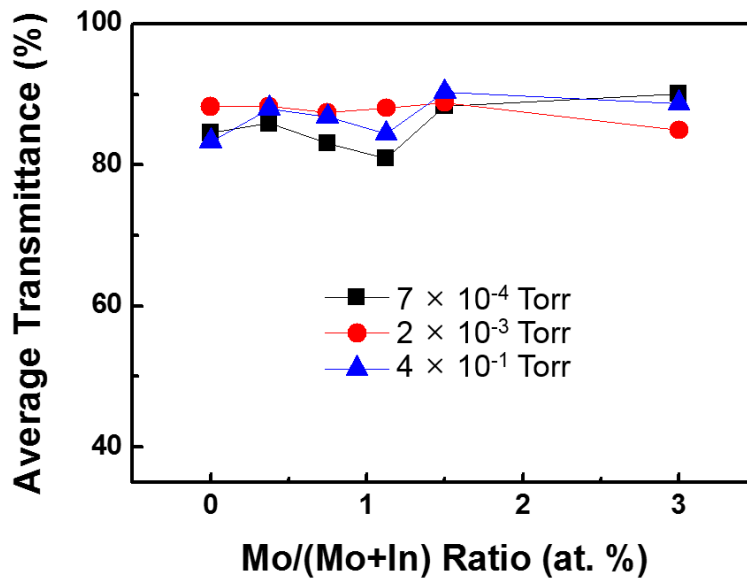


Figure 6.13 Average transmittance of spray-coated IMO films as a function of Mo concentration and oxygen partial pressure during annealing ($\lambda = 380 \sim 2500$ nm).

6.5. Comparison to other ITO and IMO films

6.5.1. Electrical properties

Figure 6.14 is a sorting map for the IMO and ITO samples produced in this work within an ' N - μ ' diagram. We further compared the electron concentration and mobility data from Fig. 6.12 with the data for spray-coated and sputtered IMO and ITO films. Spray-coated ITO films were fabricated in our lab, and sputtered ITO films were purchased. Data for reference IMO films are from previous reports.^{9,84,86,87}

In Figure 6.14, the complex relationship between the solution/processing parameters and electrical properties is represented clearly. In the graphs, the Mo content and oxygen partial pressure are indicated by different figures and colors. The three diagonal lines indicate constant conductivity levels.

Mo doping increased the mobility significantly. A high substrate temperature showed the same effect. Mo doping and oxygen partial pressure control the electron concentration. However, an optimum Mo concentration existed above which the number of electrons did not increase. The maximum electron concentration and mobility were $2.45 \times 10^{20} \text{ cm}^{-3}$ and $103 \text{ cm}^2/\text{Vs}$, respectively. When the oxygen partial pressure decreased to 10^{-6} Torr, an increase of the electron concentration was not observed. This finding indicates that the Mo activation of the generation of oxygen vacancy was suppressed by doping with Mo. In studies of ITO nanoparticle films⁶⁰, control of the oxygen partial pressure changed the electron concentration $\sim 10^{21} \text{ cm}^{-3}$, which was much higher than for IMO film systems ($\sim 2 \times 10^{20} \text{ cm}^{-3}$).

The ' N - μ ' diagram can show the difference of electrical properties between our IMO films and ITO and IMO samples prepared by other deposition techniques. Doping

materials and deposition methods influence the final electrical characteristics of TCO films.

The stars indicate the reference data to compare to samples created in this work. Half shaded and black stars indicate the electrical properties of spray-coated and commercial sputtered ITO films, respectively. Generally, ITO films show high electron concentration ($\sim 10^{21} \text{ cm}^{-3}$) and low mobility ($\sim 40 \text{ cm}^2/\text{Vs}$). Spray-coated ITO films showed lower mobility than commercial ITO. In spray-coated ITO films, concentration increased with partial pressure. The higher mobility of sputtered films is due to a dense and highly uniform microstructure with high purity. Reference IMO films generally showed a lower electron concentration with higher mobility than ITO films. The electron concentration and mobility of sputtered IMO were $\sim 6.6 \times 10^{20} \text{ cm}^{-3}$ and $\sim 130 \text{ cm}^2/\text{Vs}$, respectively, and spray-coated IMO were $\sim 1 \times 10^{20} \text{ cm}^{-3}$ and $\sim 149 \text{ cm}^2/\text{Vs}$, respectively.⁸⁸ Generally, vacuum-deposited IMO showed a higher electron concentration and similar mobility compared to spray-coated IMO film., which may be because dopant atoms can occupy space more uniformly. Compared to sputtered IMO films, spray-coated IMO films in this work showed lower electron concentrations. To enhance the electron number, the partial pressure and dopant concentration were controlled, but the electron concentration was not increased above $2.45 \times 10^{20} \text{ cm}^{-3}$. However, compared to the reference spray-coated IMO films, similar electrical properties were observed.⁷⁻⁹ This tendency was due to the deposition method.

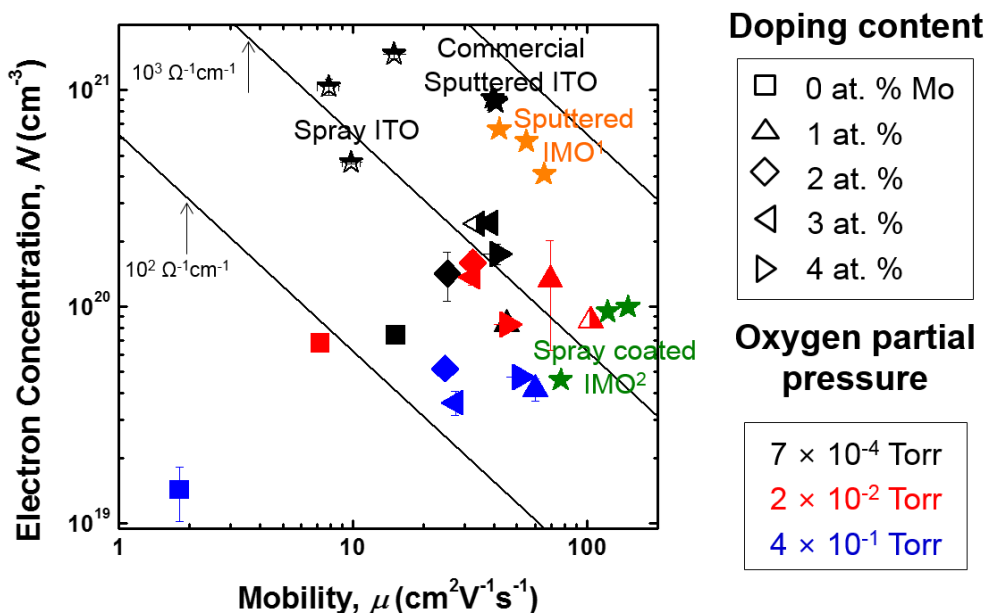


Figure 6.14 Sorting IMO samples in an ‘N- μ ’ diagram: the spray coated IMO films studied in this research and reference ITO and IMO samples were plotted in a materials space based on electron concentration and mobility values. The half-shaded figure indicates the lowest oxygen pressure and the highest substrate temperature.

6.4.2. Optical properties

The optical transmittance of spray-coated ITO and IMO films is shown in Figure 6.15. The average transmittance of spray-coated ITO and IMO films are represented in Table 6.1. The transmittance in the visible and NIR regions were also calculated. Spray-coated ITO with higher electron concentration and lower mobility showed more free-carrier absorption than IMO.¹¹ As a result, similar transmittance was seen in the visible region but was much higher in the NIR region. By changing the dopant element to Mo, electron mobility and transmittance improved.

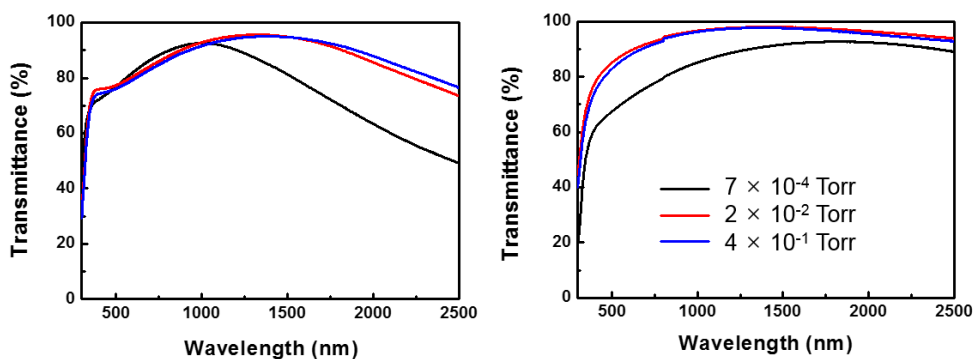


Figure 6.15 Optical transmittance of spray coated (a) 2.3 at. % ITO and (b) 2 at. % IMO films (concentration of starting solution) in the visible and NIR spectrum after oxygen partial pressure annealing.

pO₂	Spray-coated ITO			Spray-coated IMO		
	Average	Visible	NIR	Average	Visible	NIR
7×10^{-4} Torr	75.8	80.7	74.6	84.7	70.7	89.8
2×10^{-2} Torr	87.2	80.3	88.8	93.7	87.4	96.6
4×10^{-1} Torr	87.5	79.0	89.4	92.8	85.5	-96.0

Table 6.1 Average optical transmittance of spray-coated ITO and IMO films. (% transmittance).

6.6. Electron concentration and mobility

The upper dotted line in Figure 6.16 is the carrier concentration that would correspond to 1e/Mo. In ideal conditions, Mo goes into In₂O₃ as Mo⁶⁺ in place of In³⁺, yielding three electrons per Mo (e/Mo). However, in previous work on IMO films⁸⁹, 0.2 < e/Mo < 0.3 for 1 wt. % Mo and 2 wt. % Mo films. This variation in *N* based on the *p*O₂ and e/Mo < 1 suggest that dopant-metal oxygen-interstitial associates may be the dominant Mo-related dopant mechanism, similar to the well studied case of ITO.

In this model, the substitutional Sn dopant in ITO is compensated by interstitial oxygen, (2Sn_{In}[•]O_i^{''})^x at sufficiently high oxygen pressures. As the oxygen pressure is decreased, the interstitial oxygen is removed, “activating” the Sn dopant. The case for IMO is more complicated, because there are several possible valence states for Mo in In₂O₃. For example, Meng et al.⁸⁸ suggested that the activated Mo dopant might be (Mo_{In}^{•••}O_i^{''})[•] with Mo⁶⁺ and e/Mo=1. However, by x-ray photoelectron spectroscopy, Yoshida et al.¹⁰ found a roughly even mixture of Mo⁶⁺ and Mo⁴⁺ in their optimally conducting IMO films but only found Mo⁶⁺ in the low carrier concentration films grown at higher oxygen partial pressure. This finding suggests that the activated Mo dopant is not Mo⁶⁺ (Mo_{In}^{•••}) but rather Mo⁴⁺ (Mo_{In}[•]), which might arise from (2Mo_{In}^{•••}3O_i^{''})^x ⇌ 2Mo_{In}[•] + 2e' + 3/2O₂(g), which also gives e/Mo=1. If this is the correct activation reaction, then our finding that e/Mo ≈ 0.2–0.3 indicates that not all the Mo atoms are activated, as is known to be the case for Sn in ITO. Note that the In₂O₃ bixbyite structure has two different In sites (25% “b” and 75% “d”), and in the case of ITO, only the b-site Sn is active. If in these IMO films grown at 500 °C, the Mo randomly occupies the b and d sites, and only the b-site Mo can be activated, then the expected average carrier concentration would be 0.25e/Mo, very similar to the 0.2–0.3e/Mo found in this work. While there is clearly

not yet sufficient data for a definitive determination of the doping mechanism in IMO, we believe that the basic concept of substitutional Mo dopants compensated by interstitial oxygen is both physically reasonable and explains the currently available data.

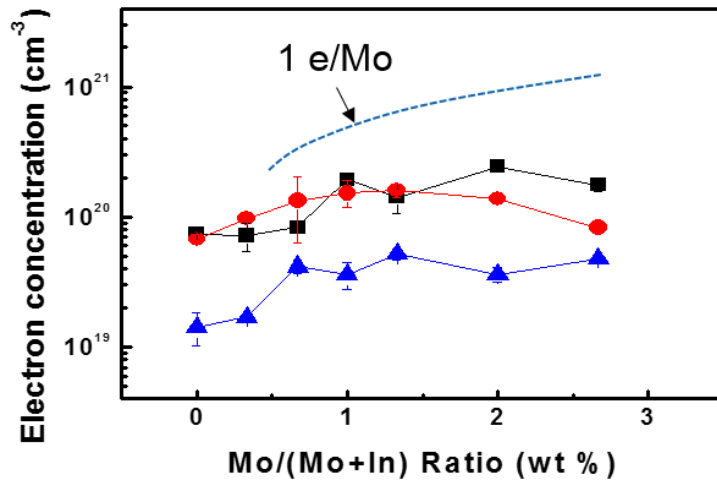


Figure 6.16 Electron concentration of IMO films; the upper dotted line is the electron concentration that would correspond to 1 e/Mo.⁸⁹

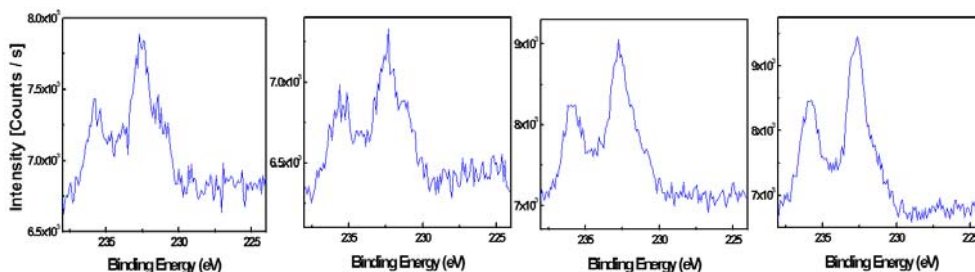


Figure 6.17 Mo 3d spectra for Mo doped In_2O_3 films before annealing (a), after annealing under 7×10^{-4} Torr (b), 2×10^{-2} Torr (c), and under 4×10^{-1} Torr (d). The Mo dopant concentration was 2.9 at. %.

Figure 6.17 shows the Mo XPS spectra for spray-coated IMO films. IMO film showed a small atomic percentage of Mo dopant, and the graph shape was not very smooth. However, clear peaks were detected.

The detailed binding energy of the IMO film was analyzed by the core level spectra of Mo 3d, as shown in Figure 6.11. Mo binding energies are located at 235.75 eV (Mo 3d_{3/2}), and 232.55 eV (Mo 3d_{5/2}). The peak positions are well matched to the core level spectra of previously reported IMO films. In the case of Mo dopant, the spin-orbit splitting of the Mo 3d level led to an energy separation of 3.2 eV between Mo 3d_{3/2} and Mo 3d_{5/2}. The well-matched energy separation of the Mo 3d level peak obtained from the IMO film indicates that Mo dopant in the IMO film exists mainly as Mo^{6+} ions. From XPS results, the Mo dopant existed primarily as Mo 6+, which indicates effective substitution. We expected different chemical states as a function of the partial pressure. However, detailed information was not obtained because of the low reliability due to low dopant concentration.

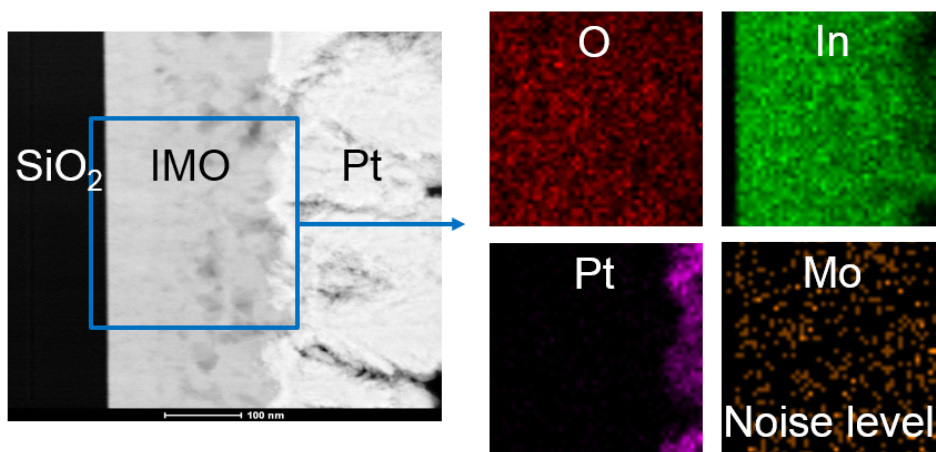


Figure 6.18 TEM images and elemental analysis of 3 at. % Mo-doped In_2O_3 films. Mo segregation was not observed.

Low doping efficiency can be caused by non-uniform distribution. As shown in Figure 6.19, for heavily W-doped In_2O_3 films, energy-filtered transmission electron microscopy (EFTEM) revealed the segregation of tungsten at the grain boundaries. In this case, the dopant is ineffective as a donor or a scattering center to reduce mobility. To investigate this effect, TEM analysis was conducted. For cross-sectional images, the IMO film was spray coated on glass (SiO_2 substrate), and Pt was coated on the IMO film. A dense cross-sectional microstructure was observed. The thickness was 216 nm when the solution volume was 20 ml. In the square region, O, In, Pt, and Mo element mapping was conducted. In was clearly detected, but Mo was obscured by the noise level. Segregation was not observed in morphology analysis. In conclusion, no segregation in IMO films was observed, and segregation or non-uniform distribution (microscopic) of the dopant was not a crucial factor for low electron concentrations.

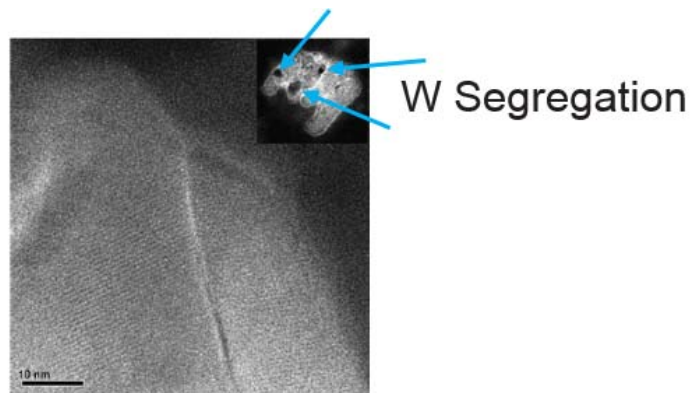


Figure 6.19 A TEM micrograph is displayed using EFTEM. The zones with brighter details, the grain border and grain boundaries, correspond to a higher W content.

6.7. Other dopants

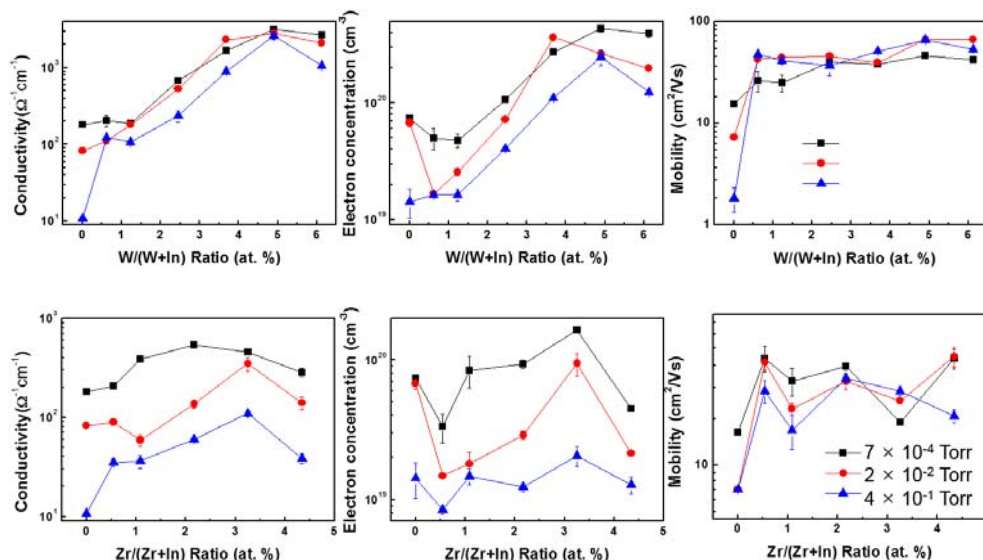


Figure 6.20 Variation of electrical conductivity, electron concentration, and mobility of spray-coated W and Zr-doped In_2O_3 films as a function of dopant concentration and oxygen partial pressure during annealing.

Based on the spray and annealing methods above, W and Zr-doped In_2O_3 films were fabricated, and the electrical properties were measured and are shown in Figure 6.20. W and Zr were chosen because they had potential as high-mobility dopants. The ionic radii and valence difference (W^{6+} : 60 pm, Zr^{4+} : 86 pm) may affect the electrical and optical performance.

Conductivity increased with dopant concentration in both films. Especially with W doping, the conductivity changed by about two orders of magnitude due to changes in

the W concentration, and was larger than Mo and Zr doping. Zr showed stronger oxygen partial pressure dependence than W doping.

The electron concentration increased with the dopant concentration. An interesting point is that a smaller electron concentration was observed than with undoped indium oxide films, despite the addition of dopant. In low partial pressure conditions, this tendency was more significant. After dopant addition (W: 0.61 at. %, Zr: 0.54 at. %), the electron concentration increased with the dopant concentration. W doping generated less electrons than Mo between 1.5 and 2 at. % and was more efficient in electron generation than Mo. Zr doping generated a similar number of electrons when the concentration was greater than 3 at. %. As the doping concentration increased, the dopant could create defects with In and O. These defects suppress the substitution of dopant for In and the generation of oxygen vacancies. This tendency may be stronger for Mo than for W(Zr). Additionally, Zr has a lower valence difference than W or Mo. Therefore, the number of electrons in Zr-doped In₂O₃ films was smaller than Mo and W at the same dopant concentrations. Furthermore, the solubility of the dopant in the indium oxide lattice can be an important factor.

Maximum conductivity and electron concentration were $3.5 \times 10^3 \Omega^{-1}\text{cm}^{-1}$ and $4.8 \times 10^{20} \text{cm}^{-3}$ with W doping and $5.4 \times 10^2 \Omega^{-1}\text{cm}^{-1}$ and $1.6 \times 10^{20} \text{cm}^{-3}$ with Zr doping.

Mobility was maximized at 0.61 and 0.54 at.% for W and Zr doping, respectively, and decreased gradually with the concentration, which was similar to IMO films. The highest mobility was 66.4 and 39.7 cm²/Vs in W and Zr-doped In₂O₃, respectively. The mobility of W-doped In₂O₃ is the highest value among the reported spray-coated W-doped In₂O₃ films.⁸¹ The result of spray-coated Zr-doped In₂O₃ in this work is the same as a previous study. Although a mobility of 170 cm²/Vs was reported in Zr-doped In₂O₃, detailed electrical properties and an explanation were not included.⁹⁰

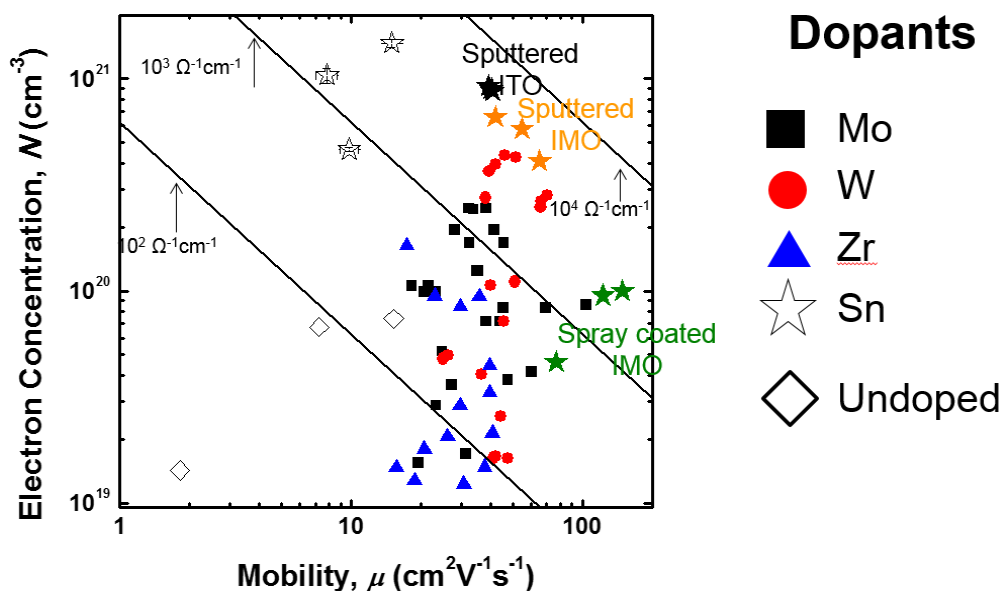


Figure 6.21 Electrical properties of impurity-doped In_2O_3 films in an ‘N- μ ’ diagram.

Figure 6.21 shows the electrical properties of various doped In_2O_3 films. Empty diamonds indicate undoped In_2O_3 films. Compared to spray-coated ITO films, Mo doping increased both the electron concentration and the mobility. By W doping, the mobility increased to $\sim 70 \text{ cm}^2\text{V}^{-1}\text{s}^{-1}$, which was similar to doping with Mo. The electron concentration in W-doped In_2O_3 films was higher than IMO; therefore, the conductivity of W-doped In_2O_3 is higher. Doping with Zr was not effective compared to Mo and W.

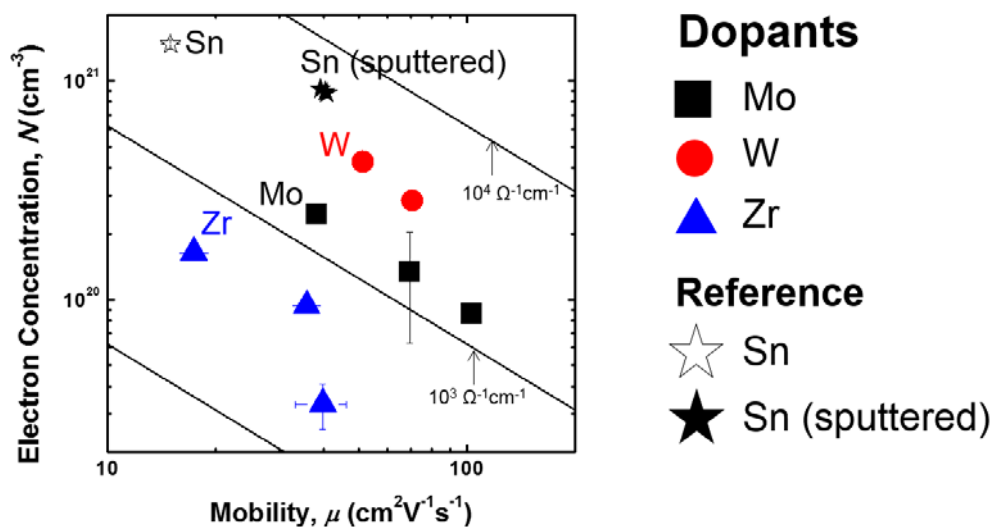


Figure 6.22 Optimal conductivity, electron concentration, and mobility of Mo, W, and Zr-doped In_2O_3 films in an ‘N- μ ’ diagram.

Figure 6.22 shows the best electrical properties of various doped In_2O_3 films. Compared to Sn, the high mobility doping elements Mo, W, and Zr reduced the electron concentration and increased mobility. Mo was appropriate for creating high mobility; however, the electron concentration in W-doped film was much higher, and the electrical conductivity of W doped films was the best among other TCO films. This result was similar to spray-coated and sputtered ITO films.

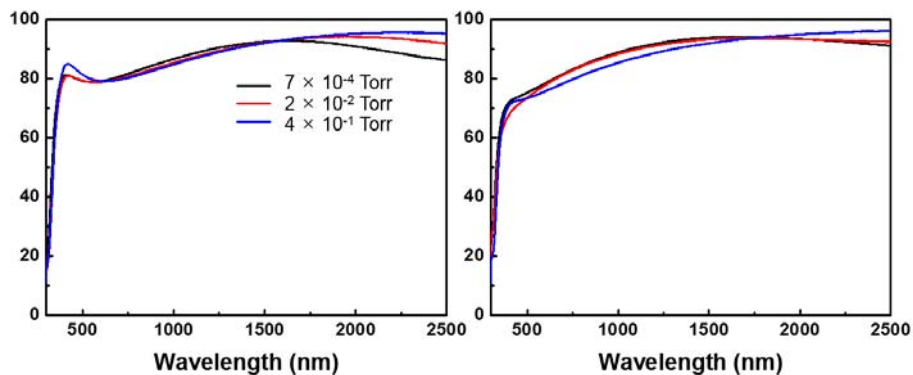


Figure 6.23 Transmittance of spray-coated 2.45 at. % W (left) and 2.17 at. % Zr (right)-doped In_2O_3 films in the visible and NIR spectra after oxygen partial pressure annealing.

The optical transmittance of spray-coated W and Zr-doped In_2O_3 is shown in Figure 6.20. The average, visible and NIR region transmittance of spray-coated W and Zr-doped In_2O_3 films are reported in Table 6.2. Transparency was calculated by integrating the spectral transmittance over the wavelength range as in Figure 6.15. All the films displayed excellent transparency (over 87 %) in all wavelength regions. Most showed 90 % transparency in the NIR region. Compared to the transmittance of spray-coated ITO films shown in Figure 6.15, transmittance in the NIR region was greatly improved and a wider transparency window was obtained with W and Zr doping.

pO ₂	Spray-coated W-doped In ₂ O ₃			Spray-coated Zr-doped In ₂ O ₃		
	Average	Visible	NIR	Average	Visible	NIR
7×10^{-4} Torr	87.8	79.9	89.6	89.2	77.8	92.0
2×10^{-2} Torr	88.8	79.5	91.0	88.8	76.4	91.8
4×10^{-1} Torr	89.5	80.6	91.5	88.5	75.4	91.6

Table 6.2 Average optical transmittance of spray-coated W and Zr-doped In₂O₃ films (% transmittance).

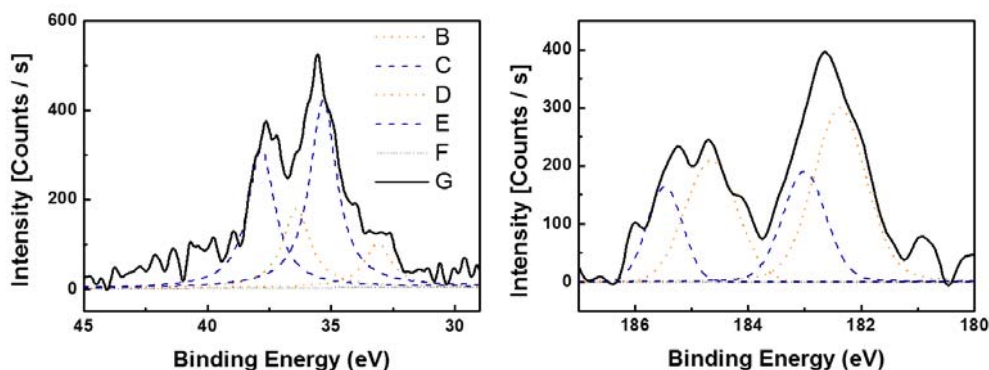


Figure 6.24 W 4f spectra for 2.45 at. % W-doped In_2O_3 films (left) and Zr 3d spectra for 2.17 at. % Zr-doped In_2O_3 films (right) after annealing under 2×10^{-2} Torr.

Chemical state	Fraction	Chemical state	Fraction
W^{4+}	27.37	Zr^{X+}	65.68
W^{6+}	72.63	Zr^{4+}	34.32

Table 6.3 Fraction and chemical state of W and Zr in In_2O_3 films.

Figure 6.24 shows the W and Zr XPS spectra for spray-coated doped In_2O_3 films. When the film showed a small atomic percentage of dopant, the graph shape was not very smooth. The detailed binding energy of the W and Zr-doped In_2O_3 film was analyzed by the core level spectra of W 4f and Zr 3d, as shown in Figure 6.24. W binding energies are located at 35.8 eV (W 4f_{5/2}), and 33.6 eV (W 4f_{7/2}). Zr binding energies

are located at 182.8 eV (Zr 3d_{3/2}), and 185.23 eV (Zr 3d_{5/2}). The peak positions are well matched to the core level spectra of previously reported W and Zr-doped In₂O₃ films. The well matched energy separation of the Mo 3d level peak obtained from the IMO film indicates that Mo dopant in the IMO film exists mainly as Mo⁶⁺ ions. From XPS results, the Mo dopant existed primarily as Mo 6+, which indicates effective substitution. We expected different chemical states as a function of partial pressure. However, in both cases, the dopants exist in the various oxidation states of 6+ and 4+ for W, and 4+ and x+ (0<X<4) for Zr. The fraction of dopants in various oxidation states are reported in Table 2.1. The fraction of W atoms that substituted for In was higher than the Zr fraction. Higher electron concentration in Figure 6.20 may be due to this chemical state.

6.8. Summary

High mobility and a large transparency window were obtained by spray-coated Mo doping of indium oxide film after oxygen partial pressure-controlled annealing. Mo doping improved mobility significantly and generated electrons by substituting for In. The spray-coating parameters were also important for increasing mobility. The electron concentration was increased by oxygen partial pressure-controlled annealing without losing mobility. The optimum dopant concentration for mobility was 0.75 at. %, and the highest mobility was 103 cm²/Vs. The optimum dopant concentration for electron concentration is affected by dopant solubility and is different from the oxygen partial pressure. The average transmittance was greater than 80 % and was near 90 % in the NIR region. Electrical properties were compared to reference ITO and IMO prepared from spray coating and vacuum deposition. Compared to ITO, the electron concentration was lower, and the mobility was much higher. The difference between our data and reference data was our analysis based on '*N-μ*' diagrams. Dopant characteristics and deposition methods are important factors to determine the performance. The transparency window is much larger than for spray-coated ITO films. The mechanism responsible for the changes in electron concentration and mobility was investigated considering various processing parameters, scattering factors, and their relationships. Based on this approach, W and Zr-doped In₂O₃ films were spray coated, and their properties were characterized. These films also showed high mobility and a large transparency window.

CHAPTER 7

Conclusions

7.1. Conclusions

Demand on chemical solution processing is increasing because it is a good candidate for an alternative fabrication method, and this is due to its simplicity and feasibility in low-cost facilities. Especially for flexible electronics, solution processing is the best solution for fabrication. There are various solution deposition methods, such as inkjet printing, spin coating, and spray coating. Solution processing can be applied to most materials, including metals, polymers, and metal oxides. However, electrical conductors were chosen for study, because conducting materials are fundamental and essential materials used as interconnects and electrodes in many electronic devices. Among various potential materials to choose from, research in this study focused on metals and metal oxides (TCOs). Solution-processed conductors can be produced by metal-organic deposition (MOD) or nanoparticle-based solution methods. Both methods have different merits and drawbacks. Despite many advantages, solution-processed conductors have major issues, such as poor performance. To overcome this problem, post-treatment processes (post-annealing) are essential. The annealing process plays a crucial role.

Research into the application of solution-processed conducting materials to a printing process or device fabrication is increasing; however, material properties and the mechanism have not been fully investigated. The annealing process was usually applied with an understanding of the change to the films during annealing, and systematic optimization of the processing has not been conducted effectively.

The objective of this thesis is to improve the performance, especially the electrical and optical properties, of solution-processed conducting films through the annealing process. Before the improvement, investigation into the cause of the poor performance of solution-processed films was performed.

Metal is the most representative conductor. Metal nanoparticles are most widely used in flexible and printed electronics as interconnects and electrodes. In nanoparticle solution, organic ligand coating the nanoparticles is added to prevent agglomeration and to maintain stability in liquid solvents. However, the remaining organic ligand inside the printed films obstructs the coalescence of the metal particles and degrades the electrical performance. To remove organic ligand and improve properties, an annealing process is necessary. Roll-to-roll processing is the best option to achieve low cost and continuity in flexible devices. Therefore, an annealing system that conceptually simplifies roll-to-roll processing was constructed, and a halogen lamp used as a heating source was designed to move instead of the substrate. This moving rapid thermal annealing is very fast and has a high heating rate. The heating rate is an important annealing parameter; however, there were no reports concerning the effect of the heating rate on metal nanoparticles with organic ligands. Moving rapid thermal annealing was compared to conventional furnace annealing with a low heating rate to determine the effect of the heating rate. The grain structure was much denser and the electrical resistivity was much lower for the films obtained by the proposed process than by furnace annealing or

previous methods. TGA results confirmed that the decomposition of organic additives shifted to a higher temperature during moving rapid thermal annealing compared to conventional annealing. The high heating rate prevents the agglomeration of Ag nanoparticles and causes the microstructural evolution to occur at a higher temperature than in furnace annealing. After the decomposition of the organic ligand, the high heating rate induces the densification of the remaining silver nanoparticles.

In transparent conducting oxide, the carrier concentration was changed, and the optical properties were as important as the electrical properties. The melting temperature is much higher than for metals (Ag, Cu); therefore, microstructure evolution is difficult in a low temperature range. Based on metal nanoparticle research, it was concluded that the decomposition of organic ligands and microstructure evolution were crucial to performance. In TCO nanoparticle studies, this approach was applied. However, carrier generation is important in TCOs and must be considered to improve properties.

ITO was chosen because of its excellent performance. ITO nanoparticle films have many advantages; however, electrical conductivity was much lower than ITO films prepared by vacuum deposition and MOD solution. ITO is an oxide material in which electrons are generated by oxygen vacancies. In a reducing atmosphere, the number of electrons can be increased. From metal nanoparticle research, organic ligands in nanoparticle solution must be removed in an oxidizing atmosphere. Therefore, the oxygen partial pressure is a very important factor to determine the conductivity. By controlling the oxygen partial pressure and temperature during annealing, the conductivity of ITO nanoparticle films was greatly improved. It was found that the electron concentration was primarily affected by the oxygen partial pressure, whereas temperature was the dominant parameter affecting mobility. Compared to sputtered ITO, the electron concentration was similar, and mobility was much lower because of a porous

microstructure.

As mentioned above, ITO has many advantages and is the most widely used method. However, it allows a high electron concentration, N , but suffers from low mobility. This results in a narrow transparency window because of low transmittance in the near infrared region (NIR). In solar cells and TFT displays, high mobility is required. Therefore, studies attempting to increase mobility have received extra attention recently. The mobility can be represented by $\mu = \tau e / m^*$; thus, to achieve high mobility, increasing τ or decreasing m^* is required.

Dopants such as Mo, W, and Zr were used in In_2O_3 films. Spray coating was used for the deposition method, which is solution based, appropriate for achieving high mobility, and amenable to the introduction of various dopants and concentrations. The unique aspect of this research is the strategy for improving the mobility of solution-processed, In_2O_3 -based TCOs. Both the choice of appropriate dopant (m^* control) and the fabrication of high-quality film (τ control) approaches were attempted.

Mo doping improved mobility significantly and generated electrons by substitution for In. The electron concentration was increased by oxygen partial pressure-controlled annealing without losing mobility. The optimum dopant concentration for electron concentration is affected by the dopant solubility and depends on the oxygen partial pressure. Mobility was maximized at 0.75 at. % and decreased at higher levels of Mo, because Mo itself can become a dominant scattering center at a large concentration.

W and Zr showed similar mobility and transmittance improvement as Mo. The dopant solubility in In_2O_3 , the dopant-metal oxygen-interstitial associates, the valence difference, and the chemical state of the dopant in In_2O_3 affect the electrical properties of films.

Solution-based deposition, annealing, and the characterization of metal and transparent

metal oxide conductors were conducted. Solution-processed conductors have similar issues, such as poor performance. Different approaches for improving performance were applied to conducting films with different materials, solutions, and deposition methods. In metallic nanoparticles, ligand removal and microstructure control is important to increase the conductivity. In transparent conducting oxide, the carrier concentration is not fixed and affects the optical properties. Therefore, the control of electron generation is crucial in addition to the control of impurities and defects. Dopant concentration and oxygen vacancy generation by oxygen partial pressure-controlled annealing are two strong factors affecting electron concentration. 'N- μ ' diagrams are useful to compare among films and determine the dependence on parameters. Different electronic devices require different specifications and characteristics for high performance. Using various strategies in this thesis, researchers can improve and control the electrical and optical properties for a particular application.

References

- 1 Sunde, T. O. L. *et al.* Transparent and conducting ITO thin films by spin coating of an aqueous precursor solution. *Journal of Materials Chemistry* **22**, 15740-15749 (2012).
- 2 Pasquarelli, R. M., Ginley, D. S. & O'Hayre, R. Solution processing of transparent conductors: From flask to film. *Chemical Society Reviews* **40**, 5406-5441 (2011).
- 3 Song, K. *et al.* Solution-processable tin-doped indium oxide with a versatile patternability for transparent oxide thin film transistors. *Journal of Materials Chemistry* **21**, 14646-14654 (2011).
- 4 Lee, J.-H., Kim, N.-R., Kim, B.-J. & Joo, Y.-C. Improved mechanical performance of solution-processed MWCNT/Ag nanoparticle composite films with oxygen-pressure-controlled annealing. *Carbon* **50**, 98-106, doi:10.1016/j.carbon.2011.07.057 (2012).
- 5 Gamerith, S. *et al.* Direct ink-jet printing of Ag-Cu nanoparticle and Ag-precursor based electrodes for OFET applications. *Advanced Functional Materials* **17**, 3111-3118 (2007).
- 6 Gross, M., Linse, N., Maksimenko, I. & Wellmann, P. J. Conductance enhancement mechanisms of printable nanoparticulate Indium Tin Oxide (ITO) layers for application in organic electronic devices. *Advanced Engineering Materials* **11**, 295-301 (2009).
- 7 S. W. Pang, L. T., R. M. Reano, W. Hu, Y. P. Kong, H. Y. Low, and A. F. Yee. <http://www.ece.ust.hk/~eepang/s4_Stability%20of%20Functional%20Polymers%20after%20Imprinting.htm> (November 19, 2007).
- 8 Al-Dahoudi, N. & Aegerter, M. A. Comparative study of transparent conductive In₂O₃:Sn (ITO) coatings made using a sol and a nanoparticle suspension. *Thin Solid Films* **502**, 193-197 (2006).
- 9 Parthiban, S., Elangovan, E., Ramamurthi, K., Martins, R. & Fortunato, E.

- Investigations on high visible to near infrared transparent and high mobility Mo doped In₂O₃ thin films prepared by spray pyrolysis technique. *Solar Energy Materials and Solar Cells* **94**, 406-412 (2010).
- 10 Calnan, S. & Tiwari, A. N. High mobility transparent conducting oxides for thin film solar cells. *Thin Solid Films* **518**, 1839-1849 (2010).
- 11 Coutts, T. J., Young, D. L. & Li, X. Characterization of transparent conducting oxides. *MRS Bulletin* **25**, 58-65 (2000).
- 12 Hummel, R. E. *Electronic Properties of Materials*. (Springer, 2011).
- 13 Bel Hadj Tahar, R., Ban, T., Ohya, Y. & Takahashi, Y. Tin doped indium oxide thin films: Electrical properties. *Journal of Applied Physics* **83**, 2631-2645 (1998).
- 14 Zhang, L., He, R. & Gu, H. C. Oleic acid coating on the monodisperse magnetite nanoparticles. *Applied Surface Science* **253**, 2611-2617 (2006).
- 15 Gilstrap Jr, R. A., Capozzi, C. J., Carson, C. G., Gerhardt, R. A. & Summers, C. J. Synthesis of a nonagglomerated indium tin oxide nanoparticle dispersion. *Advanced Materials* **20**, 4163-4166 (2008).
- 16 Jeong, S. *et al.* Controlling the thickness of the surface oxide layer on Cu nanoparticles for the fabrication of conductive structures by ink-jet printing. *Advanced Functional Materials* **18**, 679-686 (2008).
- 17 Jianfeng, Y., Guisheng, Z., Anming, H. & Zhou, Y. N. Preparation of PVP coated Cu NPs and the application for low-temperature bonding. *Journal of Materials Chemistry* **21**, 15981-15986 (2011).
- 18 Allen, M. L. *et al.* Electrical sintering of nanoparticle structures. *Nanotechnology* **19** (2008).
- 19 Yi, S. M. *et al.* Improvement of electrical and mechanical properties of Ag nanoparticulate films by controlling the oxygen pressure. *Journal of the*

- Electrochemical Society* **157**, K254-K259 (2010).
- 20 Yoon, Y. H. *et al.* Microstructure and electrical properties of high power laser thermal annealing on inkjet-printed Ag films. *Microelectronic Engineering* **87**, 2230-2233, doi:10.1016/j.mee.2010.02.008 (2010).
- 21 Porter, D. A. & Easterling, K. E. *Phase Transformations in Metals and Alloys, Third Edition (Revised Reprint)*. (Taylor & Francis, 1992).
- 22 Nandiyanto, A. B. D. & Okuyama, K. Progress in developing spray-drying methods for the production of controlled morphology particles: From the nanometer to submicrometer size ranges. *Advanced Powder Technology* **22**, 1-19 (2011).
- 23 Perednis, D. & Gauckler, L. J. Thin film deposition using spray pyrolysis. *Journal of Electroceramics* **14**, 103-111 (2005).
- 24 Joseph Prince, J., Ramamurthy, S., Subramanian, B., Sanjeeviraja, C. & Jayachandran, M. Spray pyrolysis growth and material properties of In₂O₃ films. *Journal of Crystal Growth* **240**, 142-151 (2002).
- 25 Pan, H. *et al.* Fiber laser annealing of indium-tin-oxide nanoparticles for large area transparent conductive layers and optical film characterization. *Applied Physics A: Materials Science and Processing* **104**, 29-38 (2011).
- 26 Haacke, G. New figure of merit for transparent conductors. *Journal of Applied Physics* **47**, 4086-4089 (1976).
- 27 Chopra, K. L., Major, S. & Pandya, D. K. Transparent conductors-A status review. *Thin Solid Films* **102**, 1-46 (1983).
- 28 Prathap, P., Revathi, N., Reddy, K. T. R. & Miles, R. W. Thickness dependence of structure and optoelectronic properties of In₂O₃:Mo films prepared by spray pyrolysis. *Thin Solid Films* **518**, 1271-1274 (2009).
- 29 Yoshida, Y., Wood, D. M., Gessert, T. A. & Coutts, T. J. High-mobility, sputtered films

- of indium oxide doped with molybdenum. *Applied Physics Letters* **84**, 2097-2099 (2004).
- 30 Lee, Y., Choi, J. R., Lee, K. J., Stott, N. E. & Kim, D. Large-scale synthesis of copper nanoparticles by chemically controlled reduction for applications of inkjet-printed electronics. *Nanotechnology* **19** (2008).
- 31 Yi, S.-M. *Microstructure evolution and associated properties of inkjet-printed metal films*, Seoul National University, (2009).
- 32 Kim, J. W., Kim, D. O. & Hahn, Y. B. Effect of rapid thermal annealing on the structural and electrical properties of TiO₂ thin films prepared by plasma enhanced CVD. *Korean Journal of Chemical Engineering* **15**, 217-222 (1998).
- 33 Joo, Y. C., Lee, J. W., Song, O. S., Joo, Y. C. & Kang, C. S. Effect of moving velocity of the heat source on bonding strength in the direct silicon wafer using linear annealing method. *J Korean Inst Met Mater* **39**, 110 (2001).
- 34 Kim, N. R., Lee, J. H., Yi, S. M. & Joo, Y. C. Highly conductive ag nanoparticulate films induced by movable rapid thermal annealing applicable to roll-to-roll processing. *Journal of the Electrochemical Society* **158**, K165-K169 (2011).
- 35 Kim, N.-R. *Effect of annealing parameters on microstructure and electrical properties of solution-processed metallic nanoparticulate films*, (2011).
- 36 <en.wikipedia.org> (2014).
- 37 <google>
- 38 Wagner, S. *et al.* Electronic skin: Architecture and components. *Physica E: Low-Dimensional Systems and Nanostructures* **25**, 326-334 (2004).
- 39 Subramanian, V., Chang, P. C., Lee, J. B., Molesa, S. E. & Volkman, S. K. Printed organic transistors for ultra-low-cost RFID applications. *IEEE Transactions on Components and Packaging Technologies* **28**, 742-747 (2005).

- 40 Suo, Z., Ma, E. Y., Gleskova, H. & Wagner, S. Mechanics of rollable and foldable film-on-foil electronics. *Applied Physics Letters* **74**, 1177-1179 (1999).
- 41 Calvert, P. Inkjet printing for materials and devices. *Chemistry of Materials* **13**, 3299-3305 (2001).
- 42 Singh, M., Haverinen, H. M., Dhagat, P. & Jabbour, G. E. Inkjet printing-process and its applications. *Advanced Materials* **22**, 673-685 (2010).
- 43 Greer, J. R. & Street, R. A. Thermal cure effects on electrical performance of nanoparticle silver inks. *Acta Materialia* **55**, 6345-6349, doi:10.1016/j.actamat.2007.07.040 (2007).
- 44 Perelaer, J., Hendriks, C. E., De Laat, A. W. M. & Schubert, U. S. One-step inkjet printing of conductive silver tracks on polymer substrates. *Nanotechnology* **20** (2009).
- 45 Flynn, J. H. & Wall, L. A. A quick, direct method for the determination of activation energy from thermogravimetric data. *Polym. Lett.* **4**, 323-328 (1966).
- 46 Jung, J. K. *et al.* Characteristics of microstructure and electrical resistivity of inkjet-printed nanoparticle silver films annealed under ambient air. *Philosophical Magazine* **88**, 339-359 (2008).
- 47 Zabet-Khosousi, A., Trudeau, P. E., Suganuma, Y., Dhirani, A. A. & Statt, B. Metal to insulator transition in films of molecularly linked gold nanoparticles. *Physical Review Letters* **96** (2006).
- 48 Mayadas, A. F. & Shatzkes, M. Electrical-resistivity model for polycrystalline films: The case of arbitrary reflection at external surfaces. *Physical Review B* **1**, 1382-1389 (1970).
- 49 Cuevas, F. G., Montes, J. M., Cintas, J. & Urban, P. Electrical conductivity and porosity relationship in metal foams. *Journal of Porous Materials* **16**, 675-681 (2009).
- 50 Anto, B. T., Sivaramakrishnan, S., Chua, L. L. & Ho, P. K. H. Hydrophilic sparse ionic

- monolayer-Protected metal nanoparticles: Highly concentrated nano-Au and nano-Ag "Inks" that can be sintered to near-Bulk conductivity at 150°C. *Advanced Functional Materials* **20**, 296-303 (2010).
- 51 Chou, K. S., Huang, K. C. & Lee, H. H. Fabrication and sintering effect on the morphologies and conductivity of nano-Ag particle films by the spin coating method. *Nanotechnology* **16**, 779-784 (2005).
- 52 Lee, H. H., Chou, K. S. & Huang, K. C. Inkjet printing of nanosized silver colloids. *Nanotechnology* **16**, 2436-2441 (2005).
- 53 Wang, T., Chen, X., Lu, G. Q. & Lei, G. Y. Low-temperature sintering with nano-silver paste in die-attached interconnection. *Journal of Electronic Materials* **36**, 1333-1340 (2007).
- 54 Sasaki, T. *et al.* One-step solvothermal synthesis of cubic-shaped ITO nanoparticles precisely controlled in size and shape and their electrical resistivity. *Journal of Materials Chemistry* **20**, 8153-8157 (2010).
- 55 Bhatti, M. T., Rana, A. M. & Khan, A. F. Characterization of rf-sputtered indium tin oxide thin films. *Materials Chemistry and Physics* **84**, 126-130, doi:10.1016/j.matchemphys.2003.11.022 (2004).
- 56 Kim, S. H., Park, N.-M., Kim, T. & Sung, G. Electrical and optical characteristics of ITO films by pulsed laser deposition using a 10 wt.% SnO₂-doped In₂O₃ ceramic target. *Thin Solid Films* **475**, 262-266, doi:10.1016/j.tsf.2004.08.032 (2005).
- 57 Ederth, J. *et al.* Electrical and optical properties of thin films prepared by spin coating a dispersion of nano-sized tin-doped indium oxide particles. *Smart Materials and Structures* **11**, 675-678 (2002).
- 58 Cordonier, C. E. J., Nakamura, A., Yoshioka, D., Shimada, K. & Fujishima, A. A solution process for preparation of low resistance layered indium tin oxide films. *Thin*

- Solid Films* **534**, 529-534, doi:10.1016/j.tsf.2013.03.007 (2013).
- 59 Frank, G. & Köstlin, H. Electrical properties and defect model of tin-doped indium oxide layers. *Applied Physics A Solids and Surfaces* **27**, 197-206 (1982).
- 60 Kim, N. R. *et al.* Enhanced conductivity of solution-processed indium tin oxide nanoparticle films by oxygen partial pressure controlled annealing. *Journal of Materials Chemistry C* **1**, 5953-5959 (2013).
- 61 Edwards, P. P., Porch, A., Jones, M. O., Morgan, D. V. & Perks, R. M. Basic materials physics of transparent conducting oxides. *Dalton Transactions*, 2995-3002 (2004).
- 62 Song, K., Yang, W., Jung, Y., Jeong, S. & Moon, J. A solution-processed yttrium oxide gate insulator for high-performance all-solution-processed fully transparent thin film transistors. *Journal of Materials Chemistry* **22**, 21265-21271 (2012).
- 63 Nadaud, N., Nanot, M. & Boch, P. Sintering and electrical properties of titania- and zirconia-containing In₂O₃-SnO₂ (ITO) ceramics. *Journal of the American Ceramic Society* **77**, 843-846 (1994).
- 64 Pan, H., Ko, S. H. & Grigoropoulos, C. P. The Solid-State Neck Growth Mechanisms in Low Energy Laser Sintering of Gold Nanoparticles: A Molecular Dynamics Simulation Study. *Journal of Heat Transfer* **130**, 092404, doi:10.1115/1.2943303 (2008).
- 65 Ziegler, G., Heinrich, J. & Wötting, G. Relationships between processing, microstructure and properties of dense and reaction-bonded silicon nitride. *Journal of Materials Science* **22**, 3041-3086 (1987).
- 66 Duba, A. G. Electrical conductivity of coal and coal char. *Fuel* **56**, 441-443 (1977).
- 67 Shie, J. L. *et al.* Thermal pyrolysis of poly(vinyl alcohol) and its major products. *Energy and Fuels* **16**, 109-118 (2002).
- 68 Liu, H., Avrutin, V., Izyumskaya, N., Özgr, Ü. & Morkoç, H. Transparent conducting

- oxides for electrode applications in light emitting and absorbing devices. *Superlattices and Microstructures* **48**, 458-484 (2010).
- 69 Tahar, R. B. H., Ban, T., Ohya, Y. & Takahashi, Y. Optical, structural, and electrical properties of indium oxide thin films prepared by the sol-gel method. *Journal of Applied Physics* **82**, 865-870 (1997).
- 70 Tsuchiya, T., Yamaguchi, F., Morimoto, I., Nakajima, T. & Kumagai, T. Microstructure control of low-resistivity tin-doped indium oxide films grown by photoreaction of nanoparticles using a KrF excimer laser at room temperature. *Applied Physics A: Materials Science and Processing* **99**, 745-749 (2010).
- 71 Wei, Q., Zheng, H. & Huang, Y. Direct patterning ITO transparent conductive coatings. *Solar Energy Materials and Solar Cells* **68**, 383-390 (2001).
- 72 Jeong, J. A. & Kim, H. K. Characteristics of inkjet-printed nano indium tin oxide particles for transparent conducting electrodes. *Current Applied Physics* **10**, e105-e108 (2010).
- 73 Puetz, J. & Aegerter, M. A. Direct gravure printing of indium tin oxide nanoparticle patterns on polymer foils. *Thin Solid Films* **516**, 4495-4501 (2008).
- 74 Aegerter, M. A. & Al-Dahoudi, N. Wet-chemical processing of transparent and antiglare conducting ITO coating on plastic substrates. *Journal of Sol-Gel Science and Technology* **27**, 81-89 (2003).
- 75 Hong, S. J., Kim, Y. H. & Han, J. I. Development of ultrafine indium tin oxide (ITO) nanoparticle for ink-jet printing by low-temperature synthetic method. *IEEE Transactions on Nanotechnology* **7**, 172-176 (2008).
- 76 Wu, H. *et al.* Electrospun metal nanofiber webs as high-performance transparent electrode. *Nano Letters* **10**, 4242-4248 (2010).
- 77 *cpfilm*, <<http://www.cpfilm.com/>>

- 78 *delttech*, <<http://www.delta-technologies.com/>>
- 79 Li, J. *et al.* Organic light-emitting diodes having carbon nanotube anodes. *Nano Letters* **6**, 2472-2477 (2006).
- 80 Eda, G., Fanchini, G. & Chhowalla, M. Large-area ultrathin films of reduced graphene oxide as a transparent and flexible electronic material. *Nature Nanotechnology* **3**, 270-274 (2008).
- 81 Acosta, D. R. & Martínez, A. I. Electron microscopy and physical studies of a new tungsten doped indium oxide transparent conductor. *Thin Solid Films* **515**, 8432-8437 (2007).
- 82 Shin, Y. H., Kim, H. K. & Na, S. I. Effect of MoO₃ doping power on the electrical, optical, and structural properties of MoO₃-doped In₂O₃ anodes for organic solar cells. *Journal of Vacuum Science and Technology A: Vacuum, Surfaces and Films* **30** (2012).
- 83 Thompson, C. V. Structure evolution during processing of polycrystalline films. *Annual Review of Materials Science* **30**, 159-190 (2000).
- 84 Parthiban, S. *et al.* High near-infrared transparent molybdenum-doped indium oxide thin films for nanocrystalline silicon solar cell applications. *Solar Energy Materials and Solar Cells* **93**, 92-97 (2009).
- 85 Li, X. *et al.* The electrical and optical properties of molybdenum-doped indium oxide films grown at room temperature from metallic target. *Semiconductor Science and Technology* **20**, 823-828 (2005).
- 86 Van Hest, M. F. A. M., Dabney, M. S., Perkins, J. D. & Ginley, D. S. High-mobility molybdenum doped indium oxide. *Thin Solid Films* **496**, 70-74 (2006).
- 87 Parthiban, S., Ramamurthi, K., Elangovan, E., Martins, R. & Fortunato, E. Spray deposited molybdenum doped indium oxide thin films with high near infrared transparency and carrier mobility. *Applied Physics Letters* **94** (2009).

- 88 Meng, Y. *et al.* A new transparent conductive thin film In₂O₃:Mo. *Thin Solid Films* **394**, 219-223 (2001).
- 89 Warm Singh, C. *et al.* High-mobility transparent conducting Mo-doped In₂O₃ thin films by pulsed laser deposition. *Journal of Applied Physics* **95**, 3831-3833 (2004).
- 90 Groth, R. Untersuchungen an halbleitenden Indiumoxydschichten. *physica status solidi (b)* **14**, 69-75, doi:10.1002/pssb.19660140104 (1966).

요약(국문초록)

용액 공정은 진공 증착 공정에 비해 저가, 상온/상압 공정, 환경 친화적 공정, 유연성 소자의 응용 가능성 등의 많은 장점을 가지고 있다. 하지만, 용액 공정으로 제작된 박막이 실제 소자에 적용되기 위해서는 그 특성과 성능이 향상되어야 한다는 문제를 가지고 있다. 용액 공정 이후에는 고상화 및 내부의 결함을 제거하고 특성을 제어하기 위하여 반드시 후속 처리가 필요하다. 전자 소자에서 가장 기본적이고 중요한 역할을 하는 전도성 물질을 선택하여, 용액 공정으로 제작하고 후속 열처리를 통해 특성을 향상시키고 평가하는 연구를 진행하였다. 전도성 물질 중, 전도성이 가장 우수한 금속과 투명성까지 갖춘 투명 전도성 산화물을 주제로 삼았다. 금속 나노입자의 경우, 입자를 싸고 있는 유기 리간드를 제거하고 기공이 없는 조밀한 미세구조를 형성하여 전도도를 향상시킬 수 있었다. 후속 열처리의 빠른 승온 속도를 통해 이와 같은 결과를 달성할 수 있었다. 투명 전도성 산화물의 대표적인 산화인듐-주석 (ITO) 나노입자 연구에서는, 산화물 내부의 산소 공공 농도를 향상시키고, 입자를 싸고 있는 유기 리간드를 효과적으로 제거할 수 있는 최적의 산소 분압을 열처리 과정에서 유지하여 기존의 ITO 나노입자 박막보다 뛰어난 전도도와 투과도를 갖는 투명전극박막을 개발하였다. ITO의 높은 전자 농도 때문에 근적외선 투과도가 저하되는 현상은 주석 대신 몰리브덴을 도핑함으로써 해결할 수 있었다. 또한 증착 방법을 나노입자 용액 대신 전구체 용액을 사용하는 스프레이 코팅으로 전환함으로써 전자 농도는 낮추고 이동도를 향상시켜 전도성 및 투과도를 향상시켰다. 또한 텅스텐, 지르코늄도 새로운 도핑 원소로 이용하였으며, 높은 전도도 및 투과도를 확보하였다.

표제어: 용액 공정, 열처리, 투명 전도성 산화물, 금속, 산소분압, 나노입자

학 번: 2011-30931